SANDIA REPORT
SAND2024-11708
Printed September 2024

Sandia National Laboratories

BeyondFingerprinting: AI-guided discovery of robust materials & processes

Brad L. Boyce, Rémi Dingreville, David P. Adams, Carianne Martinez, J. Elliott Fowler, Jamin R. Pillars, Ryan Wixom

Harry K. Moffat, Warren L. Davis, Sarah Ackerman, Ann Speed, Anthony Garland, Scott A. Roberts, Jon J. Coleman, Frank W. DelRio, Dale Cillessen, Jay D Carroll, Habib N. Najm, John F. Curry, Kyle L. Johnson, Sarah K. Dudley , Sadhvikas J. Addamane, Amelia Henriksen, Joyce O. Custer, Jacqueline M. Wentz, Saaketh Desai, Kimberly Bassett, Troy P. Shilt, Elise Walker, Matias Kalaswad, Ankit Shrivastava, Tomas F. Babuska, Matthew Kottwitz, Kaitlynn M. Fitzgerald, M. Jain, Carlos Mejia, Jonas Actor, Niladri Das, Nate Bianco, Tylan Watkins, Kyle Dorman, Reese E. Jones, Moe Khalil, Nat Trask

Prepared by
Sandia National Laboratories
Albuquerque, New Mexico
87185 and Livermore,
California 94550

Issued by Sandia National Laboratories, operated for the United States Department of Energy by National Technology & Engineering Solutions of Sandia, LLC.

Available to DOE and DOE contractors from
U.S. Department of Energy
Office of Scientific and Technical Information
P.O. Box 62
Oak Ridge, TN 37831

Telephone: (865) 576-8401
Facsimile: (865) 576-5728
E-Mail: reports@osti.gov
Online ordering: http://www.osti.gov/scitech

Available to the public frompu
U.S. Department of Commerce
National Technical Information Service
5301 Shawnee Rd
Alexandria, VA 22312

Telephone: (800) 553-6847
Facsimile: (703) 605-6900
E-Mail: orders@ntis.gov
Online order: https://classic.ntis.gov/help/order-methods/

ABSTRACT

BeyondFingerprinting was a 2021-2024 Sandia Grand Challenge LDRD exploring the potential to develop new resilient materials and manufacturing processes by taking an artificial-intelligence (AI)-guided approach that integrates human-subject-matter expertise with algorithms enriched with physics-based constraints to unearth process-structure-property correlations. Such algorithms, trained on high-throughput experiments and simulations, are shown to serve as surrogate models that efficiently detect key "fingerprints" in materials data, prognose material performance, and guide effective process improvements. To accelerate broader adoption across mission areas, this AI-guided approach was demonstrated with three complex process-centric exemplars: electroplating, physical vapor deposition, and laser powder bed fusion. Together, these exemplars impact nearly every hardware component relevant to DOE and NNSA national security missions.

ACKNOWLEDGEMENTS

We would like to thank the LDRD office (B. Hassan, D. Sinar, W.L. Hermina, L. Cunnigham, M. Arrowsmith) for the help and support throughout these three years. We also would like to thank N. Bouxsein from Perspectives Inc. for all the Tracking and Perspective reports that helped us with programmatic overview of *Beyond*Fingerprinting.

CONTENTS

LIST OF FIGURES

LIST OF TABLES

This page left blank

EXECUTIVE SUMMARY

BeyondFingerprinting was a 3-year Grand Challenge project funded by Sandia National Labs' LDRD (Laboratory Directed Research and Development) program. The BeyondFingerprinting project explored the discovery of new, resilient materials and manufacturing processes by taking an artificial-intelligence(AI)-guided approach that integrates human-subject-matter expertise with algorithms enriched with physics-based constraints to unearth process-structure-property correlations. Such algorithms, trained on high-throughput experiments and simulations, can serve as surrogate models that efficiently detect key "fingerprints" in materials data, prognose material performance, and guide effective adaptations. To accelerate broader adoption across mission areas, this AI-guided approach was demonstrated with three complex process-centric exemplars: electroplating, physical vapor deposition, and laser powder bed fusion.

Mission. Vision. Product. The mission of *Beyond*Fingerprinting was to accelerate the discovery of process-structure-property correlations and their underlying mechanistic causation, thereby enabling new resilient materials and manufacturing processes for all national security hardware. In a *Beyond*Fingerprinting future, component design, manufacturing methods, and materials will be simultaneously optimized by semi-autonomous systems, where the engineer does not have to envision possible solutions and then painstakingly (and expensively) test each solution with build-and-check methods; instead, they will simply select appropriate algorithms, embed known physical laws/constraints, and assign design objectives. The 'product' of *Beyond*Fingerprinting was more than just demonstrating novel high-throughput methods, customized materials-centric hybrid-informed algorithms, and related AI-guided workflows. It was about advancing the understanding and trust in how such an approach can complement traditional expert-guided wisdom and conventional high-fidelity mod/sim to efficiently reveal new, robust material processes while also facilitating basic discoveries of the mechanistic causation underlying correlations.

Project Architecture Overview. *Beyond*Fingerprinting has shown how complex, multi-modal, high-throughput process data streams can be interpreted through hybrid-informed machine learning architectures to realize substantially improved process outcomes. The project was arranged into three exemplar process thrusts and two main cross-cutting themes:

- **Exemplar 1 - Electroplating (aka Electrodeposition).** Sandia currently designs over 700 parts/components that involve electroplating to build devices ranging from thermoelectric generators to stronglinks. Electroplated metals enable transmission of electrical signals, enhance adhesion for soldering/wire-bonding, offer protection from corrosion or wear, improve lubricity, and impede diffusion. However, the development of new plating solutions is time-consuming and labor-intensive. The electroplating process has a highly nonlinear sensitivity to the bath chemistry, in addition to several other parameters (e.g. current density conditions, electrode configuration, bath temperature/agitation, complexing agent concentrations, etc.). Process optimization is largely trial-and-error, guided by experienced practitioners, and difficult to translate from lab-scale to production-scale.
- **Exemplar 2 - Physical Vapor Deposition (PVD)**. PVD is used for numerous Sandia applications, including microelectronics, power sources, neutron generators, surety mechanisms, and Z-machine hardware. While the PVD process offers many challenges, we focus on the specific task of improving the mechanical properties (e.g. adhesion between the deposited film and the substrate). Delamination, often a root-cause of subsequent hardware failures, is difficult to anticipate because it involves complex chemo-physical processes

governed by numerous factors (substrate roughness/defects/cleanliness, impurities from the vapor phase, residual stresses that build up during deposition, etc.).

- **Exemplar 3 - Laser Powder Bed Fusion (LPBF).** NNSA has been advocating for the adoption of additive manufacturing as an agile pathway to technology insertion in our low-volume applications. Yet, rapid qualification continues to be a bottleneck. To address this challenge, there are numerous examples of high-fidelity simulations under development. However, due to computational constraints and gaps in understanding, those simulations consider only specific aspects of the overall process (a subset of the requisite physics) rather than the entire complex process: powder packing, laser-matter interactions, melted-fluid/particle dynamics, non-equilibrium solidification, and solid-state phase transformations. An AI/ML approach provides an efficient surrogate representation that can incorporate experimental observations as well as focused high-fidelity simulations into a comprehensive process prediction.

- **Cross-cut: Multi-Modal High-Throughput Data Streams.** One of the core scientific questions examined in *Beyond*Fingerprinting pertained to efficient and effective methods for fusing data across multiple data streams. Available process data is complex. It involves a combination of pre-process, in-process, and post-process information from disparate sources in multiple forms: scalar parameters, time-series data, spatially resolved image data, as well as 2D and 3D datasets, each with concomitant uncertainties.

- **Cross-cut: Hybrid-Informed Multi-Layered Algorithms (Himulya).** The fabrication processes under consideration provide extremely heterogeneous data streams with varying degrees of knowledge of the underlying physics. In *Beyond*Fingerprinting, we explored the full gamut of machine-learning (ML) algorithms: (1) purely regressive ("black box") methods where there is no embedded underlying physics, (2) physics-informed methods where physical laws are weakly enforced through a penalty function, or (3) structure-preserving methods where physical constraints (e.g. conservation laws, process limits) are rigidly enforced. Each of these approaches can have value in certain aspects of an overall system-level process model.

BeyondFingerprinting's generalizable approach followed three systematic steps that are common across each exemplar. These steps are:

- **Detect**: streamline data streams; initiate hybrid-informed algorithm; establish credibility
- **Prognose**: integrate heterogeneous data; reveal process-structure-property correlations; evaluate trust
- **Adapt**: incorporate closed-loop systems; Himulaya-guided adaptation; promote use/adoption

While technical details vary from one exemplar to the other, the general workflow is common and can be transferred beyond the current exemplars.

Outcomes: Greater than the sum of its parts, *Beyond*Fingerprinting demonstrated the generalizability of the detect-prognose-adapt sequence for accelerated process improvement.

*Beyond*Fingerprinting was about TRANSFORMING the process-structure-property manufacturing paradigm to achieve innovative and precisely controlled manufacturing processes of reliable components. As listed in the summary of our work in Section 1, the *Beyond*Fingerprinting team has been developing and employing new types of hybrid-informed ML algorithms that can detect key

signatures in materials data, prognose material performance, and guide effective manufacturing process adaptations. This paradigm shift aligns with Laboratories Strategic Priority 5: "Invest and demonstrate pathfinder systems to address threats" and Priority 6: "Deploy outstanding engineering, science, and technology to our missions". By fusing experiments, modeling, and physics-informed algorithms, we have demonstrated (1) the technical basis for confidence in small-batch, high-reliability systems with limited test hardware required in our national security mission, and (2) the technologies, tools, and approaches to modernize how components are made and enable the realization of products not yet imagined. In line with the Laboratories Strategic Priority 2: "Maintain an agile and effective nuclear deterrence", moving forward, we assert that our Detect-Prognose-Adapt approach can add agility by offering a pathway to rapidly adapt to changing requirements and providing alternative methods to sustain, modernize, design, produce, secure, and employ a flexible and responsive stockpile.

*Beyond*Fingerprinting was about *DISCOVERING* the fundamental mechanistic causes underpinning process-structure-property correlations. As illustrated in the many examples shown in Section 1, our three exemplars served as specific use cases to demonstrate generality and build trust in AI-guided concepts that bridge foundational process science to applied component engineering to solve materials reliability challenges relevant to both Sandia's Nuclear Deterrence(ND) Enterprise and other hardware-dependent missions. Our work lays out the foundation for an AI/ML-guided fusion of multimodal data to accelerate the process-structure-property optimization paradigm by revealing elusive correlations and distilling the data avalanche into essential actionable information.

*Beyond*Fingerprinting was about *EMPOWERING* our workforce with emerging capabilities and cultural change to enable greater productivity, creativity and competitiveness as defined in the Laboratories Strategic Priority 7: "Unleash the power of Sandia". By delivering customized materials-centric algorithms, constrained by physical laws, guided by expert knowledge, and trained with automated high-throughput closed-loop experimental data, *Beyond*Fingerprinting capabilities have removed some of the subject-matter expert (SME) barriers in cognition, data integration, interpretation, and experience/intuition changing the way the SME is performing his/her job, focusing more on decision-making and less on build-and-check.

ACRONYMS AND TERMS

Acronym/Term	Definition
2D	Two-dimensional
3D	Three-dimensional
AFM	Atomic Force Microscopy
AI	Artificial Intelligence
AM	Additive Manufacturing
CLIP	Contrastive Language-Image Pre-training
COTS	Commercially Off-The-Shelf
CTE	Coefficient of Thermal Expansion
DAQ	Data Acquisition
DeepONet	Deep Operator Network
DFT	Density Functional Theory
DNS	Direct Numerical Simulation
EBSD	Electron Back Scattered Diffraction
EDS	Energy Dispersive X-ray Spectroscopy
FAIR	Findable, Accessible, Interoperable, Reusable
FWHM	Full Width Half Max
GB	Grain boundary
Grad-CAM	Gradient-weighted Class Activation Mapping
GRU	Gated Recurrent Unit
GP	Gaussian Process
GUI	Graphical User Interface
Himulya	Hybrid-Informed Multi-Layered Algorithms
HT	High Throughput
HTT	High Throughput Tensile
LAMMPS	Large-scale Atomic/Molecular Massively Parallel Simulator
LPBF	Laser Power Bed Fusion
LSTM	Long-Short Term Memory
LSV	Linear Sweep Voltammetry
MEMS	Micros-Electro-Mechanical System
ML	Machine Learning
ND	Nuclear Deterrence
PBE	Perdew-Burke-Ernzerhof
PCA	Principal Component Analysis

Acronym/Term	Definition
PIMA	Physics-Informed Multimodal Autoencoder
PL	Photoluminescence
PVD	Physical Vapor Deposition
RGB	Red, Blue, Green
RMS	Root Mean Square
RNN	Recurrent Neural Network
SEM	Scanning Electron Microscope
SiMTRA	Simulation of Metal TRAnsport
SLM	Spatial Light Modulator
SME	Subject Matter Expert
UV-Vis	Ultraviolet-Visible
VAE	Variational Autoencoder
VDoS	Vibrational Density of State
XRD	X-ray Diffraction

1. SUMMARY OF PUBLISHED / SUBMITTED MANUSCRIPTS

1.1. A digital twin for materials

Digital twins are emerging as powerful tools for supporting innovation as well as optimizing the in-service performance of a broad range of complex physical machines, devices, and components. A digital twin is generally designed to provide accurate in-silico representation of the form (i.e., appearance) and the functional response of a specified (unique) physical twin. This paper offers a new perspective on how the emerging concept of digital twins could be applied to accelerate materials innovation efforts. Specifically, it is argued that the material itself can be considered as a highly complex multiscale physical system whose form (i.e., details of the material structure over a hierarchy of material length) and function (i.e., response to external stimuli typically characterized through suitably defined material properties) can be captured suitably in a digital twin. Accordingly, the digital twin can represent the evolution of structure, process, and performance of the material over time, with regard to both process history and in-service environment. This paper establishes the foundational concepts and frameworks needed to formulate and continuously update both the form and function of the digital twin of a selected material physical twin. The form of the proposed material digital twin can be captured effectively using the broadly applicable framework of n-point spatial correlations, while its function at the different length scales can be captured using homogenization and localization process-structure-property surrogate models calibrated to collections of available experimental and physics-based simulation.

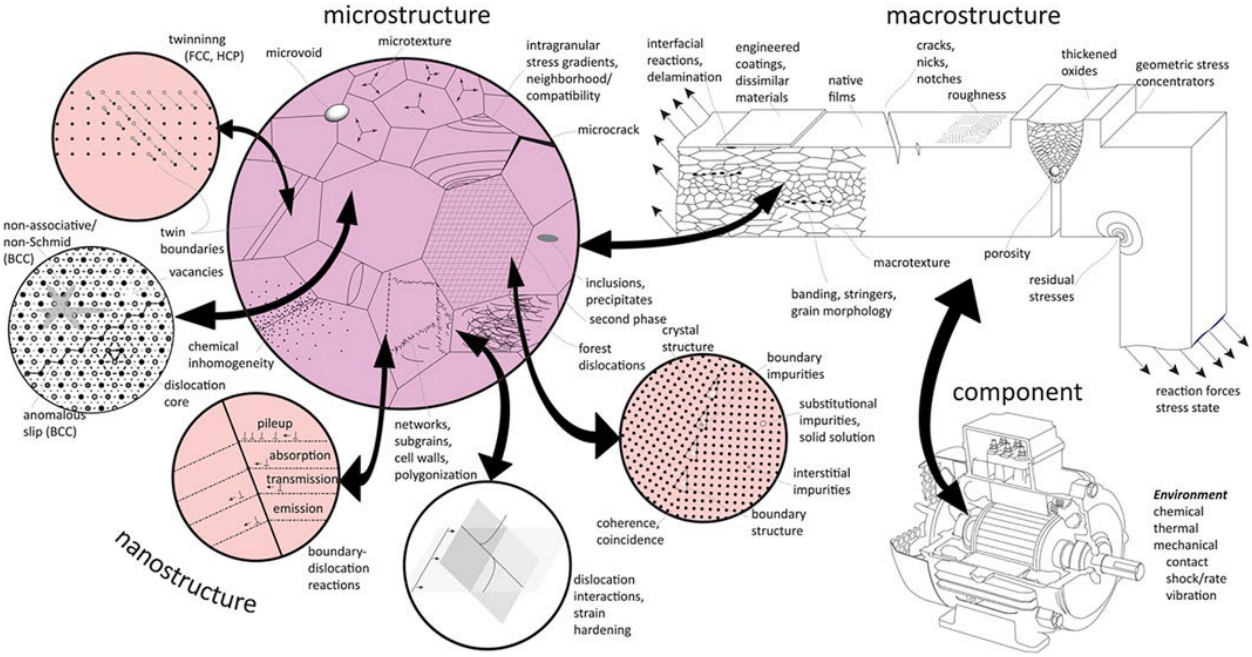

Figure 1. To manifest a digital twin of a material, it is necessary to represent the complex hierarchy of features at the nano, micro, and macro-scale that contribute to the material performance.

Reference: [1] Kalidindi, S. R., Buzzy, M., Boyce, B. L., & Dingreville, R. (2022). Digital twins for materials. *Frontiers in Materials*, *9*, 818535.
DOI: https://doi.org/10.3389/fmats.2022.818535

1.2. Topological homogenization of metamaterial variability

With the proliferation of additive manufacturing and 3D printing technologies, a broader palette of material properties can be elicited from cellular solids, also known as metamaterials, architected foams, programmable materials, or lattice structures. Metamaterials are designed and optimized under the assumption of perfect geometry and a homogeneous underlying base material. Yet in practice real lattices contain thousands or even millions of complex features, each with imperfections in shape and material constituency. While the role of these defects on the mean properties of metamaterials has been well studied, little attention has been paid to the stochastic properties of metamaterials, a crucial next step for high reliability aerospace or biomedical applications. In this work we show that it is precisely the large quantity of features that serves to homogenize the heterogeneities of the individual features, thereby reducing the variability of the collective structure and achieving effective properties that can be even more consistent than the monolithic base material. In this first statistical study of additive lattice variability, a total of 239 strut-based lattices were mechanically tested for two pedagogical lattice topologies (body centered cubic and face centered cubic) at three different relative densities. The variability in yield strength and modulus was observed to exponentially decrease with feature count (to the power −0.5), a scaling trend that we show can be predicted using an analytic model or a finite element beam model. The latter provides an efficient pathway to extend the current concepts to arbitrary/complex geometries and loading scenarios. These results not only illustrate the homogenizing benefit of lattices, but also provide governing design principles that can be used to mitigate manufacturing inconsistencies via topological design.

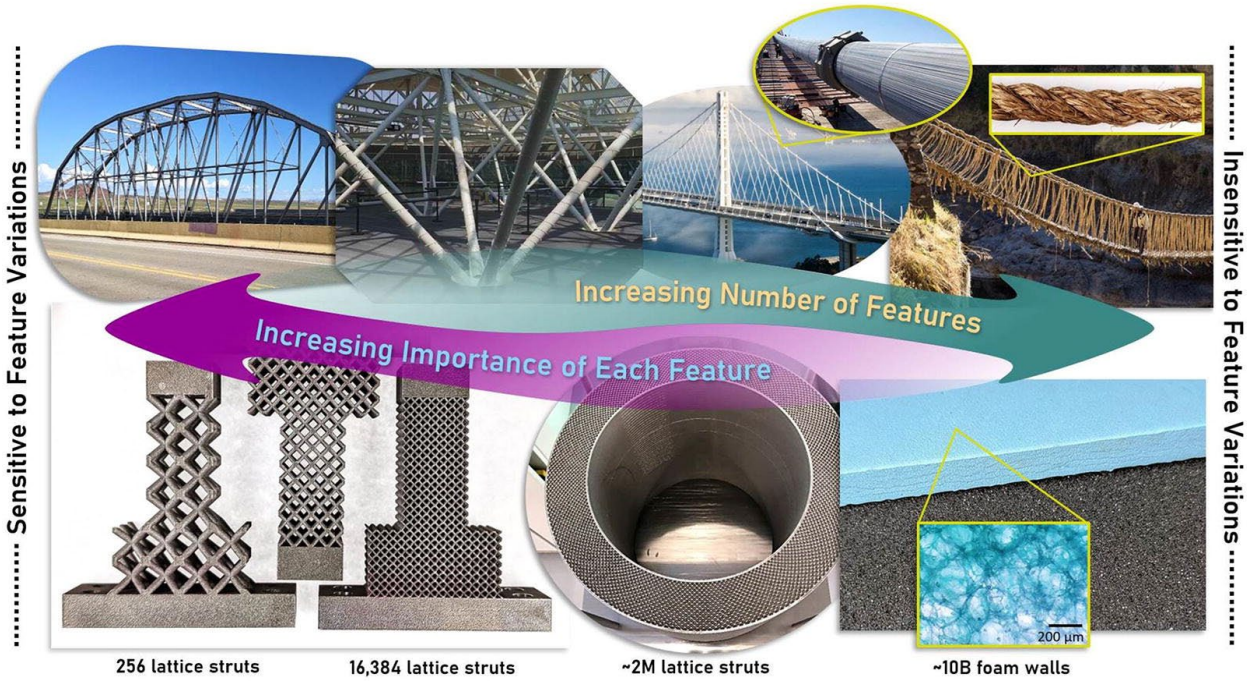

Figure 2. High-throughput testing allows rapid assessment of stochastic material variability. Here, applied to additively manufactured lattices, high-throughput testing reveals that the effective variability in material stiffness decreases as the number of unit cells increase due to a homogenization effect.

Reference: [2] White, B. C., Garland, A., & Boyce, B. L. (2022). Topological homogenization of metamaterial variability. *Materials Today*, *53*, 16-26.
DOI: https://doi.org/10.1016/j.mattod.2022.01.021

1.3. Accelerating phase-field predictions via recurrent neural networks learning the microstructural evolution in latent space

The phase-field method is a popular modeling technique used to describe the dynamics of microstructures and their physical properties at the mesoscale. However, because in these simulations the microstructure is described by a system of continuous variables evolving both in space and time, phase-field models are computationally expensive. They require refined spatio-temporal discretization and a parallel computing approach to achieve a useful degree of accuracy. As an alternative, we present and discuss an accelerated phase-field approach which uses a recurrent neural network (RNN) to learn the microstructure evolution in latent space. We perform a comprehensive analysis of different dimensionality-reduction methods and types of recurrent units in RNNs. Specifically, we compare statistical functions combined with linear and nonlinear embedding techniques to represent the microstructure evolution in latent space. We also evaluate several RNN models that implement a gating mechanism, including the long short-term memory (LSTM) unit and the gated recurrent unit (GRU) as the microstructure-learning engine. We analyze the different combinations of these methods on the spinodal decomposition of a two-phase system. Our comparison reveals that describing the microstructure evolution in latent space using an autocorrelation-based principal component analysis (PCA) method is the most efficient. We find that the LSTM and GRU RNN implementations provide comparable accuracy with respect to the high-fidelity phase-field predictions, but with a considerable computational speedup relative to the full simulation. This study not only enhances our understanding of the performance of dimensionality reduction on the microstructure evolution, but it also provides insights on strategies for accelerating phase-field modeling via machine learning techniques.

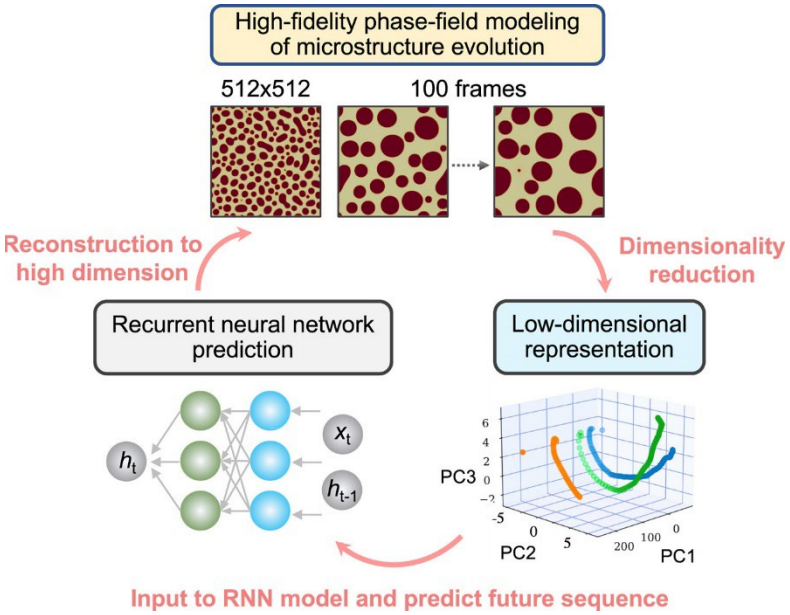

Figure 3. Schematic of a latent dynamic model workflow to accelerate materials simulations. This workflow consists of getting a low-dimensional presentation of the materials and then use this representation to learn and predict future sequence using a recurrent neural network.

Reference: [3] Hu, C., Martin, S., & Dingreville, R. (2022). Accelerating phase-field predictions via recurrent neural networks learning the microstructure evolution in latent space. *Computer Methods in Applied Mechanics and Engineering*, *397*, 115128.
DOI: https://doi.org/10.1016/j.cma.2022.115128

1.4. Learning time-dependent deposition protocols to design thin films via genetic algorithms

Designing next generation thin films tailor-made for specific applications relies on the availability of robust process-structure-property relationships. Traditional structure zone diagrams that relate one or two deposition conditions to microstructures are limited to simple mappings, with machine-learning methods only recently attempting to relate multiple processing parameters to the final microstructure. Despite this progress, process-structure relationships are unknown for deposition conditions that vary during thin-film deposition, limiting the range of achievable microstructures and properties. We combine phase-field simulations with a genetic algorithm to identify and design time-dependent deposition protocols that achieve tailor-made microstructures. We simulate the physical vapor deposition of a binary-alloy thin film by employing a phase-field model, where deposition rates and diffusivities of the deposited species vary in time and are controlled via the genetic algorithm. Our genetic-algorithm-guided protocols achieve targeted microstructures with lateral and vertical concentration modulations, as well as more complex, hierarchical microstructures previously not described in classical structure zone diagrams. By elucidating the process-structure mechanisms during physical vapor deposition and using this knowledge to achieve precise thin-film microstructures, our algorithm provides insights to the thin film, physical vapor deposition, and film functionality communities looking for additional avenues to design novel thin-film microstructures.

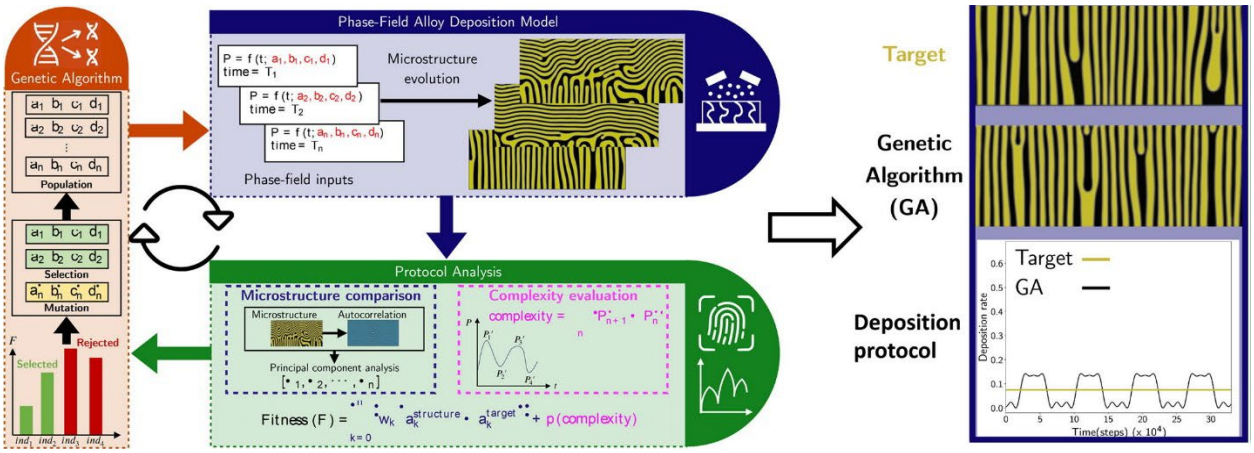

Figure 4. Workflow to discover novel (time-dependent) deposition protocols to achieve targeted microstructures. Deposition protocols are parameterized to describe any (time-dependent) protocol in terms of deposition rate. Those parameters are sampled and chose via a genetic algorithm which generate new deposition protocols. These protocols are used as input into deposition models yield associated microstructures. These microstructures are analyzed and compared to targeted microstructure for selection of new protocols by the genetic algorithm.

Reference: [4] Desai, S., & Dingreville, R. (2022). Learning time-dependent deposition protocols to design thin films via genetic algorithms. *Materials & Design*, *219*, 110815.
DOI: https://doi.org/10.1016/j.matdes.2022.110815

1.5. Microstructural black swans

Black swans are a metaphor for rare events with extreme consequences. In the domain of structural materials, black swans represent features in the microstructure that lead to catastrophic failure; as a result of their rarity, they are difficult to observe and often overlooked. These unusual weakest-link features are described variously as incipient, emergent, or anomalous. They give rise to localization, percolation, or avalanche events such as fracture, ductile rupture, dielectric breakdown, corrosion pit nucleation, and fatigue-crack initiation; as such, they are limiting cases in the concept of a representative volume. In this perspective, three examples are given of rare microstructural features and how they limit the mechanical reliability of structural metals. After taking stock of these examples, a future outlook considers the need for high-throughput testing and non-destructive characterization as well as detection algorithms and materials modelling strategies, including accelerated machine learning methods, that can capture anomalous events.

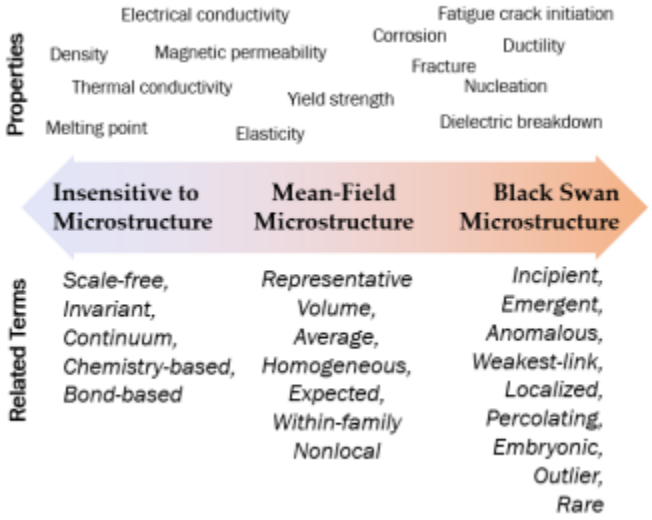

Figure 5. Some material properties like fatigue crack initiation and corrosion pit nucleation are difficult to predict because they appear to be highly stochastic, triggered at rare "weakest-links" in the microstructure.

Reference: [5] Boyce, B. L. (2022, July). Microstructural black swans. In *IOP conference series: materials science and engineering* (Vol. 1249, No. 1, p. 012004). IOP Publishing.
DOI: https://doi.org/10.1088/1757-899X/1249/1/012004

1.6. Learning two-phase microstructure evolution using DeepONet and autoencoder architectures

Phase-field modeling is an effective but computationally expensive method for capturing the mesoscale morphological and microstructure evolution in materials. Hence, fast and generalizable surrogate models are needed to alleviate the cost of computationally taxing processes such as in optimization and design of materials. The intrinsic discontinuous nature of the physical phenomena incurred by the presence of sharp phase boundaries makes the training of the surrogate model cumbersome. We develop a framework that integrates a convolutional autoencoder architecture with a deep neural operator (DeepONet) to learn the dynamic evolution of a two-phase mixture and accelerate time-to-solution in predicting the microstructure evolution. We utilize the convolutional autoencoder to provide a compact representation of the microstructure data in a low-dimensional latent space. After DeepONet is trained in the latent space, it can be used to replace the high-fidelity phase-field numerical solver in interpolation tasks or to accelerate the numerical solver in extrapolation tasks.

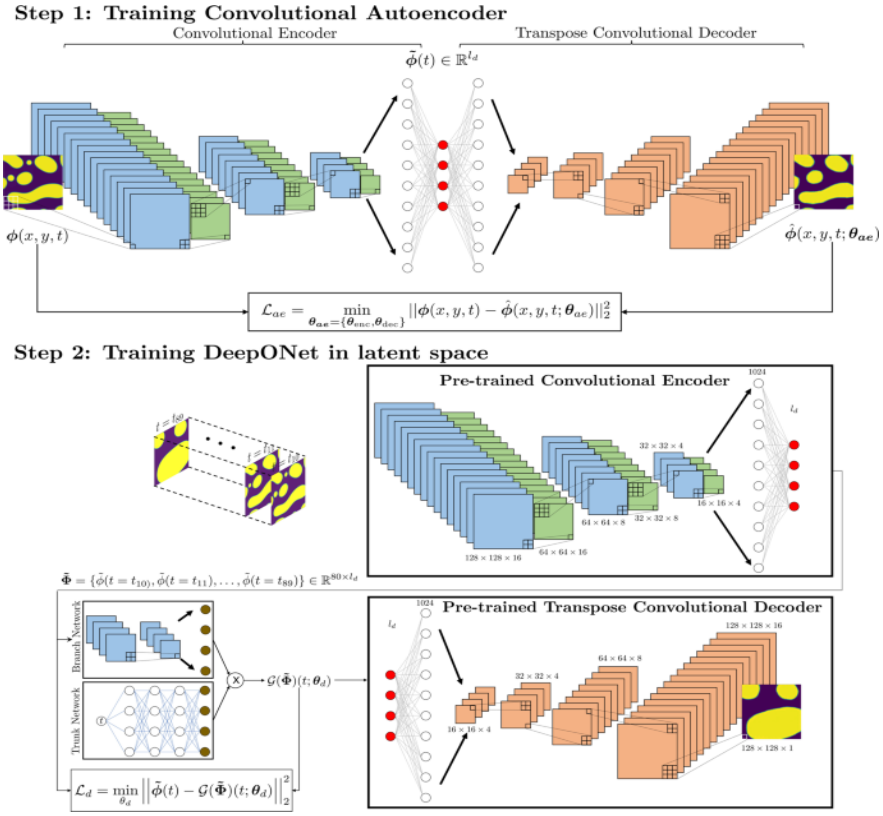

Figure 6. Accelerating materials simulation using physics-informed neural network. A convolutional autoencoder is trained to embed the description of the microstructure. The latent description of the microstructure obtained from the autoencoder is then use in a DeepONet to accelerate and predict future time sequences.

Reference: [6] Oommen, V., Shukla, K., Goswami, S., Dingreville, R., & Karniadakis, G. E. (2022). Learning two-phase microstructure evolution using neural operators and autoencoder architectures. *npj Computational Materials*, *8*(1), 190.
DOI: https://doi.org/10.1038/s41524-022-00876-7

1.7. Inferring topological phase transitions in pattern-forming processes with self-learning

The identification of transitions in pattern-forming processes are critical to understand and fabricate microstructurally precise materials in many application domains. While supervised methods can be useful to identify transition regimes, they need labels, which require prior knowledge of order parameters or relevant microstructures describing these transitions. Instead, we develop a self-supervised, neural-network-based approach that does not require predefined labels about microstructure classes to predict process parameters from observed microstructures. We show that assessing the difficulty of solving this inverse problem can be used to uncover microstructural transitions. We demonstrate our approach by automatically discovering microstructural transitions in two distinct pattern-forming processes: the spinodal decomposition of a two-phase mixture and the formation of binary-alloy microstructures during physical vapor deposition of thin films. This approach opens a path forward for discovering unseen or hard-to-discern transitions and ultimately controlling complex pattern-forming processes.

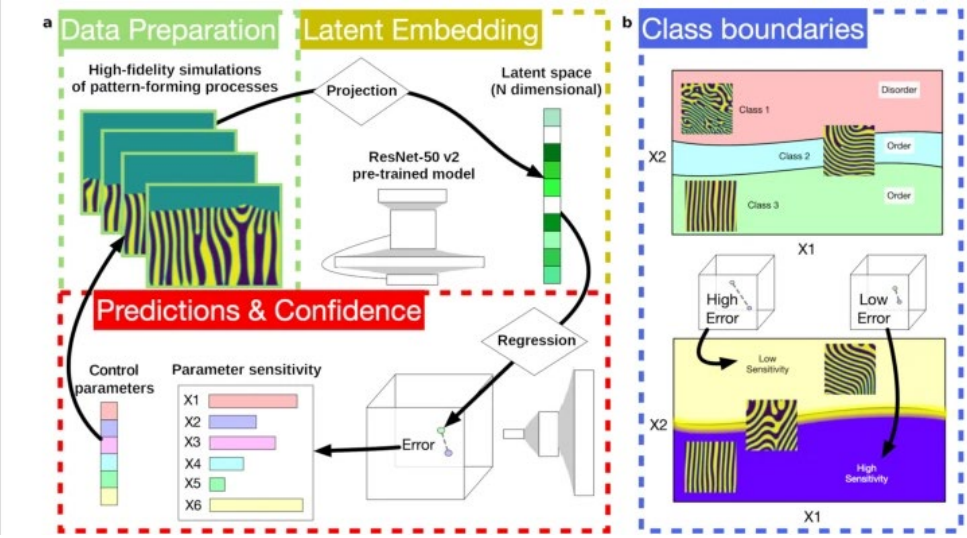

Figure 7. Workflow to identify transition regimes in pattern-forming processes via self-supervised learning. a We simulate the dynamical evolution of the physical system for a broad range of process parameters. Next, we project the final state of the microstructural pattern into a latent space (using a pre-trained ResNet-50 v235). We regress on these latent dimensions to estimate the original process parameters. b To detect specific classes of microstructural patterns, we evaluate the model error by predicting the corresponding initial process parameters. By measuring the change in sensitivity of forming specific patterns for various input process parameters, we learn where the transition regime(s) might occur.

Reference: [7] Abram, M., Burghardt, K., Ver Steeg, G., Galstyan, A., & Dingreville, R. (2022). Inferring topological transitions in pattern-forming processes with self-supervised learning. *npj Computational Materials*, *8*(1), 205.
DOI: https://doi.org/10.1038/s41524-022-00889-2

1.8. Optimization of Stochastic Feature Properties in Laser Powder Bed Fusion

Process parameter selection in laser powder bed fusion (LPBF) controls the as-printed dimensional tolerances, pore formation, surface quality and microstructure of printed metallic structures. Measuring the stochastic mechanical performance for a wide range of process parameters is cumbersome both in time and cost. In this study, we overcome these hurdles by using high-throughput tensile (HTT) testing of over 250 dogbone samples to examine process-driven performance of strut-like small features, ~1 mm2 in austenitic stainless steel (316 L). The output mechanical properties, porosity, surface roughness and dimensional accuracy were mapped across the printable range of laser powers and scan speeds using a continuous wave laser LPBF machine. Tradeoffs between ductility and strength are shown across the process space and their implications are discussed. While volumetric energy density deposited onto a substrate to create a melt-pool can be a useful metric for determining bulk properties, it was not found to directly correlate with output small feature performance.

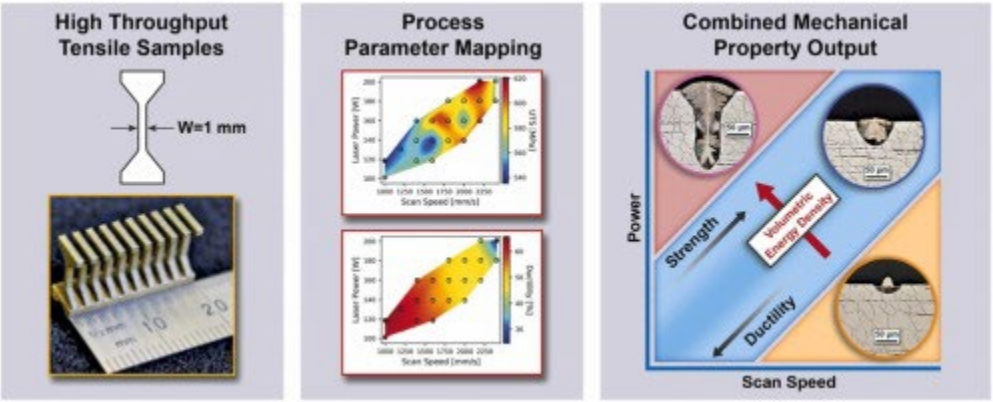

Figure 8. High-throughput tensile testing contributes to rapid optimization of process parameters in additive manufacturing. Other researchers typically lack this mechanical performance data during optimization, and instead optimize for density or printability.

Reference: [8] Jensen, S. C., Koepke, J. R., Saiz, D. J., Heiden, M. J., Carroll, J. D., Boyce, B. L., & Jared, B. H. (2022). Optimization of stochastic feature properties in laser powder bed fusion. *Additive Manufacturing*, *56*, 102943.
DOI: https://doi.org/10.1016/j.addma.2022.102943

1.9. Part-scale Process Modeling for Metal Additive Manufacturing, submitted ASM Handbook, 2022.

This article provides an overview of different modeling approaches used to capture the phenomena present in the additive manufacturing (AM) process. Inherent to the thermomechanical processing that occurs in AM for metals is the development of residual stresses and distortions. The article then provides an overview of thermal modeling. It presents a discussion on solid mechanics simulation and microstructure simulation.

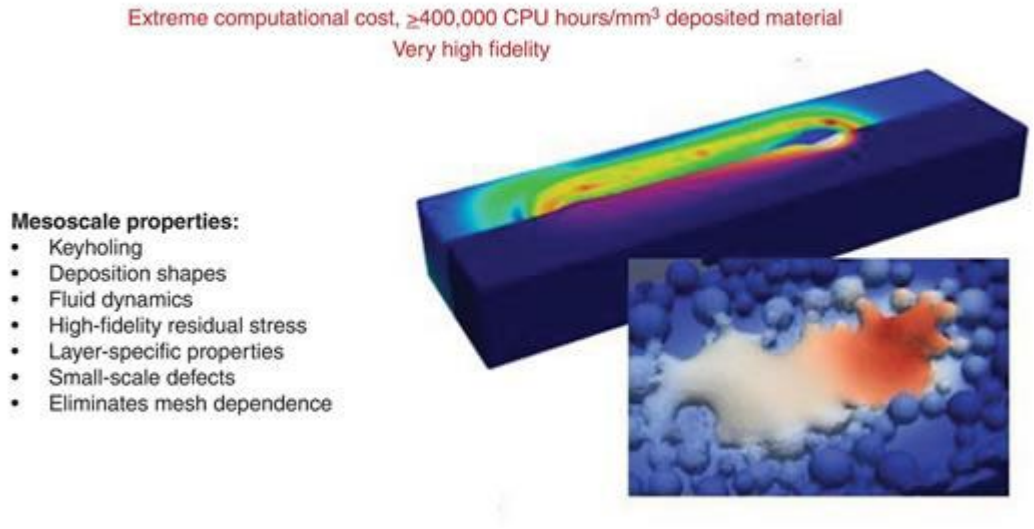

Figure 9. Explicit High-Fidelity simulation of additive manufacturing processes requires enormous computational resources, rendering extensive parametric studies infeasible. Future surrogate models trained on limited simulation data will allow speed-up of such predictions, albeit with reduced fidelity.

Reference: [9] Johnson, K. L., Moser, D., Rodgers, T. M., & Stender, M. E. (2023). Part-Scale Process Modeling for Metal Additive Manufacturing. In *Additive Manufacturing Design and Applications* (pp. 67-73). ASM International.

DOI: https://doi.org/10.31399/asm.hb.v24A.a0006976

1.10. Long-term process stability in additive manufacturing

Laser powder bed fusion (LPBF), also known as selective laser sintering or direct laser melting, is an additive manufacturing process in which part geometries are formed simultaneously with the underlying material. The microstructure, defect content, and surface quality are all synthesized conjointly with the part shape. While the geometric design freedom allowed by this process enables new complex features and parts with small (~1 mm) features, challenges associated with process qualification can deter wider adoption. Furthermore, a lack of historical performance data for statistical process control of witness coupons, for either bulk material or for small features, makes the barrier to entry more difficult. Here, we demonstrate long-term, property-based process monitoring and variability assessment using both small-featured (1 mm) and larger, bulk-representative material witness coupons. Over a one-year period, more than 550 tensile bars and 80 Charpy impact bars were printed alongside 316 L stainless steel parts built using LPBF and tested to detect shifts in the process over time. Miniature tensile bars with a 1 mm2 gage area were tested using a high throughput mechanical testing system. In parallel, a larger test coupon was used to monitor density, hardness, and Charpy impact toughness. This collection of measurements was used to determine detectable property shifts correlated to LPBF process changes including powder feedstock, machine hardware, software versioning, and machine parameter settings. The benefits of using small featured, high-throughput samples are discussed based on process sensitivity and the number of repeat tests possible for each build. This study not only reveals the utility of property-based process monitoring but illustrates the sensitivity of these measurements to detect process changes and provides further evidence for property stability in modern LPBF.

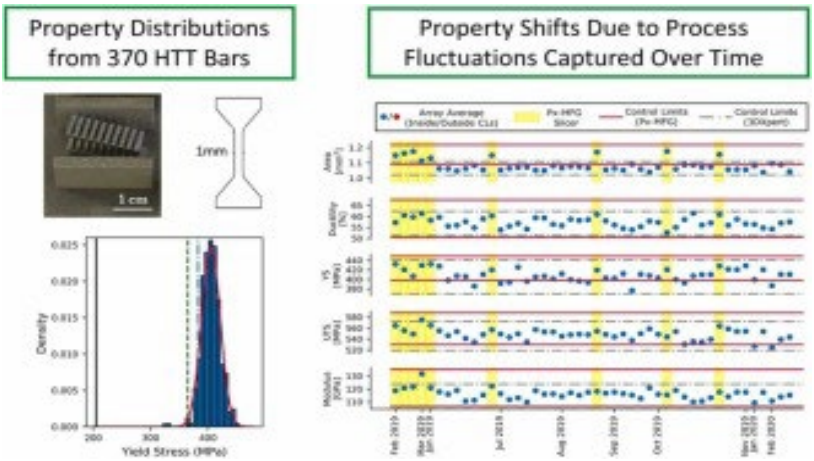

Figure 10. High-throughput tension testing enables a new level of insight into the long-term repeatability of additive manufacturing processes. Rarely if ever do other organizations have access to such extensive mechanical property data, collected consistently over years of process usage.

Reference: [10] Jensen, S. C., Carroll, J. D., Pathare, P. R., Saiz, D. J., Pegues, J. W., Boyce, B. L., ... & Heiden, M. J. (2023). Long-term process stability in additive manufacturing. *Additive Manufacturing*, *61*, 103284.

DOI: https://doi.org/10.1016/j.addma.2022.103284

1.11. Process-microstructure relationships of physical vapor deposited polycrystalline thin films via a multi-phase-field formulation.

We present a generalized multi-phase-field model to predict the growth of polycrystalline thin films fabricated by physical vapor deposition. The model accounts for the explicit transport of atomic species to the substrate and the competing diffusion processes on the surface and in the bulk of the film leading to the formation of films with specific microstructures. We used magnetron sputtering conditions (pressure, voltage, working distance, substrate orientation) to calculate the energy and direction of the arriving atoms at the substrate using Monte Carlo simulations with the SiMTRA code. Our simulation results capture the dependence of the microstructure on deposition conditions, and delineate the relationship between process parameters and the formation of columnar microstructures and surface roughness characteristic of thin films. These simulation predictions are in agreement with transmission electron microscopy characterization of sputtered films. Through our systematic investigation of competing growth mechanisms, we provide insights into the complex relationships between deposition conditions and bulk and surface morphologies.

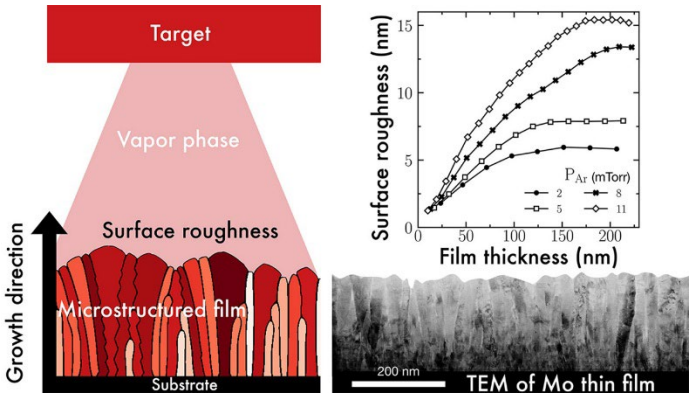

Figure 11. Phase-field simulations of physical vapor deposition of thin film. Left panel illustrates the various components of the model and features captured by the model. Right panel shows a comparison with TEM cross section of the same microstructure. Model is able to accurately predict the evolution of the morphology of the microstructure as a function of deposition conditions and thickness of the film.

Reference: [11] Monti, J. M., Stewart, J. A., Custer, J. O., Adams, D. P., Depla, D., & Dingreville, R. (2023). Linking simulated polycrystalline thin film microstructures to physical vapor deposition conditions. *Acta Materialia*, *245*, 118581.
DOI: https://doi.org/10.1016/j.actamat.2022.118581

1.12. Learning incoherent light emission steering from metasurfaces using generative models

Spatiotemporal control over incoherent light sources is critically important for applications such as displays, remote sensing, clean energy, and illumination. Incoherent light emission made up of randomized wavefronts is incompatible with known beam steering techniques that rely on coherent electromagnetic wave interference. The emerging field of tunable dielectric metasurfaces consisting of sub- wavelength arrays of optical nanoresonators has recently enabled active re-direction of incoherent light (photoluminescence, PL) emission. This was achieved by illuminating (pumping) the metasurface with a pump laser reflecting off a programmable spatial light modulator (SLM) with sawtooth grating patterns as input. Achieving efficient beam steering requires the generation of optimal pump patterns programmed into the SLM to maximize the PL emitted towards a given direction. Given the innumerable possibilities and the lack of a theoretical physical framework to guide the exploration of pump patterns, we use an active learning algorithm running a closed loop optical experiment with a generative model to explore and optimize novel pump patterns. We achieve up to an order of magnitude enhancement in the steering efficiency by using pump patterns that are generated by a variational auto-encoder, with minimal number of experiments. The results presented in this paper highlight the unique ability of generative models and active learning to dramatically improve steering efficiency by finding novel optical pump patterns that are beyond human intuition. Our combination of advanced machine learning techniques driving closed loop nanophotonic experiments might pave the way to derive the underlying physics of emergent light-matter phenomena.

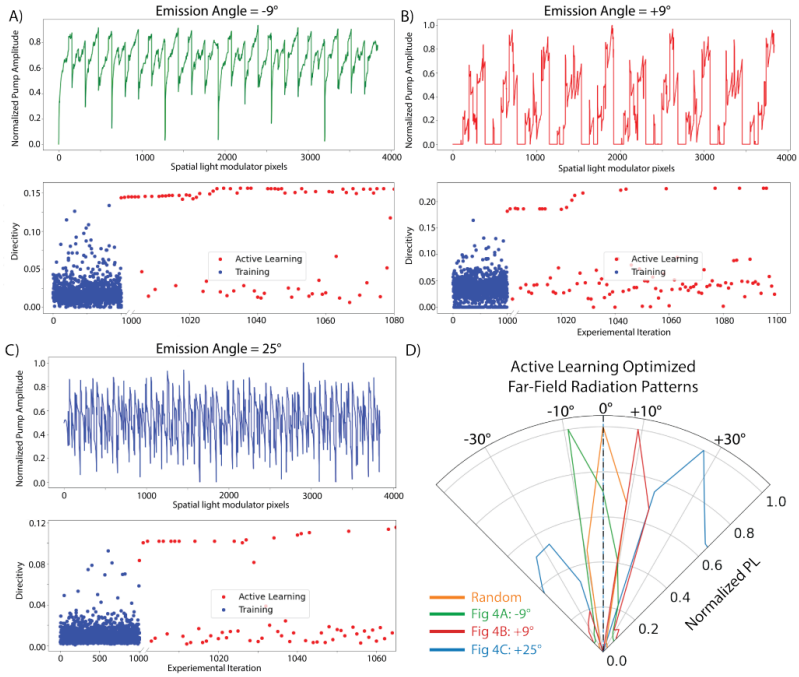

Figure 12. Generative models combined with equation learner can learn how to steer light from fast and high-throughput experiments.

Reference: [12] Iyer, P. P., Desai, S., Addamane, S., Dingreville, R., & Brener, I. (2023). Learning incoherent light emission steering from metasurfaces using generative models. In *Proceedings of the IEEE/CVF Winter Conference on Applications of Computer Vision* (pp. 3770-3777).

1.13. Connecting vibrational spectroscopy to atomic structure via supervised manifold learning: beyond peak analysis

Vibrational spectroscopy is a nondestructive technique commonly used in chemical and physical analyses to determine atomic structures and associated properties. However, the evaluation and interpretation of spectroscopic profiles based on human-identifiable peaks can be difficult and convoluted. To address this challenge, we present a reliable protocol based on supervised manifold learning techniques meant to connect vibrational spectra to a variety of complex and diverse atomic structure configurations. As an illustration, we examined a large database of virtual vibrational spectroscopy profiles generated from atomistic simulations for silicon structures subjected to different stress, amorphization, and disordering states. We evaluated representative features in those spectra via various linear and nonlinear dimensionality reduction techniques and used the reduced representation of those features with decision trees to correlate them with structural information unavailable through classical human-identifiable peak analysis. We show that our trained model accurately (over 97% accuracy) and robustly (insensitive to noise) disentangles the contribution from the different material states, hence demonstrating a comprehensive decoding of spectroscopic profiles beyond classical (human-identifiable) peak analysis.

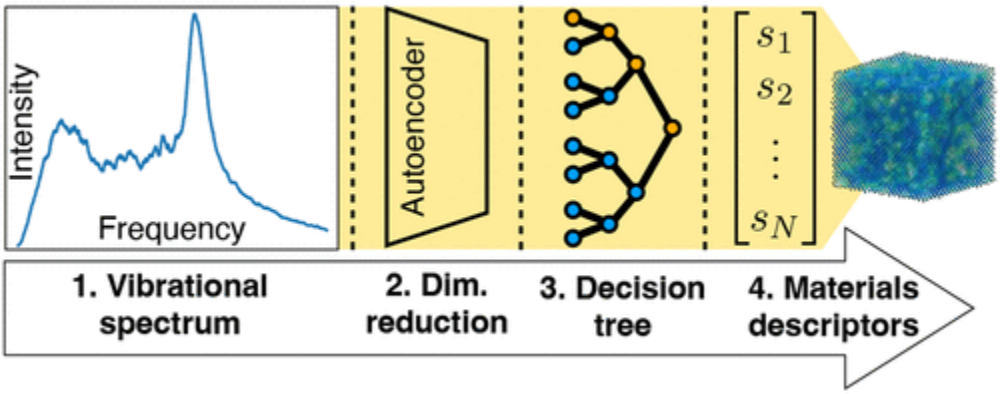

Figure 13. We extracted materials state descriptors beyond classical peak-width analysis through a machine-learned approach which takes as input an observed vibrational spectroscopy spectrum and outputs a vector describing stress and strain full tensors, fraction of disorder, internal length scale associated with disorder. The workflow consists of first reducing the dimensionality of the vibrational spectrum via an autoencoder, then use the latent representation of the spectrum into a regression model (in the present case a decision tree) to regress the state of the materials.

Reference: [13] Vizoso, D., Subhash, G., Rajan, K., & Dingreville, R. (2023). Connecting vibrational spectroscopy to atomic structure via supervised manifold learning: Beyond peak analysis. *Chemistry of Materials*, *35*(3), 1186-1200.
DOI: https://doi.org/10.1021/acs.chemmater.2c03207

1.14. Machine Learning for Materials Science: Barriers to Broader Adoption

Machine learning is on a bit of a tear right now, with advances that are infiltrating nearly every aspect of our lives. In the domain of materials science, this wave seems to be growing into a tsunami. Yet, there are still real hurdles that we face to maximize its benefit. This Matter of Opinion, crafted as a result of a workshop hosted by researchers at Sandia National Laboratories and attended by a cadre of luminaries, briefly summarizes our perspective on these barriers. By recognizing these problems in a community forum, we can share the burden of their resolution together with a common purpose and coordinated effort.

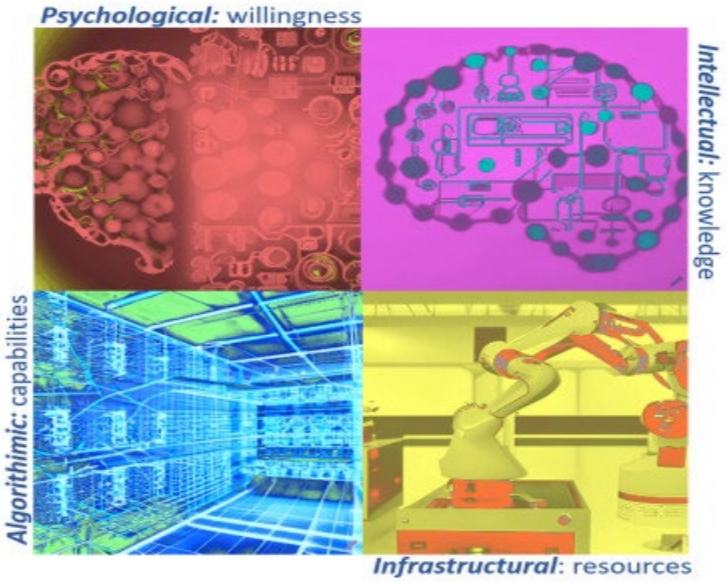

Figure 14. There are four basic categories that create barriers to the efficient usage of machine learning algorithms in materials science: (1) psychological trust, (2) intellectual awareness of available algorithms and their proper usage, (3) availability of infrastructural capabilities for both data collection and data analysis at a large scale, and (4) in some cases, existing algorithms must be modified to accommodate the data sources and embed physics knowledge.

Reference: [14] Boyce, B., Dingreville, R., Desai, S., Walker, E., Shilt, T., Bassett, K. L., ... & Warren, J. A. (2023). Machine learning for materials science: Barriers to broader adoption. *Matter*, *6*(5), 1320-1323.
DOI: https://doi.org/10.1016/j.matt.2023.03.028

1.15. Sputtered-deposited Mo thin films: Multimodal characterization of structure, surface morphology, density, residual stress, electrical resistivity and mechanical response

Multimodal datasets of materials are rich sources of information which can be leveraged for expedited discovery of process–structure–property relationships and for designing materials with targeted structures and/or properties. For this data descriptor article, we provide a multimodal dataset of magnetron sputter-deposited molybdenum (Mo) thin films, which are used in a variety of industries including high temperature coatings, photovoltaics, and microelectronics. In this dataset we explored a process space consisting of 27 unique combinations of sputter power and Ar deposition pressure. The phase, structure, surface morphology, and composition of the Mo thin films were characterized by x-ray diffraction, scanning electron microscopy, atomic force microscopy, and Rutherford backscattering spectrometry. Physical properties—namely, thickness, film stress and sheet resistance—were also measured to provide additional film characteristics and behaviors. Additionally, nanoindentation was utilized to obtain mechanical load-displacement data. The entire dataset consists of 2072 measurements including scalar values (e.g., film stress values), 2D linescans (e.g., x-ray diffractograms), and 3D imagery (e.g., atomic force microscopy images). An additional 1889 quantities, including film hardness, modulus, electrical resistivity, density, and surface roughness, were derived from the experimental datasets using traditional methods. Minimal analysis and discussion of the results are provided in this data descriptor article to limit the authors' preconceived interpretations of the data. Overall, the data modalities are consistent with previous reports of refractory metal thin films, ensuring that a high-quality dataset was generated. The entirety of this data is committed to a public repository in the Materials Data Facility.

Figure 15. A summary of the 2,072 measurements performed on a combinatorial library of pure Mo films deposited under a range of conditions and characterized via several complementary modalities.

Reference: [15] Kalaswad, M., Custer, J. O., Addamane, S., Khan, R. M., Jauregui, L., Babuska, T. F., ... & Adams, D. P. (2023). Sputter-deposited Mo Thin films: multimodal characterization of structure, surface morphology, density, residual stress, electrical resistivity, and mechanical response. *Integrating Materials and Manufacturing Innovation*, *12*(2), 118-129.
DOI: https://doi.org/10.1007/s40192-023-00297-4

1.16. Revealing the structure-property relationships of amorphous carbon tribofilms on platinum-gold surfaces

Nanocrystalline metal alloys have shown great promise as electrical contact materials, given their mechanical and tribological properties. In particular, platinum-gold (Pt–Au) nanocrystalline alloys have demonstrated coefficients of friction as low as 0.01 and specific wear rates on the order of 10−9 mm3 N−1 m−1, largely due to the formation of carbon-based tribofilms at the sliding interfaces. In this study, we advance our understanding of the Pt–Au tribofilm structure-property relations and growth mechanisms via high-throughput and high-resolution measurements as a function of Pt–Au composition. As the solute content increased from 0 at. % to 10 at. % Au, cross-sectional and plan-view transmission electron microscopy demonstrated a decrease in average grain size d and an accompanied increase in grain boundary (GB) segregation. The decrease in d and increase in GB solute segregation translated to a decrease in modulus Er and an increase in hardness H as determined via nanoindentation; the Er trend was mainly described using a rule-of-mixtures approximation, whereas the H trend was ascribed to solid solution strengthening and GB stabilization. The steady state-friction μ and wear rate decreased with the addition of Au; low Au-content films showed substrate wear, while high Au-content films showed stable tribofilm growth in both macroscale and nanoscale friction tests. The carbon bonding configuration of the tribofilms was investigated by near-edge X-ray absorption fine structure spectroscopic analyses and found to be similar to that of hydrogenated amorphous carbon films. Altogether, the study provided insight into the mechanistic origins of the tribofilms, thus opening the door to tunable properties ranging from mitigation for electrical contacts to the creation of self-healing films for solid lubricants.

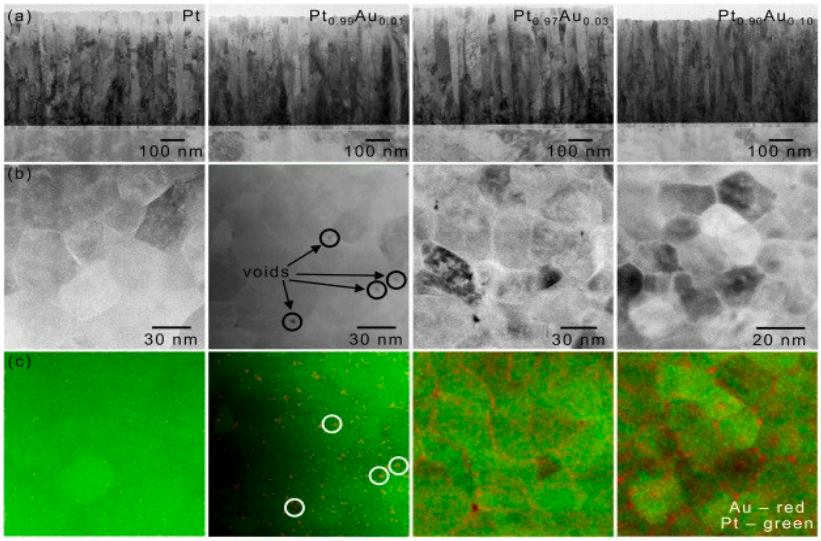

Figure 16. (top row) Cross-sectional images of as-deposited films, (middle row) plan view images, and (bottom row) corresponding STEM-EDS composition maps, revealing gold segregation at grain boundaries.

Reference: [16] DelRio, F. W., Mangolini, F., Edwards, C. E., Babuska, T. F., Adams, D. P., Lu, P., & Curry, J. F. (2023). Revealing the structure-property relationships of amorphous carbon tribofilms on platinum-gold surfaces. *Wear*, *522*, 204690.
DOI: https://doi.org/10.1016/j.wear.2023.204690

1.17. Automated high-throughput fatigue testing of freestanding thin films

Mechanical testing at small length scales has traditionally been resource-intensive due to difficulties with meticulous sample preparation, exacting load alignments, and precision measurements. Microscale fatigue testing can be particularly challenging due to the time-intensive, tedious repetition of single fatigue experiments. To mitigate these challenges, this work presents a new methodology for the high-throughput fatigue testing of thin films at the microscale. This methodology features a microelectromechanical systems-based Si carrier that can support the simultaneous and independent fatigue testing of an array of samples. To demonstrate this new technique, the microscale fatigue behavior of nanocrystalline Al is efficiently characterized via this Si carrier and automated fatigue testing with in situ scanning electron microscopy. This methodology reduces the total testing time by an order of magnitude, and the high-throughput fatigue results highlight the stochastic nature of the microscale fatigue response. This manuscript also discusses how this initial capability can be adapted to accommodate more samples, different materials, new geometries, and other loading modes.

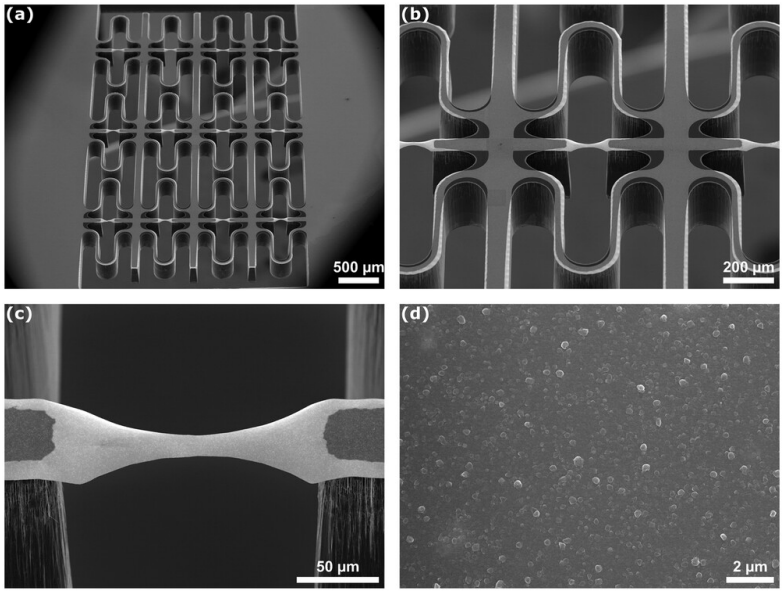

Figure 17. A Si Micro-Electro-Mechanical system (MEMS)-based platform enables the simultaneous fatigue testing of up to 12 thin-film tensile bars, with concurrent automated imaging of fatigue damage progression in the Scanning Electron Microscope (SEM).

Reference: [17] Barrios, A., Kunka, C., Nogan, J., Hattar, K., & Boyce, B. L. (2023). Automated High-Throughput Fatigue Testing of Freestanding Thin Films. *Small Methods*, *7*(7), 2201591.
DOI: https://doi.org/10.1002/smtd.202201591

1.18. A Workflow for Accelerating Multimodal Data Collection for Electrodeposited Films

Future machine learning strategies for materials process optimization will likely replace human capital-intensive artisan research with autonomous and/or accelerated approaches. Such automation enables accelerated multimodal characterization that simultaneously minimizes human errors, lowers costs, enhances statistical sampling, and allows scientists to allocate their time to critical thinking instead of repetitive manual tasks. Previous acceleration efforts to synthesize and evaluate materials have often employed elaborate robotic self-driving laboratories or used specialized strategies that are difficult to generalize. Herein we describe an implemented workflow for accelerating the multimodal characterization of a combinatorial set of 915 electroplated Ni and Ni–Fe thin films resulting in a data cube with over 160,000 individual data files. Our acceleration strategies do not require manufacturing-scale resources and are thus amenable to typical materials research facilities in academic, government, or commercial laboratories. The workflow demonstrated the acceleration of six characterization modalities: optical microscopy, laser profilometry, X-ray diffraction, X-ray fluorescence, nanoindentation, and tribological (friction and wear) testing, each with speedup factors ranging from 13–46x. In addition, automated data upload to a repository using FAIR (Findable, Accessible, Interoperable, Reusable) data principles was accelerated by 64x.

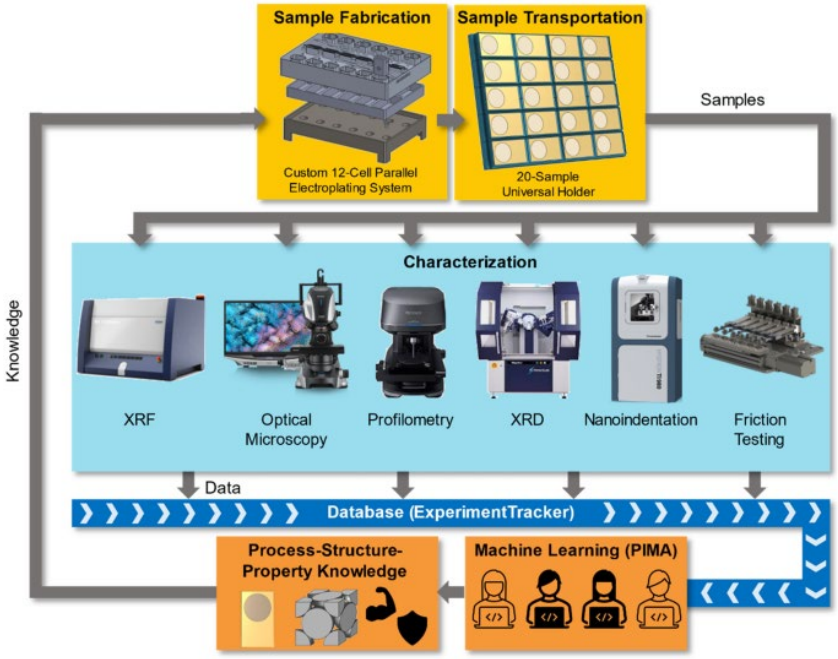

Figure 18. An accelerated electroplating workflow uses custom parallel combinatorial synthesis and a multi-sample holder, loaded into 6 automated instruments ranging from X-ray Flourescence to Nanoindentation.

Reference: [18] Bassett, K. L., Watkins, T., Coleman, J., Bianco, N., Bailey, L. S., Pillars, J., ... & Boyce, B. L. (2023). A Workflow for Accelerating Multimodal Data Collection for Electrodeposited Films. *Integrating Materials and Manufacturing Innovation*, *12*(4), 430-440.
DOI: https://doi.org/10.1007/s40192-023-00315-5

1.19. Latent representation of microstructure evolution: a survey

Characterizing and quantifying microstructure evolution is critical to forming quantitative relationships between material processing conditions, resulting microstructure, and observed properties. Machine-learning methods are increasingly accelerating the development of these relationships by treating microstructure evolution as a pattern recognition problem, discovering relationships explicitly or implicitly. These methods often rely on identifying low-dimensional microstructural fingerprints as latent variables. However, using inappropriate latent variables can lead to challenges in learning meaningful relationships. In this work, we survey and discuss the ability of various linear and nonlinear dimensionality reduction methods including principal component analysis, autoencoders, and diffusion maps to quantify and characterize the learned latent space microstructural representations and their time evolution. We characterize latent spaces by their ability to represent high-dimensional microstructural data in terms of compression achieved as a function of the number of latent dimensions required to represent the data accurately, their accuracy based on their reconstruction performance, and the smoothness of the microstructural trajectories in latent dimension. We quantify these metrics for common microstructure evolution problems in material science including spinodal decomposition of a binary metallic alloy, thin film deposition of a binary metallic alloy, dendritic growth, and grain growth in a polycrystal. This study provides considerations and guidelines for choosing dimensionality reduction methods when considering materials problems that involve high dimensional data and a variety of features over a range of lengths and time scales.

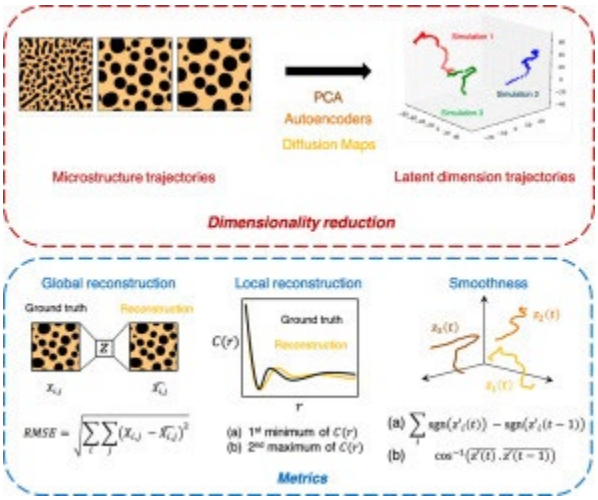

Figure 19. Latent representation of microstructure via various machine-learning algorithms (e.g. autoencoders, principal component analysis, diffusion maps) are evaluated in terms of the ability of the machine-learning strategy to (i) reconstruct the microstructure from its latent representation, both in terms of local and global features; and (ii) the ability to describe smooth microstructure evolution trajectory in the latent space. Smoothness of the latent representation of the microstructure as a function of time is important for adaption and control of those microstructure when linked with process conditions.

Reference: [19] Desai, S., Shrivastava, A., D'Elia, M., Najm, H. N., & Dingreville, R. (2024). Trade-offs in the latent representation of microstructure evolution. *Acta Materialia*, *263*, 119514.

DOI: https://doi.org/10.1016/j.actamat.2023.119514

1.20. Beyond Combinatorial Materials Science – The 100 Prisoners Problem

Advancements in high-throughput data generation and physics-informed artificial intelligence and machine-learning algorithms are rapidly challenging the status quo for how materials data is collected, analyzed, and communicated with the world. Machine-learning algorithms can be executed in just a few lines of code by researchers with minimal data science expertise. This perspective addresses the reality that the ecosystems which have been constructed to nurture new materials discovery and development are not yet well equipped to take advantage of the radically more powerful and accessible computational and algorithmic tools which have the immediate potential to enhance the pace of scientific advancement in this field. A novel architecture for managing materials data is proposed and discussed from the standpoint of how historical and emerging subfields of materials science could have been or might still significantly improve the impact of materials discoveries to the many human societal needs for new materials.

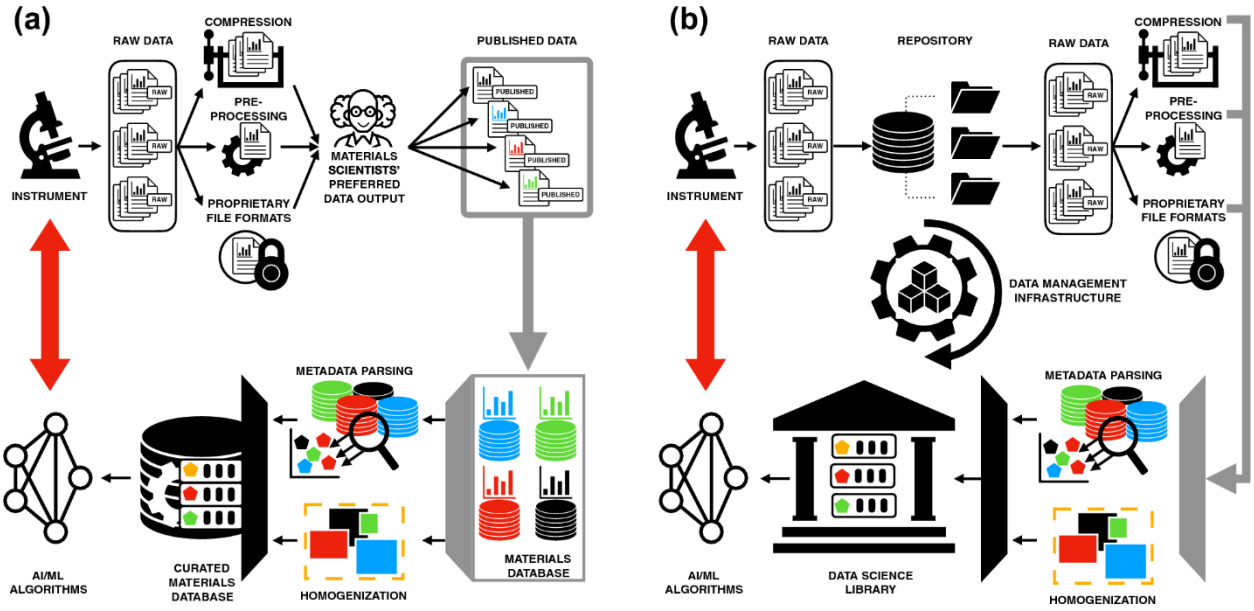

Figure 20. (a) a typical workflow where measurements, interpretation, and even publication can be disconnected from data sharing and advanced analytics, (b) a future workflow where data sharing via a FAIR repository and advanced analysis can occur automatically in conjunction with data collection.

Reference: [20] Fowler, J. E., Kottwitz, M. A., Trask, N., & Dingreville, R. (2024). Beyond Combinatorial Materials Science: The 100 Prisoners Problem. *Integrating Materials and Manufacturing Innovation*, *13*(1), 83-91.
DOI: https://doi.org/10.1007/s40192-023-00330-6

1.21. Reconstruction of high-resolution atomic force microscopy measurements from fast-scan data using a Noise2Noise algorithm

The acquisition of large atomic-force-microscopy (AFM) scans at nanoscale resolutions can take hours and produce datasets with millions of pixels, which is time consuming and computationally expensive to analyze. In this paper, we present an approach to speed up this process by using a computer-vision algorithm, namely the Noise2Noise algorithm, to reconstruct high-resolution, low scan speed AFM data from high-speed, noisy, sparsely sampled AFM data. This algorithm is trained on various noise types to reproduce different sources of experimental noises encountered during the acquisition of AFM data. Our results demonstrate that a sparse, uniform AFM scan of 20× 20 μ m at 128× 128 pixel resolution can be processed within seconds, and the output image is comparable to a higher quality raw data scan which required 30 min or more to collect, reducing not only the acquisition and analysis time, but also the size of the data being collected.

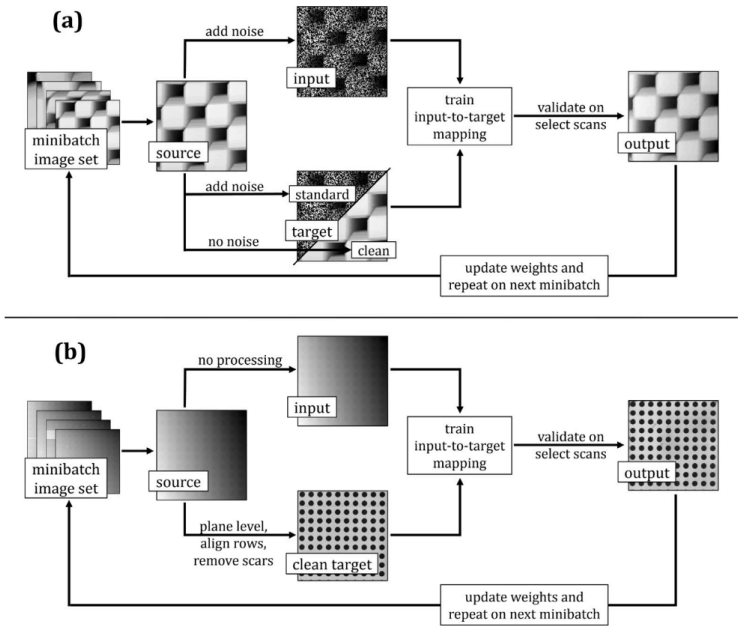

Figure 21. We used a Noise2Noise (N2N) algorithms to reconstruct high-resolution atomic force microscopy (AFM) images from noisy AFM images. (a) One target AFM image corresponds to a high-resolution 'clean' image and the other corresponds to a 'noisy' sparsely sampled image. We used different types of noise to train the network. (b) Once trained, we employed this algorithm to take scans at fast scan speeds and lower sampling density to reconstruct the corresponding slow-scan AFM image, significantly reducing scan time and decreasing processing complexity. The results demonstrate that it is possible to reconstruct high-resolution scans from sparse or noisy AFM images with minimal time and computational requirements.

Reference: [21] Natinsky, E., Khan, R. M., Cullinan, M., & Dingreville, R. (2024). Reconstruction of high-resolution atomic force microscopy measurements from fast-scan data using a Noise2Noise algorithm. *Measurement*, *227*, 114263.

DOI: https://doi.org/10.1016/j.measurement.2024.114263

1.22. AI for Technoscientific Discovery: A Human-Inspired Architecture

We present a high-level architecture for how artificial intelligences might advance and accumulate scientific and technological knowledge, inspired by emerging perspectives on how human intelligences advance and accumulate such knowledge. Agents advance knowledge by exercising a technoscientific method—an interacting combination of scientific and engineering methods. The technoscientific method maximizes a quantity we call "useful learning" via more-creative implausible utility (including the "aha!" moments of discovery), as well as via less-creative plausible utility. Society accumulates the knowledge advanced by agents so that other agents can incorporate and build on to make further advances. The proposed architecture is challenging but potentially complete: its execution might in principle enable artificial intelligences to advance and accumulate an equivalent of the full range of human scientific and technological knowledge.

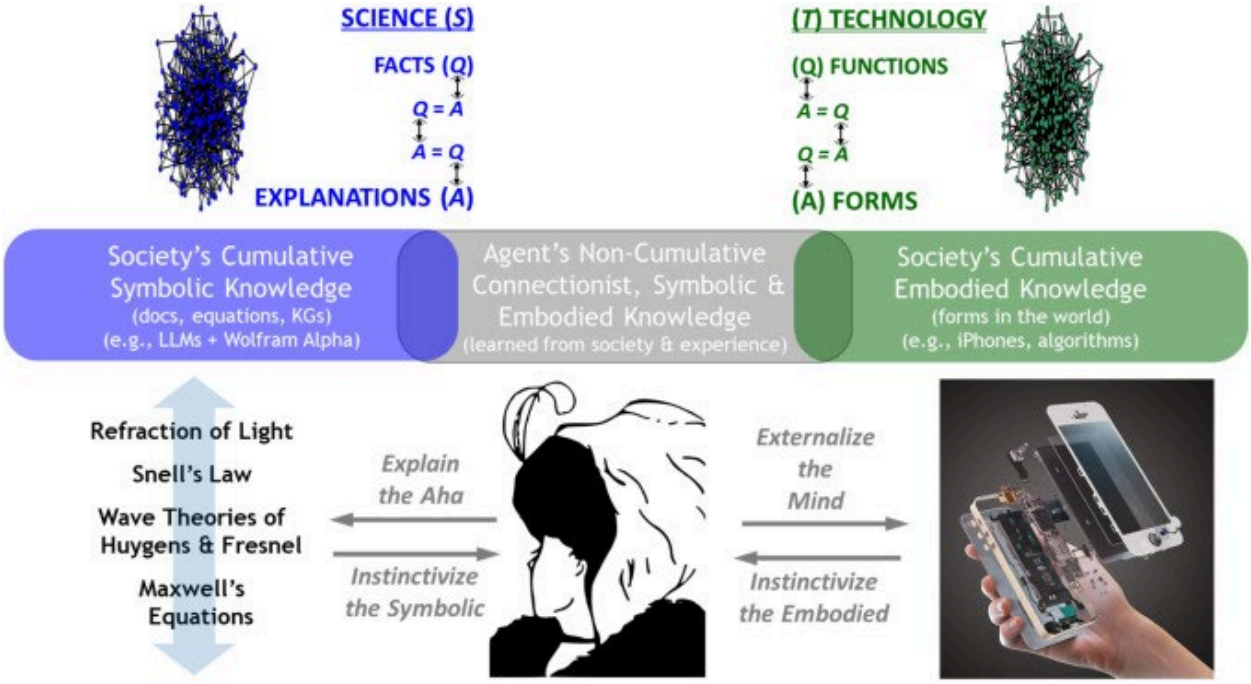

Figure 22. An AI agent, here shown in the bottom center, can complement human agent's ability to unearth scientific facts and replicate engineering functions.

Reference: [22] Tsao, J. Y., Abbott, R. G., Crowder, D. C., Desai, S., Dingreville, R. P. M., Fowler, J. E., ... & Stracuzzi, D. J. (2024). AI for Technoscientific Discovery: A Human-Inspired Architecture. *Journal of Creativity*, *34*(2), 100077.

DOI: https://doi.org/10.1016/j.yjoc.2024.100077

1.23. Bayesian optimization for stable properties amid processing fluctuations in sputter deposition

We introduce a Bayesian optimization approach to guide the sputter deposition of molybdenum thin films, aiming to achieve desired residual stress and sheet resistance while minimizing susceptibility to stochastic fluctuations during deposition. Thin films are pivotal in numerous technologies, including semiconductors and optical devices, where their properties are critical. Sputter deposition parameters, such as deposition power, vacuum chamber pressure, and working distance, influence physical properties like residual stress and resistance. Excessive stress and high resistance can impair device performance, necessitating the selection of optimal process parameters. Furthermore, these parameters should ensure the consistency and reliability of thin film properties, assisting in the reproducibility of the devices. However, exploring the multidimensional design space for process optimization is expensive. Bayesian optimization is ideal for optimizing inputs/parameters of general black-box functions without reliance on gradient information. We utilize Bayesian optimization to optimize deposition power and pressure using a custom-built objective function incorporating observed stress and resistance data. Additionally, we integrate prior knowledge of stress variation with pressure into the objective function to prioritize films least affected by stochastic variations. Our findings demonstrate that Bayesian optimization effectively explores the design space and identifies optimal parameter combinations meeting desired stress and resistance specifications.

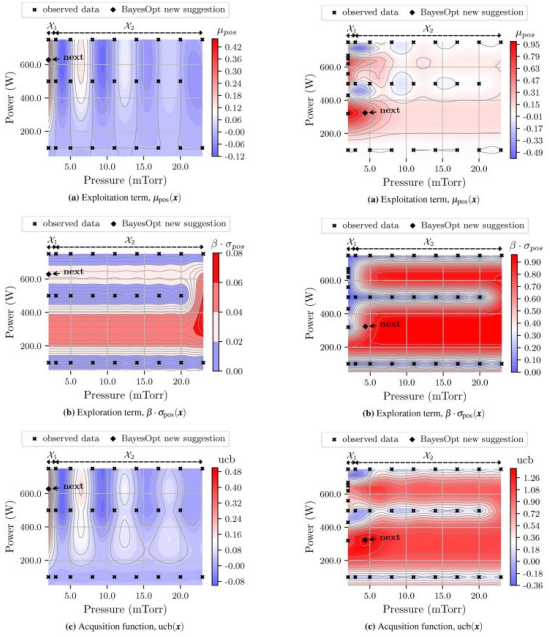

Figure 23. Bayesian-guided determination of the "next" most valuable data point to acquire, at (left) the first iteration of Bayesian selection, and (right) the seventh iteration of Bayesian selection. The exploitation term is captured by expected value based on a Gaussian process model in (a), and exploration term is captured by the uncertainty of the model's expected value expressed as a standard deviation multiplied by a scaling term (b). A weighted sum of these two terms results in the acquisition function shown in (c).

Reference: [23] Shrivastava, A., Kalaswad, M., Custer, J. O., Adams, D. P., & Najm, H. N. (2024). Bayesian optimization for stable properties amid processing fluctuations in sputter deposition. *Journal of Vacuum Science & Technology A*, *42*(3).

DOI: https://doi.org/10.1116/6.0003418

1.24. Unsupervised physics-informed disentanglement of multimodal data

We introduce physics-informed multimodal autoencoders (PIMA) - a variational inference framework for discovering shared information in multimodal datasets. Individual modalities are embedded into a shared latent space and fused through a product-of-experts formulation, enabling a Gaussian mixture prior to identify shared features. Sampling from clusters allows cross-modal generative modeling, with a mixture-of-experts decoder that imposes inductive biases from prior scientific knowledge and thereby imparts structured disentanglement of the latent space. This approach enables cross-modal inference and the discovery of features in high-dimensional heterogeneous datasets. Consequently, this approach provides a means to discover fingerprints in multimodal scientific datasets and to avoid traditional bottlenecks related to high-fidelity measurement and characterization of scientific datasets.

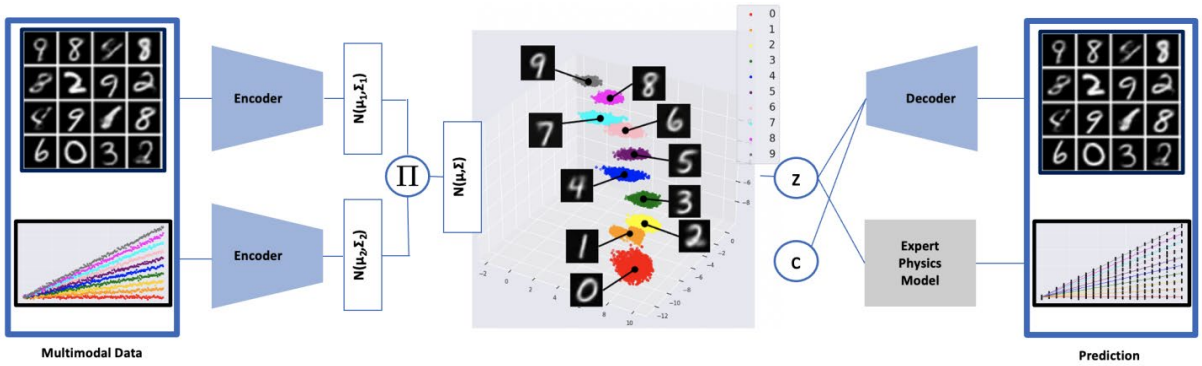

Figure 24. A physics-informed multimodal autoencoder fuses data from images of handwritten numbers 0-9 alongside toy empirical data with corresponding slopes 0-9. The expert physics model in the decoder allows embedding of an expected physical rule.

Reference: [24] Walker, E., Trask, N., Martinez, C., Lee, K., Actor, J. A., Saha, S., ... & Boyce, B. L. (2024). Unsupervised physics-informed disentanglement of multimodal data. *Foundations of Data Science*, 0-0.
DOI: https://doi.org/10.3934/fods.2024019

1.25. Rethinking materials simulations: Blending direct numerical simulations with neural operators.

Direct numerical simulations (DNS) are accurate but computationally expensive for predicting materials evolution across timescales, due to the complexity of the underlying evolution equations, the nature of multiscale spatio-temporal interactions, and the need to reach long-time integration. We develop a new method that blends numerical solvers with neural operators to accelerate such simulations. This methodology is based on the integration of a community numerical solver with a U-Net neural operator, enhanced by a temporal-conditioning mechanism that enables accurate extrapolation and efficient time-to-solution predictions of the dynamics. We demonstrate the effectiveness of this framework on simulations of microstructure evolution during physical vapor deposition modeled via the phase-field method. Such simulations exhibit high spatial gradients due to the co-evolution of different material phases with simultaneous slow and fast materials dynamics. We establish accurate extrapolation of the coupled solver with up to 16.5 speed-up compared to DNS. This methodology is generalizable to a broad range of evolutionary models, from solid mechanics, to fluid dynamics, geophysics, climate, and more.

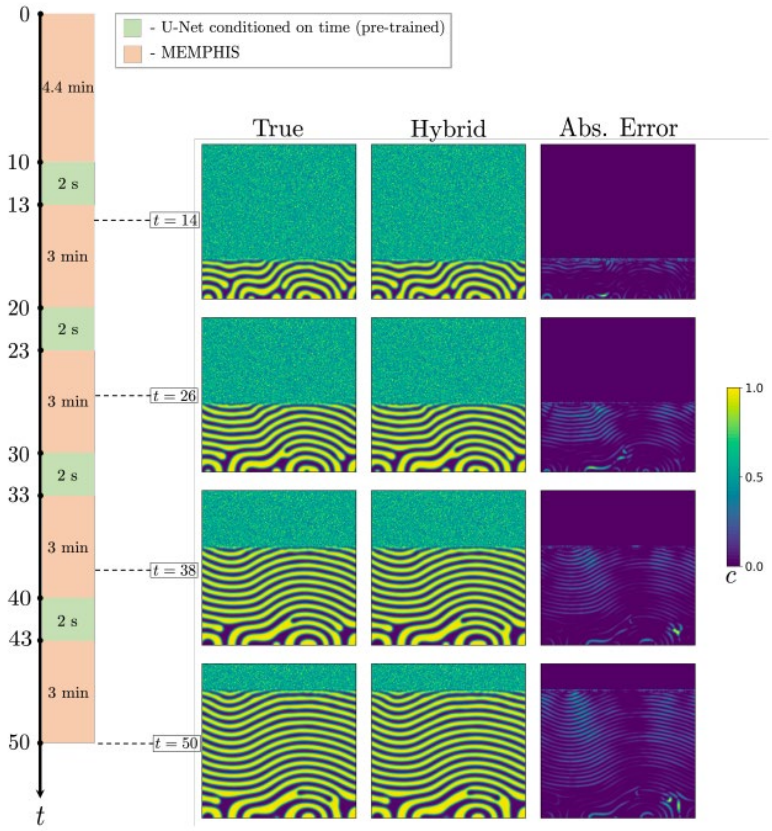

Figure 25. Direct numerical simulation using a phase field model (True) compared to an accelerated hybrid simulation approach that integrates a faster U-Net solver with periodic, slower phase field solutions.

Reference: [25] Oommen, V., Shukla, K., Desai, S., Dingreville, R., & Karniadakis, G. E. (2024). Rethinking materials simulations: Blending direct numerical simulations with neural operators. *npj Computational Materials*, *10*(1), 145.

DOI: https://doi.org/10.1038/s41524-024-01319-1

1.26. Unlocking alternative solutions for critical materials via materials informatics

Critical materials are materials that are essential for a broad range of modern technologies but subject to supply risks, and for which there are no easy substitutes. The list of materials that are considered critical depends on who, where, and when you ask. This ambiguity is due to several factors, including geopolitical instability, resource depletion, and environmental concerns. In the US, lithium (Li) has become the poster child for criticality, owing to the rapid rise in electric vehicles and the vanishingly small domestic production. Other examples include beryllium (Be), an important material for solar photovoltaics and electric-vehicle batteries, or neodymium (Nd) and dysprosium (Dy), because of their use in magnets. A 2023 assessment by the US Department of Energy identified "the electric eighteen" critical materials, which even include materials that are viewed as common, such as copper (Cu) and silicon (Si). While their supply risk is modest, their ubiquity in the energy sector renders any disruption potentially devastating.

The quest for the discovery and manufacturing of new and innovative materials to replace critical materials remains as vital as ever. Future critical materials disruptions will likely need to be solved in a matter of years or even months, rather than the decade or more often quoted as the requisite timeframe to mature from materials discovery to commercialization. In addition to this need for agility, a broadly coordinated federal strategy across all industrial sectors must address economic viability, ease of production, domestic availability, and lifecycle environmental impact. Resistance to change within the materials industry, along with a lack of awareness about environmental impacts, can slow down this transition. Regulatory frameworks may not be conducive to promoting sustainability, and technical challenges in fabricating materials with comparable performance to their traditional counterparts can be daunting. Additionally, limited data availability, existing infrastructure geared towards conventional materials, and market uncertainties can all pose substantial roadblocks. Therefore, to meet economic, industrial, and technological needs, it is imperative to accelerate the discovery of alternatives to critical materials by developing new and disruptive methods to identify materials with the desired properties in a timely and responsive manner.

Researchers and engineers have traditionally used their expertise and intuition, in concert with ab initio and heuristic models, to guide the discovery of new materials. However, machine learning (ML) and artificial intelligence (AI) systems are now surpassing human intuition limits for complex tasks such as image recognition, materials design and discovery, or autonomous experiments. These data-driven approaches can also compensate for predictive shortcomings in traditional models arising from assumptions, simplifications, and imperfect calibrations. As artificial intelligence algorithms become more powerful and accessible, many materials scientists are increasingly embracing this emerging scientific domain to accelerate the discovery and development of new materials. Materials informatics—the amalgam of materials science, AI and ML, and advanced data analytics—holds one of the keys to addressing roadblocks to discovering alternative solutions to critical materials. The promise of materials informatics is that the discovery and manufacturing of materials solutions that will replace critical materials can be simultaneously and rapidly optimized by semi-autonomous systems, where the engineers do not have to envision all possible materials replacement solutions and then painstakingly (and expensively) test each solution with build-and-check methods. Instead, engineers can select appropriate algorithms, embed known physical laws and constraints, and assign design and materials objectives. Materials informatic approaches have already proven quite useful for certain materials problems such as broad and rapid searches across the periodic table (or more often,

a rational subset) to achieve particular alloying effects, albeit such approaches may not be as obviously applicable for difficult-to-predict behaviors such as fatigue life, for instance.

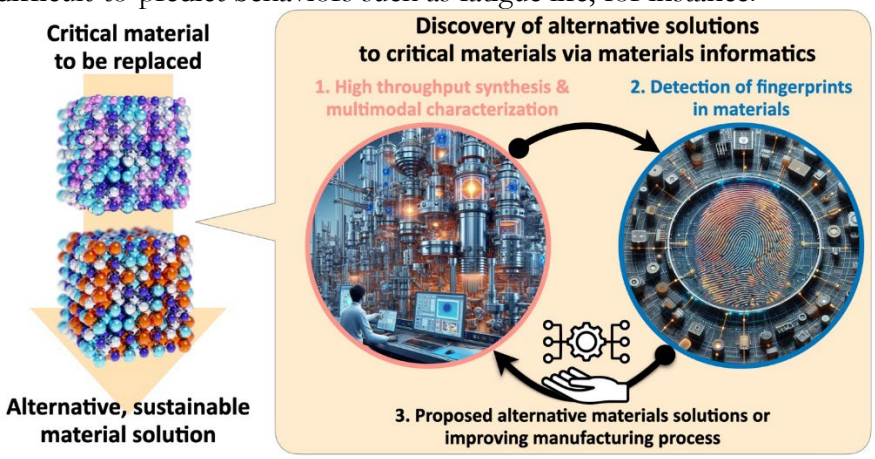

Figure 26. Notionally, AI algorithms offer the ability to detect complex or hidden "fingerprints" in large datasets obtained via high-throughput simulation and multimodal characterization, guiding the identification of alternative material solutions to replace at-risk materials.

Reference: [26] Dingreville, R., Trask, N.A., Boyce, B.L. Karniadakis, G.E. (2024). Unlocking alternative solutions to critical materials via materials informatics. *The Bridge*. Issue on Critical Materials, 54(2).

1.27. Bayesian blacksmithing: discovering thermomechanical properties and deformation mechanisms in high-entropy refractory alloys

Finding alloys with specific design properties is challenging due to the large number of possible compositions and the complex interactions between elements. This study introduces a multi-objective Bayesian optimization approach guiding molecular dynamics simulations for discovering high-performance refractory alloys with both targeted intrinsic static thermomechanical properties and also deformation mechanisms occurring during dynamic loading. The objective functions are aiming for excellent thermomechanical stability via a high bulk modulus, a low thermal expansion, a high heat capacity, and for a resilient deformation mechanism maximizing the retention of the BCC phase after shock loading. Contrasting two optimization procedures, we show that the Pareto-optimal solutions are confined to a small performance space when the property objectives display a cooperative relationship. Conversely, the Pareto front is much broader in the performance space when these properties have antagonistic relationships. Density functional theory simulations validate these findings and unveil underlying atomic-bond changes driving property improvements.

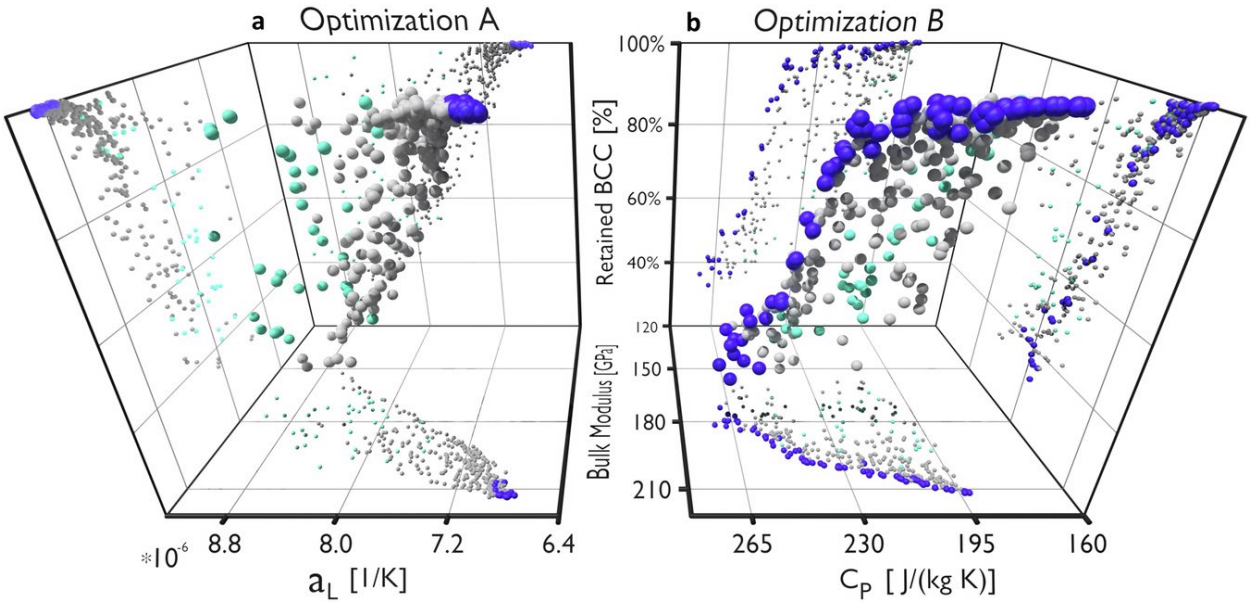

Figure 27. The multi-objective function consists of optimizing both (static) thermomechanical properties (bulk modulus, coefficient of thermal expansion, heat capacity) and target a specific deformation mechanism (retained BCC phase upon shock) in a model alloy: MoNbTaTi. Three-dimensional projections of the calculated property performance spaces of optimizations A (panel a) and B (panel b). Pareto optimal points are colored purple, while points from the initial database are colored turquoise. Points evaluated during optimization but which do not lie on either Pareto front are colored grey. To aid in visualization, two-dimensional projections are drawn onto the visible faces, and shadows are projected onto the points within the three-dimensional volume.

Reference: [27] Startt, J., McCarthy, M. J., Wood, M. A., Donegan, S., & Dingreville, R. (2024). Bayesian blacksmithing: discovering thermomechanical properties and deformation mechanisms in high-entropy refractory alloys. *npj Computational Materials*, *10*(1), 164.
DOI: https://doi.org/10.1038/s41524-024-01353-z

1.28. Tunable amorphous carbon films formed on ultralow wear, Pt-Au alloys

The mechanocatalytic formation of carbonaceous films at the interface between sliding metallic contacts is simultaneously advantageous for reducing friction and adhesion in several tribological applications and detrimental for electrical contacts as they can induce device failure by increasing the contact resistance. Yet, remarkably little is still known about the chemistry, structural and mechanical properties, and tunability of these interfacial layers. In this study, we performed contact pressure-dependent tribological experiments in dry nitrogen containing trace organics on four, nanocrystalline Pt-Au alloys ([Au] from 0 at.% to 10 at.%), a promising class of alloys for ultralow wear and electrical contact applications. The ex-situ, multi-technique characterization results did not only provide insights into the chemical nature and mechanical behavior of the mechanocatalytic, carbon-rich films formed on Pt-Au surfaces, but also revealed the interplay between catalytic and mechanochemical tribofilm formation controlled by the composition-dependent electronic structure of the Pt-Au substrate and the applied contact pressure. The results of this work provide guidelines for tailoring nanocrystalline alloys to control their mechano-catalytic activity on the basis of variations of the alloy mechanical properties and element's electronic structure with the alloy stoichiometry.

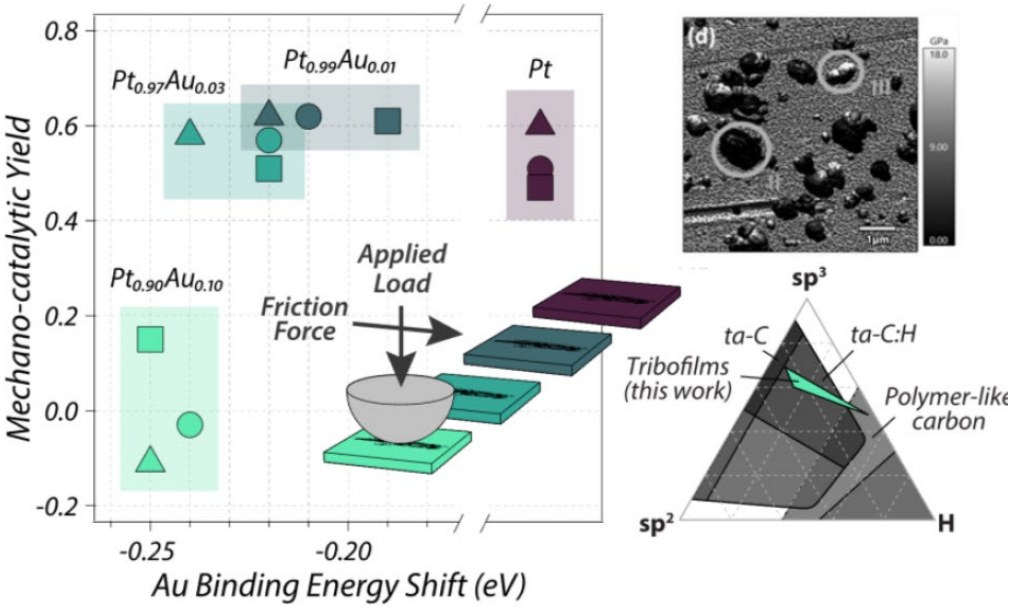

Figure 28. (left) Tribologically-induced mechano-catalytic yield (omitting non-contact region) as a function of the Au $4f_{7/2}$ binding energy shift. (upper right) AM-FM nanomechanical mapping reveal that tribochemically-induced particles are mechanically distinct from the substrate. (lower right). A ternary phase diagram based on spectroscopic analysis showing tetrahedral amorphous C:H tribofilms (ta-C:H, green region) that formed during sliding contact in Pt-Au.

Reference: [28] Edwards, C. E., Babuska, T. F., Curry, J. F., DelRio, F. W., Killgore, J. P., Boyce, B. L., ... & Mangolini, F. (2024). Tunable amorphous carbon films formed on ultralow wear, Pt–Au alloys. *Carbon*, *226*, 119220.
DOI: https://doi.org/10.1016/j.carbon.2024.119220

1.29. High-Throughput Microstructural Characterization and Process Correlation using Automated Electron Backscatter Diffraction

The need to optimize the processing conditions of additively manufactured (AM) metals and alloys has driven advances in throughput capabilities for material property measurements such as tensile strength or hardness. High-throughput (HT) characterization of AM metal microstructure has fallen significantly behind the pace of property measurements due to intrinsic bottlenecks associated with the artisan and labor-intensive preparation methods required to produce highly polished surfaces. This inequality in data throughput has led to a reliance on heuristics to connect process to structure or structure to properties for AM structural materials. In this study, we show a transformative approach to achieve laser powder bed fusion (LPBF) printing, HT preparation using dry electropolishing and HT electron backscatter diffraction (EBSD). This approach was used to construct a library of > 600 experimental EBSD sample sets spanning a diverse range of LPBF process conditions for AM Kovar. This vast library is far more expansive in parameter space than most state-of-the-art studies, yet it required only approximately 10 labor hours to acquire. Build geometries, surface preparation methods, and microscopy details, as well as the entire library of >600 EBSD data sets over the two sample design versions, have been shared with intent for the materials community to leverage the data and further advance the approach. Using this library, we investigated process–structure relationships and uncovered an unexpected, strong dependence of microstructure on location within the build, when varied, using otherwise identical laser parameters.

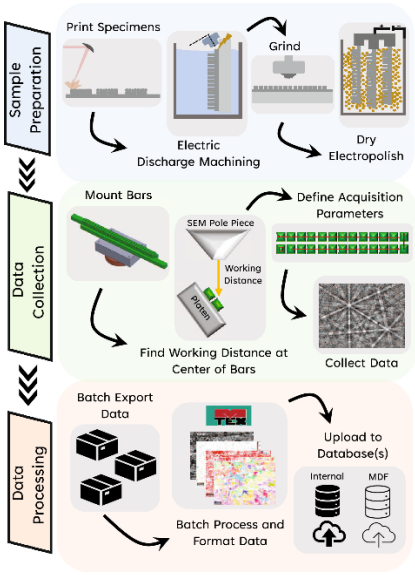

Figure 29. A streamlined high-throughput workflow enabled the collection of electron backscatter diffraction maps from hundreds of uniquely processed additively manufactured metals.

Reference: [29] Fowler, J. E., Ruggles, T. J., Cillessen, D. E., Johnson, K. L., Jauregui, L. J., Craig, R. L., ... & Boyce, B. L. (2024). High-Throughput Microstructural Characterization and Process Correlation Using Automated Electron Backscatter Diffraction. *Integrating Materials and Manufacturing Innovation*, 1-15.
DOI: https://doi.org/10.1007/s40192-024-00366-2

1.30. Dataset of simulated vibrational density of states and x-ray diffraction profiles of mechanically deformed and disordered atomic structures in gold, iron, magnesium, and silicon

This dataset is comprised of a library of atomistic structure files and corresponding X-ray diffraction (XRD) profiles and vibrational density of states (VDoS) profiles for bulk single crystal silicon (Si), gold (Au), magnesium (Mg), and iron (Fe) with and without disorder introduced into the atomic structure and with and without mechanical loading. Included with the atomistic structure files are descriptor files that measure the stress state, phase fractions, and dislocation content of the microstructures. All data was generated via molecular dynamics or molecular statics simulations using the Large-scale Atomic/Molecular Massively Parallel Simulator (LAMMPS) code. This dataset can inform the understanding of how local or global changes to a materials microstructure can alter their spectroscopic and diffraction behavior across a variety of initial structure types (cubic diamond, face-centered cubic (FCC), hexagonal close-packed (HCP), and body-centered cubic (BCC) for Si, Au, Mg, and Fe, respectively) and overlapping changes to the microstructure (i.e., both disorder insertion and mechanical loading).

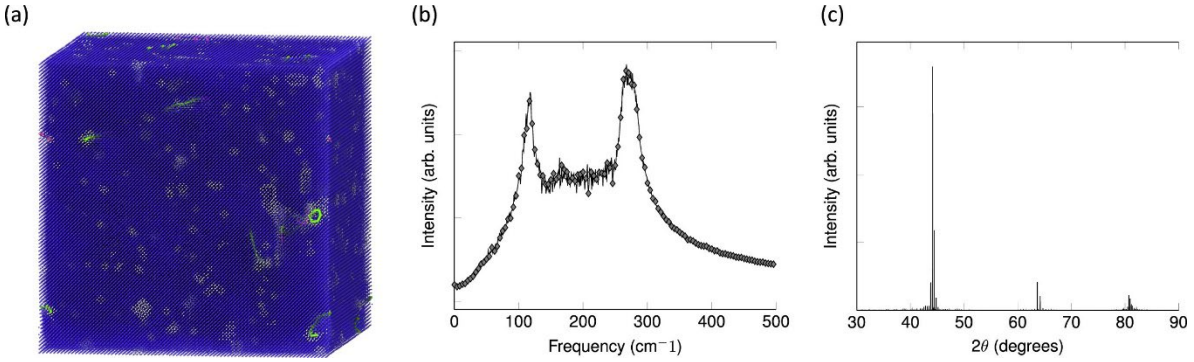

Figure 30. (a) Render of a bulk Fe microstructure at 0.15 dpa and 0.05 hydrostatic tensile strain. Atoms are coloured according to their phase: blue is BCC, white is disordered. Dislocation lines are coloured according to their type: green are ½ ⟨111⟩ and magenta are ⟨100⟩. Corresponding (b) VDoS profile, truncated at 500 cm^{-1} and (c) XRD profile for the microstructure rendered in (a).

Reference: [30] Vizoso, D., & Dingreville, R. (2024). Dataset of simulated vibrational density of states and X-ray diffraction profiles of mechanically deformed and disordered atomic structures in Gold, Iron, Magnesium, and Silicon. *Data in Brief*, *55*, 110689.
DOI: https://doi.org/10.1016/j.dib.2024.110689

1.31. Benchmarking machine learning strategies for phase-field problems

We present a comprehensive benchmarking framework for evaluating machine-learning approaches applied to phase-field problems. This framework focuses on four key analysis areas crucial for assessing the performance of such approaches in a systematic and structured way. Firstly, interpolation tasks are examined to identify trends in prediction accuracy and accumulation of error over simulation time. Secondly, extrapolation tasks are also evaluated according to the same metrics. Thirdly, the relationship between model performance and data requirements is investigated to understand the impact on predictions and robustness of these approaches. Finally, systematic errors are analyzed to identify specific events or inadvertent rare events triggering high errors. Quantitative metrics evaluating the local and global description of the microstructure evolution, along with other scalar metrics representative of phase-field problems, are used across these four analysis areas. This benchmarking framework provides a path to evaluate the effectiveness and limitations of machine-learning strategies applied to phase-field problems, ultimately facilitating their practical application.

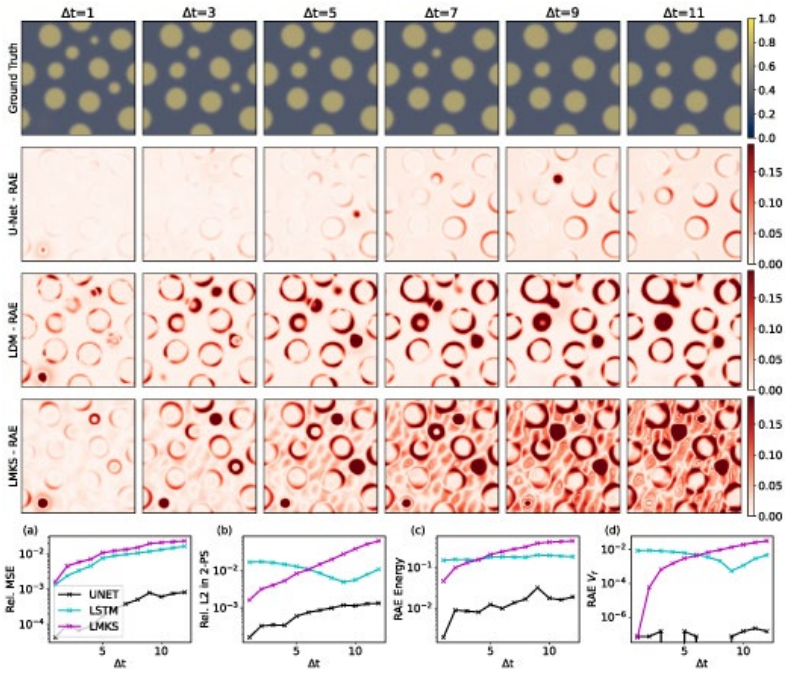

Figure 31. Visual comparison of the simulation trajectories between the direct numerical solver (top row, ground truth), and predictions from the validation set from our three machine-learning solvers: the U-Net (second row), the LDM (third row), and LMKS (fourth row). Results for the three machine-learning solvers are displayed in terms of the relative absolute error (RAE) with respect to the ground truth predictions. Additionally, panels (a)–(d) provide quantitative comparisons between the three machine-learning solvers and the direct numerical simulations as a function of simulation time in terms of the relative mean-squared error (Rel. MSE) of the concentration field, the Rel. L2 metric for the 2-point statistics (Rel. L_2 in 2-PS), the RAE for the energy (RAE Energy), and the RAE for the phase volume fraction (RAE V_f).

Reference: [31] Dingreville, R., Roberston, A. E., Attari, V., Greenwood, M., Ofori-Opoku, N., Ramesh, M., & Zhang, Q. (2024). Benchmarking machine learning strategies for phase-field problems. *Modelling and Simulation in Materials Science and Engineering*, *32*(6), 065019.
DOI: 10.1088/1361-651X/ad5f4a

1.32. Guided combinatorial synthesis and automated characterization expedites the discovery of hard, electrically conductive PtxAu1-x films

Sputter-deposited Pt-Au thin films have been reported to develop a hard, thermally stable,nanocrystalline structure, yet little is known about how these characteristics vary with PtxAu1-xcomposition and process conditions. Toward this end, this document describes an extensive, combinatorial Pt-Au thin film library including characterized film compositions, structure and properties. Complemented by kinematic Monte Carlo simulations of co-deposition, a broadrange of PtxAu1-x compositions (from x ~ 0.02 to 0.93) was first established by sputtering withvaried magnetron powers and gun tilt angles. The produced films were subsequently interrogated using automated nano-indentation, X-ray reflectivity, X-ray diffraction, Atomic Force Microscopy, surface profilometry, four-point probe sheet resistance techniques, and Wavelength Dispersive Spectroscopy in order to determine how hardness, modulus, density, surface roughness, structure and resistivity vary with film stoichiometry and process parameters. Combinatorial films displayed an assortment of properties with the hardness of some films exceeding values reported previously for this material system. High hardness, high modulus, and low resistivity were generally attained when using increased deposition energy and reduced angle-of-incidence processes. Overall, the research identified promising, new PtxAu1-x compositions for future study and pinpointed strategies for improved deposition.

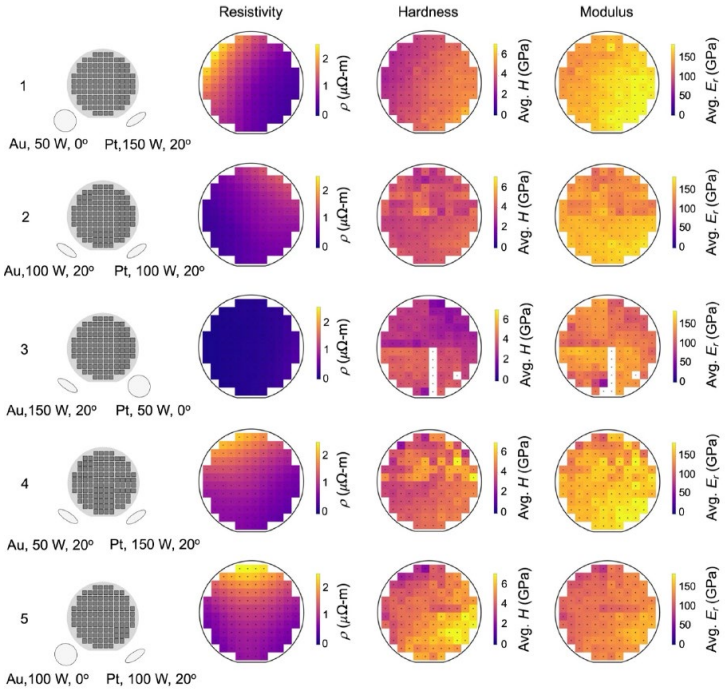

Figure 32. Wafer maps of key properties measured across 5 combinatorial wafers each consisting of 112 unique deposition conditions (cm square patches).

Reference: [32] Adams, D.P., Kothari, R., Addamane, S., Jain, M., Dorman, K., Desai, S., Sobczak, C., Kalaswad, M., Bianco, N., DelRio, F.W., Custer, J.O., Rodriguez, M.A., Boro, J., Dingreville, R., Boyce, B.L. (2024). Guided combinatorial synthesis and automated characterization expedites the discovery of hard, electrically conductive PtxAu1-x films, *J. Vac. Sci. Techn. A.* Accepted for publication.
DOI: https://doi.org/10.1116/6.0003785

1.33. Toughness from Imagery: extracting more from failure analysis using deep convolutional neural networks

Understanding the origins of mechanical failures is critical to the prevention of future failures. In this study, additively manufactured Charpy bars, commonly used to measure the impact toughness of materials, were produced over a wide range of process conditions. The Charpy V-Notch toughness was measured on over 200 samples alongside corresponding optical images of both sides of the fracture surface. Convolutional neural network models were trained to correlate the fractographic images with quantitative toughness values. Several different neural network architectures were compared, along with other strategies for data cleaning and downsampling. The best models predicted Charpy toughness values from imagery with a mean absolute percent error of 8.5%. The neural network results were interpreted through a Gradient-weighted Class Activation Mapping (Grad-CAM) saliency map; toughness values were correlated with expected physical characteristics such as porosity, shear lips, fracture surface edges, etc. A model trained on data from a Kovar alloy was found to maintain predictivity when applied to other similar alloy systems (300-series stainless steels) without any additional training. The primary optical images used in this study were macrofractography images spanning the entire fracture surface; a follow-on study using microfractographic images was less predictive, but retained some utility. This work illustrates opportunities for developing data-driven approaches to provide quantitative assessment and qualitative interpretations of fracture surfaces.

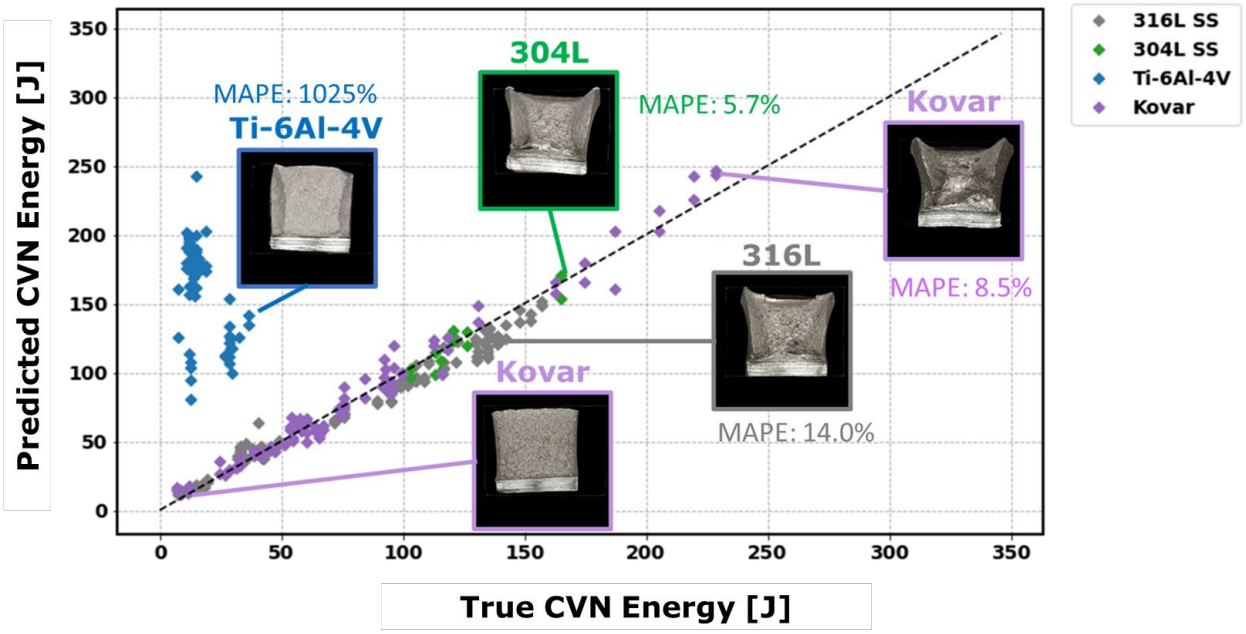

Figure 33. Parity plot of a neural network model for Charpy toughness (CVN) predicted based on inset imagery versus ground truth measurements. Training utilized holdout data from only the Kovar dataset. The model not only predicts Kovar toughness from fracture images (insets) but can also have similar predictive power for similar austenitic stainless steel alloys, 304L and 316L.

Reference: [33] Bianco, N., Fitzgerald, K., Cillessen, D., Brown, N., Carroll, J., Garland, A., Bassett, K.L., Schroder, J.B., Boyce, B.L. (2024). Toughness from Imagery: extracting more from failure analysis using deep convolutional neural networks, submitted to *Journal of Failure Analysis and Prevention*, Accepted for publication.

1.34. Sputter-deposited Mo thin films: characterization of grain structure and Monte Carlo simulations of sputtered atom energies and incidence angles

Multimodal datasets for materials provide the large amount of information needed for expediting the discovery of process-structure-property relationships important to materials performance. In this Data Descriptor article, we describe a dataset for magnetron sputtered molybdenum thin films. The dataset is taken from 27 unique depositions that vary sputter power and argon sputter pressure. High angle annular dark field and bright field cross-section transmission electron micrographs were obtained from films produced in each of the depositions. Automated crystal orientation mapping was used to derive inverse pole figures from the imaged areas covering hundreds of grains, and MTEX, a Matlab toolbox for analyzing crystallographic textures, extracted statistics of the grain sizes and tilt. Additionally, the binary-collision Monte Carlo computer program SiMTra was used to simulate aspects of film deposition. SiMTra monitors the gas-phase transport effects on the energy and angular distributions of the arriving metal species as a function of the process parameters. The SiMTra simulations accounted for sample rotation in a true planetary configuration wherein substrates passed repeatedly under a 200 mm-diameter cathode in a sputter-down, co-planar geometry. For the predicted angle of incidence and energy, probability density functions, uniformity maps, and average quantities are reported for different sputter powers, Ar pressures, and working distances. Overall, the described data set provides opportunities for examining process-structure relationships. The entirety of this data is committed to a public repository in the Materials Data Facility.

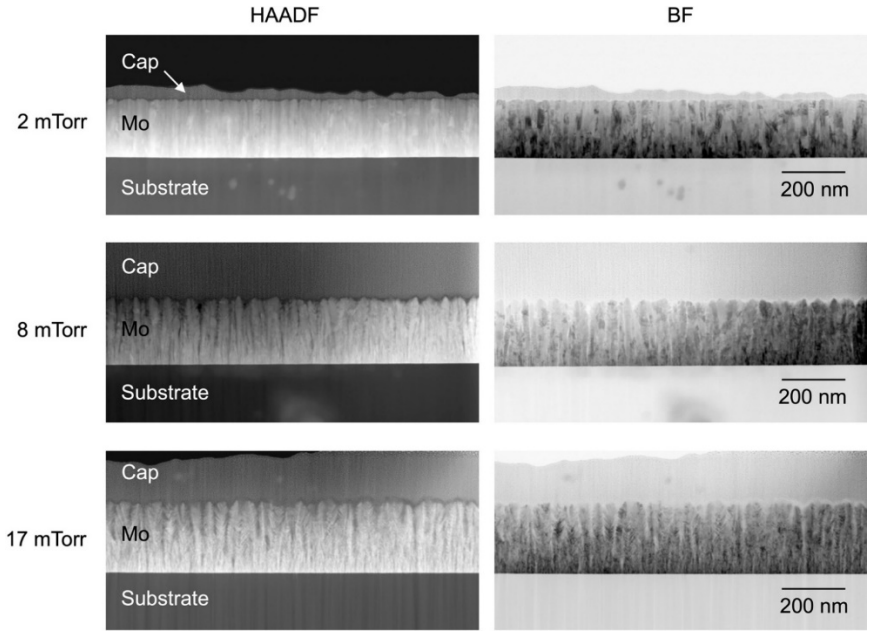

Figure 34. Paired High Angle Annular Darkfield and Brightfield transmission electron micrographs obtained from three different Mo films sputter deposited using a power of 100 W. Films are shown in cross-section, and the argon pressure used for the deposition is listed to the left of the HAADF images. Increased surface roughness and branching are evident at higher process pressures.

Reference: [34] Custer, J.O., Kalaswad, K., Kothari, R.S., Kotula, P.G., Ruggles, T., Dingreville, R., Henriksen, A., Adams, D.P. (2024). Sputter-deposited Mo thin films: characterization of grain structure and Monte Carlo simulations of sputtered atom energies and incidence angles. To be submitted to *Integrating Materials and Manufacturing Innovations*.

1.35. Cu-Ag Nanocrystalline Thin Films: Materials Library for the Study of Process-Property-Microstructure Relationships

A compositional and deposition-parameter space investigation of nanocrystalline Cu-Ag thin films was performed to construct a materials library for both traditional and machine learning analysis. Facilitated by combinatorial methods, 672 co-sputtered films of Cu-Ag have been deposited via pulsed DC magnetron methods utilizing single element targets. Varying the gun-tilt angle, power at each cathode, and Ar pressure enabled swift examination of nearly the full range of alloy compositions and a relevant portion of deposition atomistics. Wavelength dispersive spectroscopy, atomic force microscopy, x-ray diffraction, x-ray reflectivity, sheet resistance, optical profilometry and nanoindentation were employed for automated mapping analysis of the resulting films. The resultant hardness, modulus, film density, crystal texture and resistivity of films having different composition were analyzed in terms of key characteristics of deposition (incident atom kinetic energy and incidence angle) predicted by the binary-collision, kinematic Monte Carlo program SiMTra. The survey revealed compositional and energetic dependencies of film tarnishing, gains in mechanical performance against literature values, and resistivity dependence on composition described by Nordheim's rule. Much of the results are discussed in the context of microstructural variations and differences in film density. Additionally, TEM demonstrates several forms of compositional variation including Ag segregation to Cu grain boundaries as well as 5-nm period, intragranular compositional modulations. Annealing of a Cu-rich alloy reveals that despite room-temperature grain boundary segregation of the Ag solute in such composition of Cu-Ag, this as-deposited structure is not thermally stable above 100 ˚C.

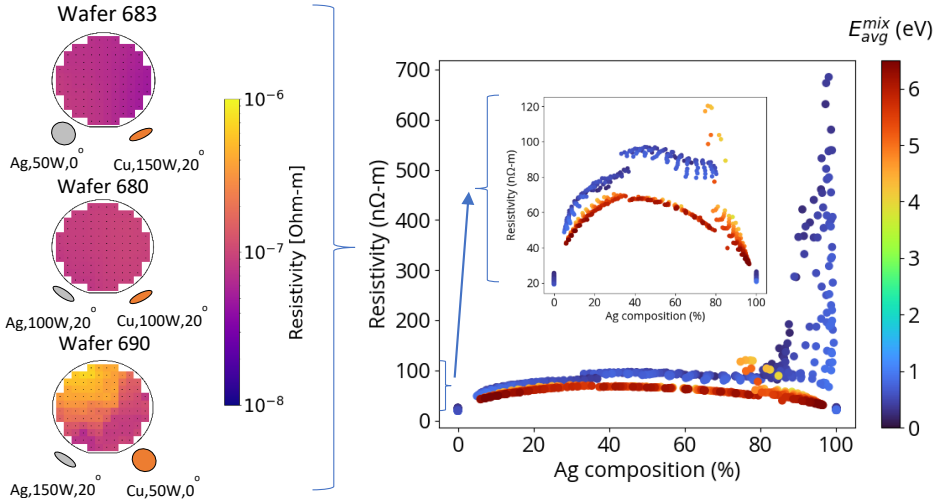

Figure 35. Visualization of a subset of depositions, measurements, and correlative analyses performed, focused on the relationship between resistivity and sputtered atom energy retained on arrival at the substrate. The full set includes 8 wafers (6 co-sputtered, 2 single element) with differing deposition conditions, 896 resulting films, and 7 main modalities of measurement supplemented by TEM.

Reference: [35] Dorman, K. R., Bianco, N., Kothari, R., Kalaswad, M., Sobczak, C., Desai, S., Custer, J., Addamane, S., Jain, M., Hinojos, A., Rodriguez, M., DelRio, F., Boyce, B. L., Dingreville, R., & Adams, D. P. (2024). Cu-Ag Nanocrystalline Thin Films: Materials Library Development for the Study of Process-Property-Microstructure Relationships. To be submitted to *Thin Solid Films*.

1.36. Unsupervised Multimodal Fusion of In-process Sensor Data for Advanced Manufacturing Process Monitoring

Effective monitoring of manufacturing processes is crucial for maintaining product quality and operational efficiency. Modern manufacturing environments often generate vast amounts of multimodal data, including visual imagery from various perspectives and resolutions, hyperspectral data, and machine health monitoring information such as actuator positions, accelerometer readings, and temperature measurements. However, interpreting this complex, high-dimensional data presents significant challenges, particularly when labeled datasets are unavailable or impractical to obtain. This paper presents a novel approach to multimodal sensor data fusion in manufacturing processes, inspired by the Contrastive Language-Image Pre-training (CLIP) model. We leverage contrastive learning techniques to correlate different data modalities without the need for labeled data, overcoming limitations of traditional supervised machine learning methods in manufacturing contexts. Our proposed method demonstrates the ability to handle and learn encoders for five distinct modalities: visual imagery, audio signals, laser position (x and y coordinates), and laser power measurements. By compressing these high-dimensional datasets into low-dimensional representational spaces, our approach facilitates downstream tasks such as process control, anomaly detection, and quality assurance. The unsupervised nature of our method makes it broadly applicable across various manufacturing domains, where large volumes of unlabeled sensor data are common. We evaluate the effectiveness of our approach through a series of experiments, demonstrating its potential to enhance process monitoring capabilities in advanced manufacturing systems. This research contributes to the field of smart manufacturing by providing a flexible, scalable framework for multimodal data fusion that can adapt to diverse manufacturing environments and sensor configurations. The proposed method paves the way for more robust, data-driven decision-making in complex manufacturing processes.

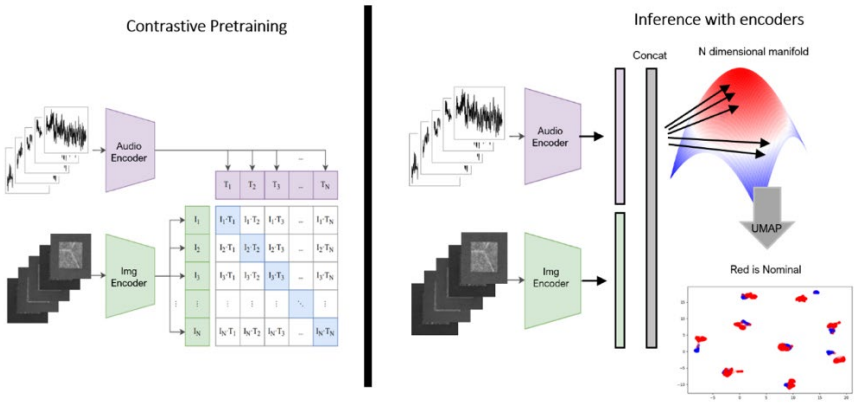

Figure 36. (left) We use contrastive loss to train encoders for each modality. Contrastive loss pushes corresponding vectors closer together in latent space. (right) We use the encoders for inference over the data to identify clusters and anomalies. The red and blue dots on the 2D scatter plot are data tuples from a nominal print (in red) and a purposefully off-nominal print (blue). Each dot represents an individual part for a unique layer, and each group of red and blue circles represents a distinct part on the build plates. The red and blue dots are not directly on top of each other which shows we are able to discriminate between the nominal and off-nominal builds.

Reference: [36] M. McKinney, A. Garland, D. Cillessen, J. Adamczyk, D. Bolintineanu, M. Heiden, E. Fowler, B.L. Boyce, (2024). Unsupervised multimodal fusion of in-process sensor data for advanced manufacturing process monitoring. To be submitted to *Journal of Manufacturing Systems.*

1.37. Understanding Pt_xAu_{1-x} films through unsupervised disentanglement of multimodal data

Recent literature has explored a broad range of Pt_xAu_{1-x} compositions and has shown under certain conditions these films display hardness values exceeding that of their constituents (Pt, Au). Although studies have correlated film hardness with various conditions, challenges with making sense of the complex combinatorial space have ultimately left explainability as inconclusive. In effort to further our understanding of these high-hardness Pt_xAu_{1-x} films, an unsupervised clustering algorithm based on variational inference is implemented which encodes disparate modalities (scalars, spectra, ..) into a shared latent representation. Through clustering of this latent representation, the algorithm identifies distinct mechanistic regimes with correlations across modalities. The underpinnings of this approach enables training on data with missing information (e.g., corrupted measurements) and enables cross-modal estimation. This approach is demonstrated with a Pt_xAu_{1-x} dataset, which showcases its capability as a tool for improving explainability of complex multimodal datasets. With this algorithm we explore the complex combinatorial space and offer new insights into our understanding of the high-hardness Pt_xAu_{1-x} films.

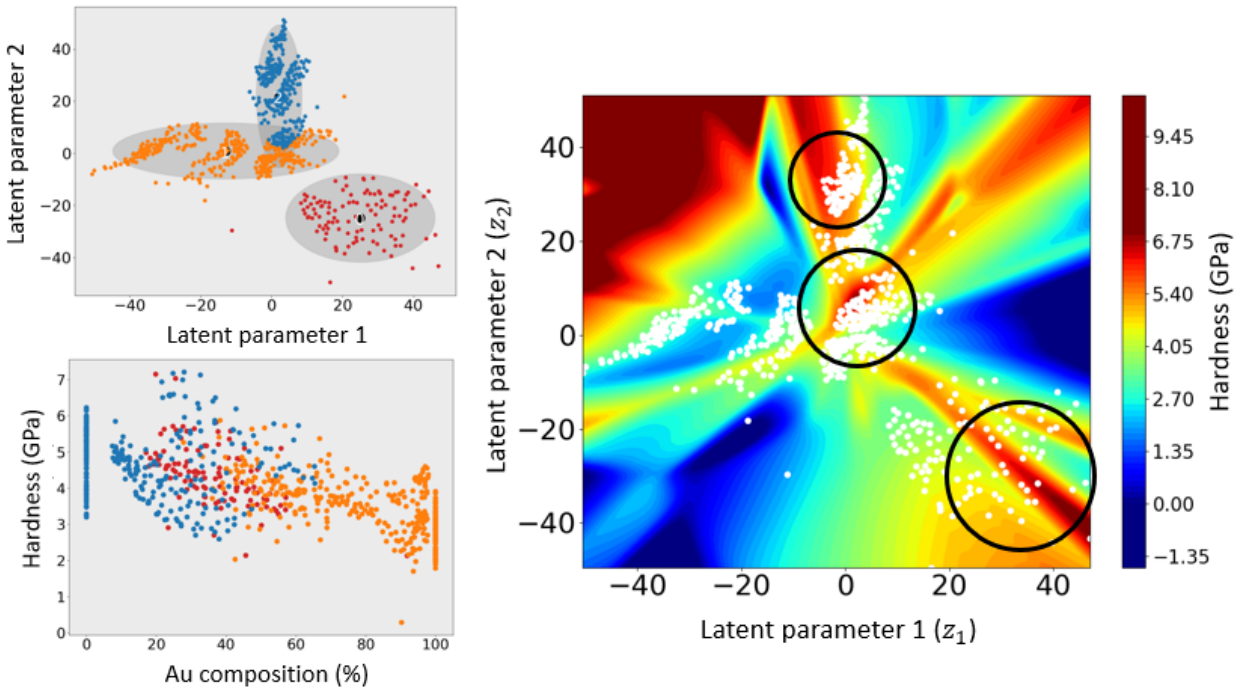

Figure 37 (Top left) the trained model's two-dimensional latent space identifying three clusters with (bottom left) each cluster representing a unique range of compositions with different hardness values. (Right) the latent space sampled and colored by the trained model's generated hardness, unveiling three regions of high hardness. The middle circle is dense with datapoints and converges to a local maximum, which suggests robustness in the process conditions for producing these high-hardness films. This is in opposition to the bottom right circle where there is sparsity in the data and suggestions wiggle room in the process conditions to produce even higher hardness films in subsequent experiments.

Reference: [37] Shilt, T., Adams, D. P., Martinez, C., Dingreville, R. (2024). "Understanding Pt_xAu_{1-x} films through unsupervised disentanglement of multimodal data". To be submitted to *npj Computational Materials.*

2. LIST OF PUBLISHED DATASETS

In addition to peer-reviewed manuscript, we also published four, publicly available datasets:

1. D.P. Adams, S. Addamane, J.O. Custer, F. DelRio, M. Kalaswad, L. Jauregui, R. Khan, A. Henriksen (2022). "Sputter deposited Mo thin films: multimodal characterization of residual stress, resistivity, crystallinity and surface morphology", *Materials Data Facility*. https://doi.org/10.18126/io99-ldj2

2. S. Desai, R. Dingreville, A. Shrivastava (2023) Microstructure evolution dataset from phase-field simulations (spinodal decomposition, physical vapor deposition, grain growth, dendrite growth), *Materials Data Facility*. https://doi.org/10.18126/ivdc-l57i

3. Fowler, J. Elliott; Ruggles, Tim J.; Cillessen, Dale E.; Johnson, Kyle L.; Jauregui, Luis J.; Henriksen, Amelia A.; Bianco, Nathan R.; Boyce, Brad L. (2023). High Throughput EBSD Characterization of Additive Kovar." *Materials Data Facility*. https://doi.org/10.18126/7d9u-edev

4. D. Visozo, R. Dingreville, (2023). Simulated vibrational density of states and x-ray diffraction profiles of mechanically deformed and disordered atomic structures in gold, iron, magnesium, and silicon, *Materials Data Facility*, https://doi.org/10.18126/tacz-v14v

5. R. Kothari, A. Henriksen, R. Dingreville, D.P. Adams, (2024). Analysis of SimTra Outputs for Sputter Deposition involving Planetary Substrate Travel. To be submitted to *Materials Data Facility*.

3. LIST OF REPORTS

1. H.H. Lim, J.F. Curry, M.T. Dugger, "Improved Throughput and Analysis of Scratch Test Results via Automation and Machine Learning", SAND2022-1836

2. N. Trask, "AI-enabled high-throughput science: multimodality and computational challenges" *AI@DOE Roadmapping Workshop* (2021).

3. M. D'Elia, A. Howard, R.M. Kirby, N. Kutz, A. Tartakovsky, H. Viswanathan, "Discovering new governing equations using ML", in: *Machine Learning in Heterogeneous Porous Materials*, a report for the National Academies, 2022. [note: unclear if this report is final or not]

4. Sanchez, D. "Breaking the Mold: Individual and Situational Moderators of Cognitive Flexibility in Material Deposition and Machine Learning Personnel." SAND2022-13767 O.

4. SUMMARY OF UNPUBLISHED WORK

4.1. Combining variational autoencoders with latent Bayesian optimization to find optimal physical vapor deposition parameters

4.1.1. Motivation

To identify a set of optimal deposition parameters, we propose a method that integrates the dimensionality reduction capabilities of a variational autoencoder (VAE) [38] with a Gaussian process (GP) surrogate model [39-41]. This approach is motivated by several factors. Firstly, the VAE enables dimensionality reduction, allowing us to apply the Gaussian process in a lower-dimensional parameter space. Secondly, the VAE helps to uncover a decorrelated latent space, simplifying the process of optimal design within that space. Additionally, the architecture allows for the integration of multimodal information through the inclusion of additional encoders [24]. However, this approach presents challenges, such as issues with extrapolation when selecting optimal design points and the potential for poorly structured latent spaces that hinder surrogate modeling. Previous studies that have combined VAEs with GP regression across various applications have explored strategies to overcome these challenges.

4.1.2. Method

In this section, we introduce the complete PVD-based optimal design algorithm for quickly identifying deposition parameters that yield the desired film characteristics. Figure 38 provides a schematic overview of our approach. It is important to note that the VAE/GP algorithm (center block of Figure 38) is versatile and can be applied to other contexts as well.

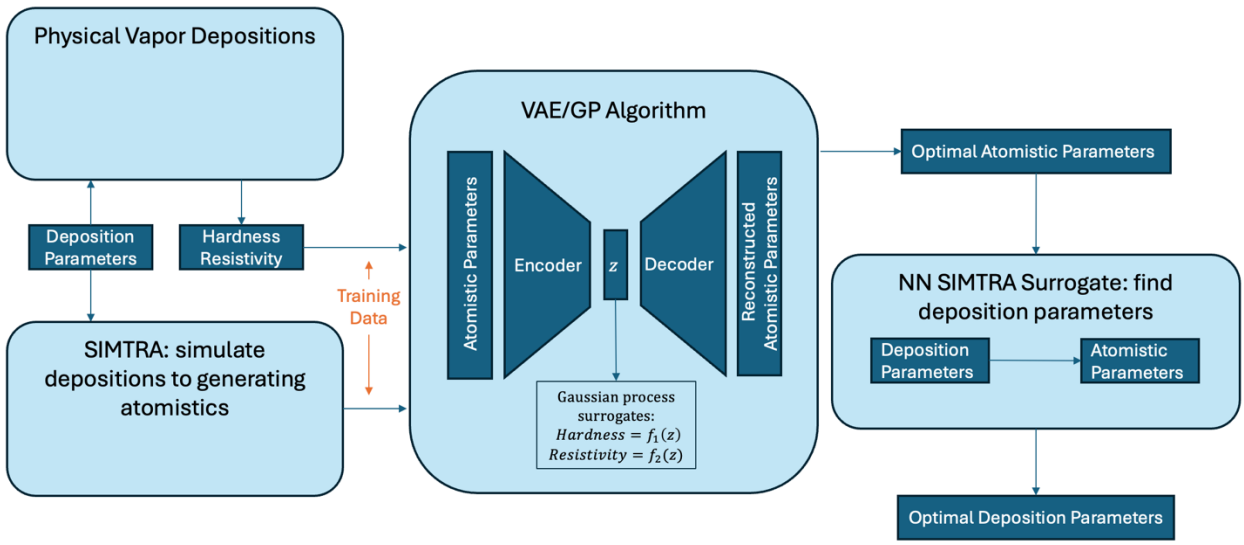

Figure 38. Schematic of the full algorithmic approach.

4.1.3. Results (PVD dataset for model training)

The VAE/GP model was trained using data from three combinatorial copper/silver wafer depositions. Each wafer contains 112 films, providing a total of 336 data points for model training, validation, and testing. To assess the model's performance, 235 points (approximately 70%) were

allocated for training (100 for the first training set and 135 for the second), 67 points (about 20%) were used for validation to select the best model, and 34 points (roughly 10%) were reserved for testing. The VAE/GP training was repeated ten times with different training, validation, and testing data sets to evaluate the robustness of the results. For the final atomistic parameter recommendations, 269 points were used for model training (100 for the first training set and 169 for the second), while 67 points were used for validation. We then tested the model using results from the recommended set of depositions. The process parameter input to the VAE/GP algorithm, is a vector comprising the 9 atomistic parameters obtained by simulating each of the three depositions in SIMTRA. Additionally, we included XRD data as a secondary modality. During model training, we initially trained the VAE/GP algorithm using only the process parameters. In a subsequent training phase, we incorporated the XRD data. Throughout this section, we will compare the results from these two phases of training, i.e., with and without the inclusion of the XRD data.

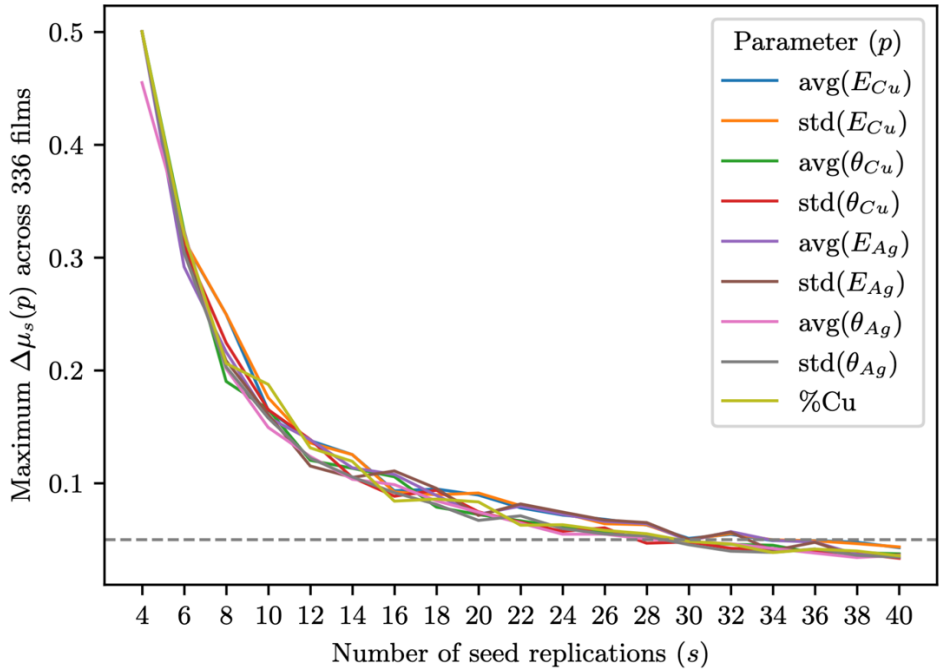

Figure 39. Approximately 40 replications of SIMTRA are required to get convergence of the atomistic parameter estimates. Showing the maximum value of Equation (31) across 336 films (112 films for each of the three wafers describe in Table 1). We see that with approximately 40 replications the maximum relative change in the mean prediction is less than 5%.

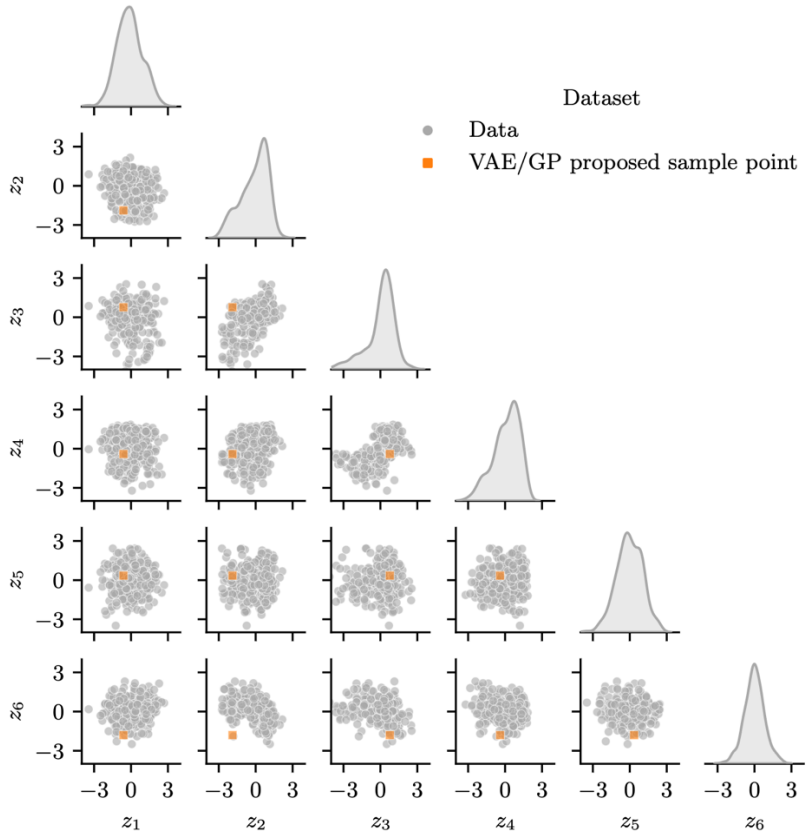

Figure 40. Proposed sample point in latent space (orange square) falls within the domain of the training and validation data (gray dots). Additionally, this visualization of the latent space shows that the six latent variables follow a roughly Gaussian distribution (see diagonal density estimations) and are uncorrelated (see scatter plots).

Table 1. Recommended atomistic parameter values from the three approaches.

Parameter	VAE/GP (without XRD)	VAE/GP (with XRD)	GP Only
$avg(E_{Cu})$	0.296	0.124	0.239
$std(E_{cu}$	2.216	1.566	4.468
$avg(\theta_{Cu})$	42.3	42.7	42.1
$std(\theta_{Cu})$	18.8	19.2	18.7
$avg(E_{Ag})$	0.724	0.113	0.506
$std(E_{Ag})$	3.679	0.743	4.110
$avg(\theta_{Ag})$	40.6	41.9	42.5
$std(\theta_{Ag})$	18.4	19.0	18.9
$\%Cu$	0.128	0.602	0.022

4.1.4. Discussion

Overall, these results underscore the robustness of the VAE/GP algorithm in modeling material properties, particularly when enhanced with supplementary structural data such as XRD. The findings also highlight the algorithm's capability to generalize across different datasets without sacrificing accuracy, making it a promising tool for material science applications where predictive accuracy and model generalization are crucial.

4.2. Manipulating Coefficient of Thermal Expansion via Laser Powder Bed Fusion Energy Setting

4.2.1. Motivation

A highly desirable characteristic of Kovar® steel (Fe-balance, Co-17%, Ni-29%) from Carpenter Technology Corporation is its low coefficient of thermal expansion. Initial studies, such as Batch 603 shown in Figure 2, demonstrate the impact of changes in process conditions on the coefficient of thermal expansion. The primary motivation for this research is to identify key process settings and correlate these conditions with the coefficient of thermal expansion.

4.2.2. Method

Kovar® steel with a particle size distribution of 15-45 μm was used in a Renishaw AM400 Laser Powder Bed Fusion (LPBF) machine to investigate the effects of various process parameters. Machine limits for power, velocity (point distance and exposure time), hatch spacing, and scan pattern were provided as the basis for the experiment. A combinatorial set of process parameters was generated and a subset of 90 combinations was selected to manage the number of samples on the build platform. Each parameter setting produced three types of test samples: a density cube, a tensile specimen, and a coefficient of thermal expansion (CTE) specimen. The density cubes were measured using Archimedes testing, tensile specimens were tested using an Instron load cell, and CTE specimens were analyzed using a heat plate with digital image correlation.

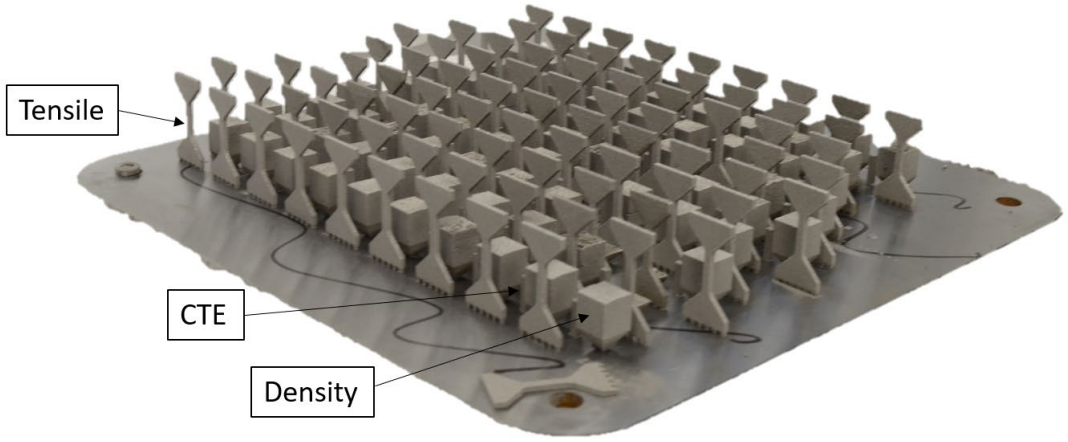

Figure 41. This figure illustrates the manufacturing process of 90 Kovar steel samples using the Renishaw AM400 Laser Powder Bed Fusion (LPBF) machine. The samples were produced under various process parameter settings to investigate their effects on material properties.

4.2.3. Results

The study investigated the effects of various process parameters on Kovar® steel samples produced using a Renishaw AM400 Laser Powder Bed Fusion (LPBF) machine. Coefficient of thermal expansion (CTE) measurements using digital image correlation revealed that the process parameters resulted in CTE values both lower and higher than the nominal Kovar CTE. This investigation was

part of a broader series of studies characterizing Kovar steel. The selected group of samples exhibited a significant disparity in CTE results, prompting further analysis. Despite extensive testing, no direct correlation was found between the measured CTE values and the process parameters. Overall, the data suggest that while optimizing certain process parameters can influence the material properties of Kovar® steel produced using LPBF, the relationship between process settings and CTE remains complex and warrants further investigation.

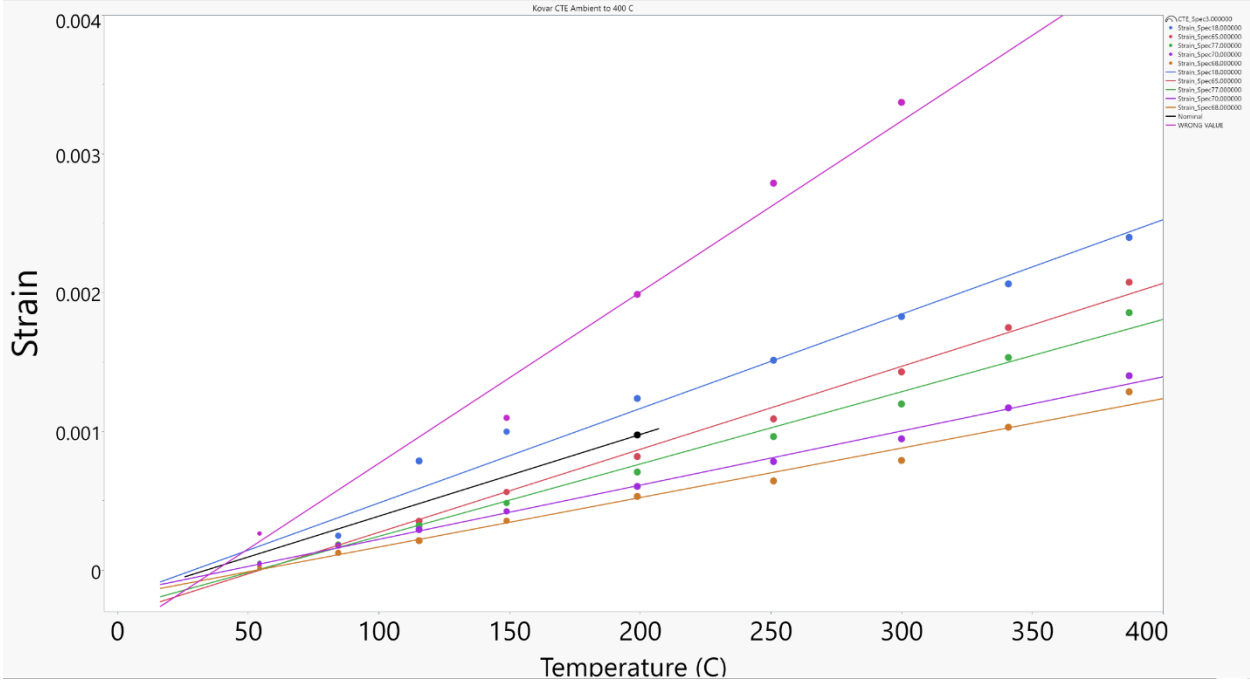

Figure 42. Subset of coefficient of thermal measurements from Batch 603 as a function of change to process settings.

4.2.4. Discussion

This study investigated the effects of various process parameters on the of Kovar® steel samples produced using a Renishaw AM400 LPBF machine. Identifying process parameters that impact CTE has shown success in downstream applications, particularly in matching Kovar CTE to Sandia National Laboratories (SNL) ceramic materials, which has resulted in successful brazed joints and the development of internal components. However, a key lesson learned is the complexity and vastness of the parameter space. A more effective approach may involve first developing a robust understanding of additive Kovar material properties before attempting to explore the extensive parameter space. This foundational knowledge can guide more targeted experiments, ultimately optimizing process parameters to enhance the material properties of Kovar® steel produced using LPBF.

4.3. High Throughput Electrodeposition Process Development

4.3.1. Motivation

The electrodeposition of alloys enabled the development of materials with unprecedented material and performance properties. Controlling the composition and mechanical properties of alloys is challenging due to chemical and electrochemical incompatibilities of different metal salt sources. We have developed an accelerated process built around exploring and mapping the chemical and electrochemical mechanisms of different metal depositions through automation and parallelization. With this method we characterize electrolytes and deposition conditions in a broad scope that allows us to optimize the electrochemical synthesis of alloys with controllable properties.

Several major revisions of how we do electrodeposition research have been developed through this project. Firstly, we have taken advantage of automated tools for solution synthesis. This process allows us to screen qualifying electrolyte solutions for parameters such as solubility while being a surrogate for Ultraviolet-visible (UV-Vis) spectroscopy with batch optical microscopy. Once potentially viable electrolytes have been down selected, we use custom designed, 3D printed electrodeposition cell hardware to ensure that each deposition undergoes consistent set up and conditions while the process is underway while also maintaining large batch numbers. To power and control our cell hardware we have also built a custom tool that manages the deposition currents and voltages, establishes the correct operating parameters for the designated amount of time, and logs dynamic in-situ measurements.

4.3.2. Method

The results section will outline the development of a high throughput plating system and the processes developed to enable high throughput experimentation. These include solubility studies, titration, auto pipettor operation, and hardware development to enable specific deposition parameters.

4.3.3. Results

The first requirement of a suitable electrolyte is the solubility of the metal precursors. This is heavily dependent on the speciation of the metal as it manifests in the electrolyte system, less so on the solubility of the metal salt source which may be completely different. The speciation is an artifact of a few different interacting parameters. The addition of chelating agents will change the speciation of the metal precursor which has a substantial influence on both the solubility and deposition mechanisms. The pH of the solution influences the configuration of the complexing agent, particularly if they are weak acids and can protonate/deprotonate as well as directly influencing the metal precursor. Typically, pH tuning manifests as oxide or hydroxide formation of the metal species at higher pH, which often leads to precipitation.

Temperature also influences solubility but is not generally a stepwise function and trends are typically an increase of solubility at increasing temperatures. We define viable solubility to be determined at room temperature, even if the expectation is that the depositions will occur at elevated temperature. Not only does this ensure that the solutions are always liquid, but it also ensures axillary problems such as precipitation are kept to a minimum and allows solution handling to be significantly simplified.

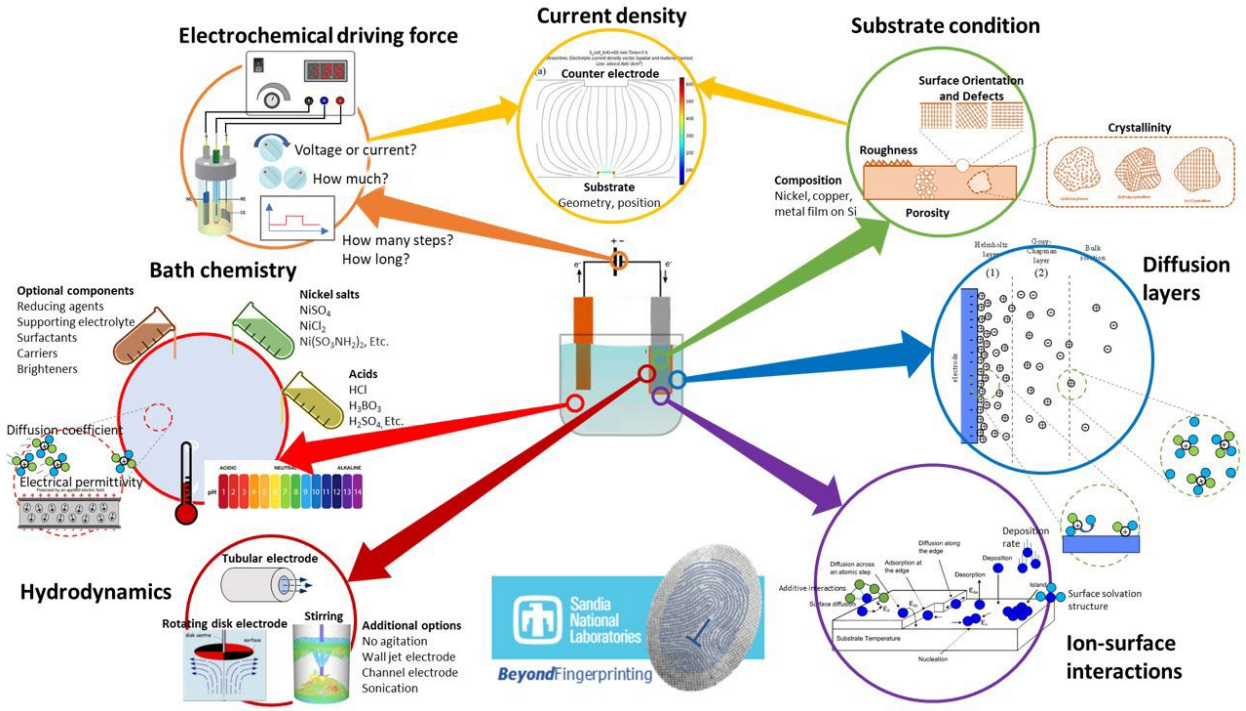

Figure 43. Schematic overview of electrodeposition process and variability.

Auto-pipettor solution making: We used a commercially available auto-pipettor for rapidly generating large numbers of unique solutions. The Opentrons OT-2 was purchased for a previous project and was an ideal fit for the grand challenge effort. Automated pipetting addresses multiple issues facing experimental chemists. The automated process provides precise and reproducible preparation of solutions. This process removes the time intensive labor as well as alleviates many safety concerns when working with acids, bases or other potentially toxic compounds. We embedded a calibration check process involving using 15 vials of known mass and dispensed various volumes of water in each to ensure the volume measurement was accurate prior to making electrolytes.

Our methodology involved the preparation of a series of electrolyte solutions, each distinguished by specific metal salt precursors, complexing agents, and pH levels. Alkaline hydroxides, namely NaOH and KOH, were utilized for the precise adjustment of solution pH, with deionized water serving as the solvent across all preparations. The selection of reagents was guided by their relevance to the desired electrolyte properties, with high-purity metal salts and a range of complexing agents constituting the primary components.

We ran into significant challenges working with a strictly liquid handling system and aiming to generate solutions of uniform volume in which the constituents and products may not be soluble. These challenges stemmed from the need to combine the metal salts with their electrolytes and be in either the high or low pH regime. We found the precursors were not always soluble along the full range of pH values causing precipitation. Additionally, if concentrated base was used the high local pH caused formation of metal hydroxides that were not soluble. The innovation we developed involved starting with two stock solutions. These stock solutions are made with acid sources of complexing agents and additional acid to ensure they could reach the low end of the pH range we were exploring, and then the second stock solution had the same source, with added Na or KOH to reach the high side of the

pH range. The solution handler natively accepts 96 well plates. These plates are critical in the electrolyte screening process because it is able to canvas a large array of electrolyte conditions. For instance, we can sweep from a pure acid stock solution to a pure base stock solution and also have ten pH's along the way. Not only does this process give solubility information but also serves as a rudimentary titration curve giving us an accurate starting point for how to generate a solution of a given composition at any pH we are interested in making. However, due to the solubility of the metal salts in these stock solutions often not representing the solubility across the pH range, we had to be creative in the pre-processing steps for these screenings. To solve this problem, we dissolved our metal salts in water and distributed the solution in all of the needed cells throughout the well plate prior to adding any other material. We then dried these solutions out of well plates, removing all the water and leaving a predetermined quantity of metal salt that generally has low or no vapor pressure. Solutions were then mixed in graded proportions using the auto-pipettor, generating a pH gradient that is the equivalent of adding NaOH or KOH in isolation in a consistent set of other constituents. Using this method, we were able to obtain a wide range of operable pHs with eight different complexing agents at a time.

Once the solutions were made in the well plates they were sealed and mixed and allowed to come to equilibrium for a minimum of 24 hours. The wells were then imaged with a Keyence VHX-7000 microscope with transmitted lighting from the backside. This enables us to log the conformation of the electrolytes, their color changes and if there are any solids in the well due to insolubility. Transmitted light images are show in Figure 44 for different metal precursors, complexing and a pH gradient.

Figure 44. Optical microscope images of Ni Pt Co and Cu solutions with a variety of complexing agents and pH values demonstrating the operating conditions of the respective electrochemical baths.

Once the images were collected, we could easily verify which solutions were to be down selected based on presence of solids. Each of the solutions also had their pH's measured to determine the boundaries

of a particular metal-complex electrolyte. This is only a pass/fail test and allows us to screen and reduce the sample size to only deposit from promising electrolytes. It is obvious to tell which solutions are viable to move forward with a visual inspection, which is where we started with the qualification. However, color analysis is easy to do and provides a more quantitative analysis of the electrolyte. The distribution of the color palate is indicative of the presence of solids, as a fully soluble solution has a completely uniform coloration. A comparison of a solution with precipitate and a fully dissolved salt is shown in Figure 45.

Interestingly, the use of the well plates and the colors of the solution vary as a function of pH. Typically, UV-Vis spectroscopy would be used to provide insight into complexation of the metal and the complexing agents. However, this technique is time consuming if access to an instrument that accepts the 96 well plates is not available or expensive if that instrument needs to be purchased. We made the most of the tools available to us and used the fundamental links between the color and spectroscopy we explored, showing promise of the microscopy as a faster, cheaper surrogate for the spectroscopy technique. A custom python script was used to determine the Red Blue Green (RGB) value of each pixel in the microscopy image. A distribution of those RGB values were then plotted to visualize distribution. This distribution is a direct correlation to the absorbance measured in the UV-Vis instrument and using a machine learning approach we should be able to approximate the spectrum without having to add additional processing steps to the workflow. Figure 45 B and D demonstrate the distribution of RGB values. One key observation we made from these measurements is the more homogenous the solution color is the sharper the distribution of the RGB values. This observation could also be used to automate screening of the solutions that precipitate at the same time we predict the UV-Vis spectrum.

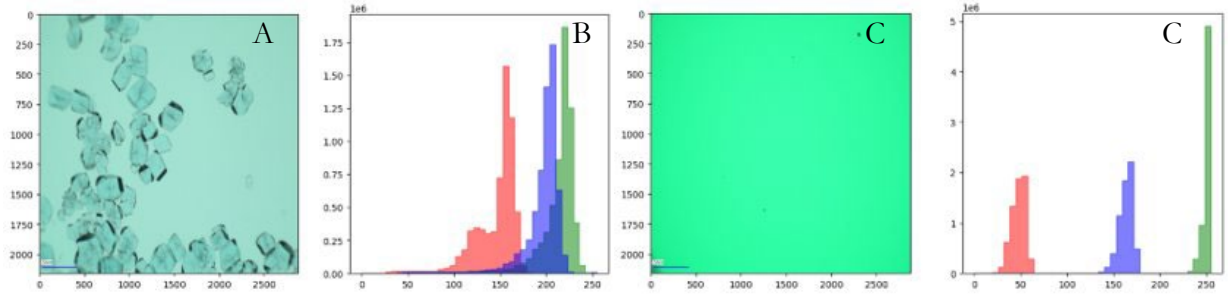

Figure 45. Optical microscope images of Ni based electrolytes with various states of solubility as well as the RGB color distribution of those electrolytes.

Once we have the viability determined by solubility analysis and the pH measured out for each series, we have enough information to scope out the range of solutions that can be continued for further testing as well as the constituent concentrations needed to make each solution at a target pH. This can be quite complicated to predict due to interactions of multiple buffers in the solutions and varies drastically between different metals and complexing agents in use. A plot of the pH vs sodium hydroxide concentration is shown in Figure 46, showing the significant shift in pH due to the addition of the nickel salt precursor.

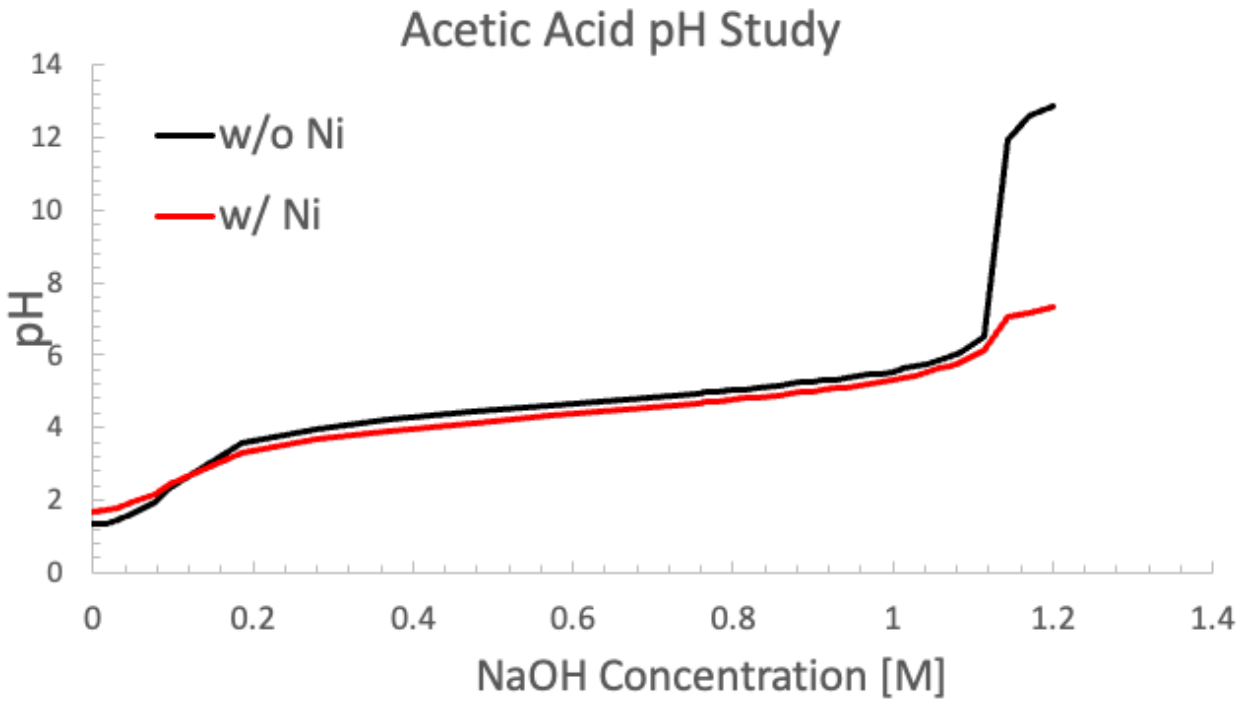

Figure 46. pH curve for acetic acid with and without Ni demonstrating the effect of adding the Ni.

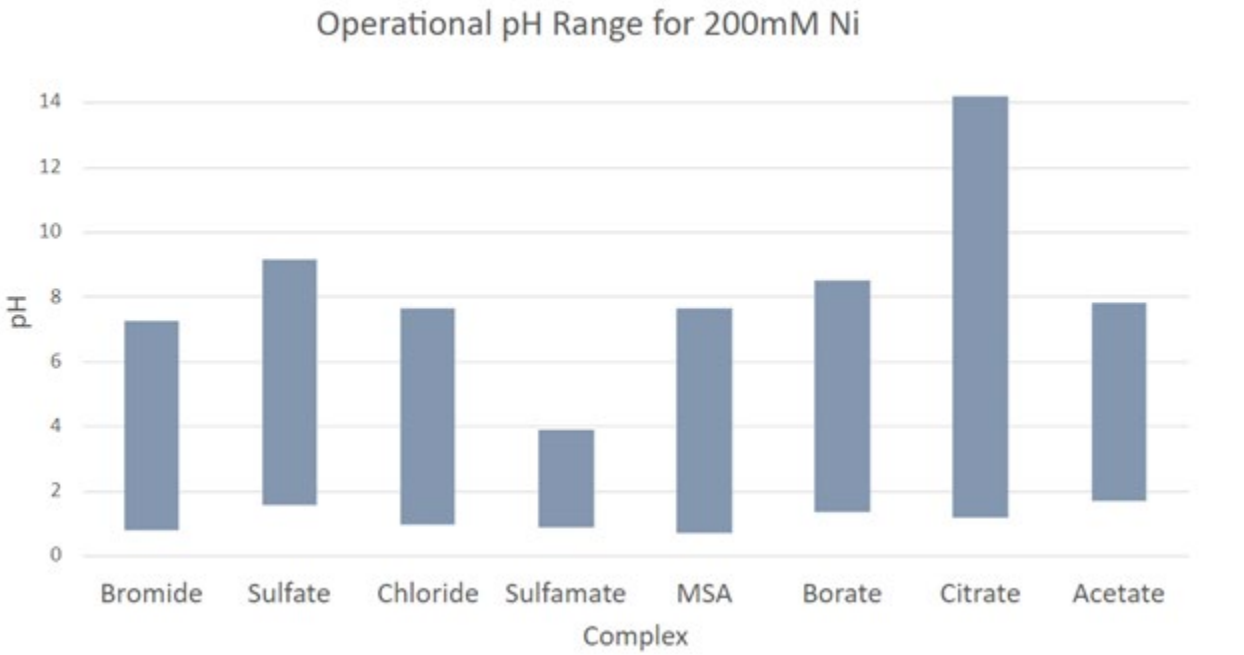

Figure 47. Operating pH ranges for each of the complexing agents tested for Ni.

This process was extrapolated across many different complexing agents and a figure of the full operating regime for each of the complexes can be found in Figure 47. The low pH region seems to

be the most common applicable regime for the 200 mM Ni. Select solutions from this down selection were moved forward to electrochemical testing, described below.

Deposition Hardware: The development of 3D printed templates for electrodeposition cells represents a significant advancement in the field of electrochemistry. By incorporating counter, reference, and working electrodes, along with reusable working electrode substrate holders and built-in electrical connections, these templates offer a streamlined and efficient approach to accelerated electrodeposition experiments. The iterative design of these modular cartridges allowed us to optimize and ultimately simplify the design resulting in a robust system that requires little maintenance. Additionally, the reusability and integrated design of the templates not only enhance experimental reproducibility but also contribute to a more sustainable research practice by reducing the need for disposable components. This effort underscores the potential of 3D printing in advancing high throughput methodologies in electrochemical research, which is a field that has grown accustomed to throughput and scope limitations. These limitations often stem from the long preparation and cleaning stages. By having a modular system, we can prepare several sets of samples at a time parallelizing the entire electroplating process. We decided that 16 parallel depositions at volumes that are 10 mL or less fit our application well; however, the modularity of this system allows it to be rapidly modified to other applications. We attempted to minimize the sample volumes and reduce waste, while maintaining sample sizes and deposition thicknesses that were large enough to suit the post deposition analysis. Limitations with x ray diffraction (XRD) and tribology narrowed the acceptable geometry to 1 cm diameter circle samples and a target thickness of 1 micron. Large samples would likely require larger volumes and you could reduce volumes if you had smaller samples size requirements. We also ran 16 in parallel due to the power supply hardware and data acquisition software accepting 16 inputs. An image of the final product can be found in Figure 48.

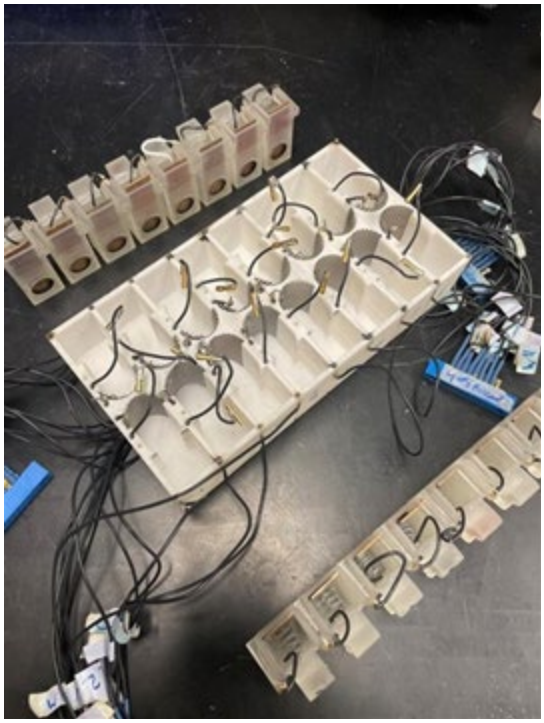

Figure 48. 3D printed well plates and cartridges for the electrochemical deposition system.

The final design was achieved after dozens of iterations and takes advantage of platinized titanium mesh counter electrodes and silver/silver chloride reference electrodes which are generally agnostic to aqueous electrochemical applications. These electrode choices enable us to re-use the same electrodes for different metal sets, which was determined to be the preferrable solution vs attempting to use more specific soluble electrodes, which would not only require different sets of counter electrodes to be purchased and swapped out for each system but would also potentially convolute the results as the influence would be less consistent.

Managing electronic connections was challenging when running this many depositions in parallel. For each cell we have the power circuit which requires two connections as well as a measurement circuit necessitating another two connections. For all channels there are a grand total of 64 connections, so it was imperative we make these connections as effortless and reliable as possible. We integrated pin and socket wire harness electrical connections that could easily be connected and disconnected when needed, this enabled us to make iterations on the hardware without necessitating fully rebuilding the wiring for each. Additionally, the cartridge has a connection to the wells. This is facilitated through IO pin connections. These allow the fast swapping of the cartridges while also making instant connections. Reference and counter electrode connections are integrated into the wells as well. The counter electrode is permanent and thus requires no set up before experimentation; however, the reference electrodes simply need plugged in. The reference electrodes need to spend most of their time in a saturated NaCl electrolyte to prevent voltage shifts. The optimization of the wiring allowed us to easily run diagnostics on the connections as well as significantly reduce the time to set up an experiment.

We have discussed at length the challenges with time and high throughput approaches for electrochemical studies. One aspect that take a substantial amount of time is sample preparation. Our work requires well defined areas of deposition to both facilitate the follow-on material analysis as well as have defined controls of the electrodeposition system so proper sample masking is critical. We opted to use re-usable electrode holders with viton o-rings to seal against the substrate face and define a circular area that was 1 cm in diameter. These 3d printed and spring-loaded cartridges allowed us to easily insert and remove the working electrode substrates. These cartridges also had built in wiring for the electrical connections and building them in banks of 8 enabled bulk connection to a wiring harness which reduced the effort that is normally needed to individually connect each electrode. An image of the well plate and pair working electrode banks is shown in Figure 49, with wiring for all the electrodes in place.

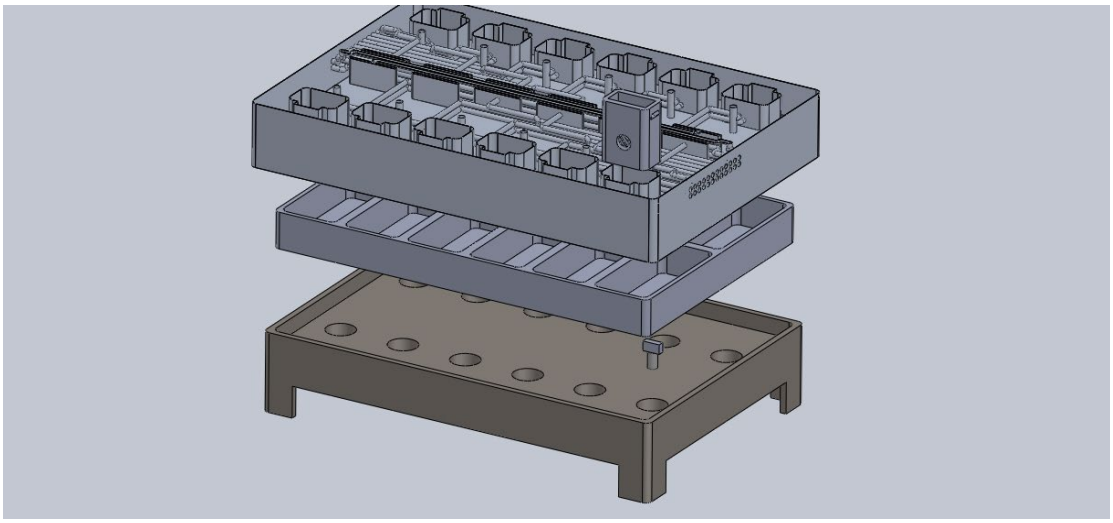

Figure 49. Schematic of the cell stack that included the magnetic stirring as a feature.

We approached control of the electrolyte mixing in 3 different ways. The first of which was to have no solution agitation. The main benefits of this approach are ease of use and consistency between experiments. The main drawback is poor relevance to electrodeposition conditions which generally require some amount of solution agitation to function properly. We implemented magnetic stirrers in each well by addition of a baseplate with an electric motor driving a corrugated bolt attached to gear with magnets under each well. A sample of this version of the system is found in Figure 7. This solved many issues; each well was mixed, and the rotation rates were consistent due to the belt driving all of the gears at the same rate. A large drawback of this process was that each well required the additional step of adding a miniature stir bar, and each stir bar required cleaning steps between uses. Thus, a simplified the mixing process was established by adding vibrating functionality to the well plates. Proof of concept was established using a silicone coated vibrating device that was chemically resistant in case of splashing and was attached to the wells through a 3d printed fixture. This process was easy to implement and reliably consistent over the entire set of experiments; however, the representation of the mixing was also convoluted and unique. Recently we have added an additional well stage that consists of two platforms with isolation springs between. The upper platform housed the agitation while the springs allowed for the energy to remain in the upper stage and also provided smoothing of the agitation for a more uniform mixing across all samples.

There are many options for controlling temperature of the wells, we opted to run the entire deposition set up in an over to ensure that the temperatures were consistent and uniform. Some general issues to be aware of are the dwell time needed to achieve uniform temperature between all the components after they have been placed in the oven and evaporation losses in the wells from sitting at elevated temperature. We measured the temperatures of the electrolyte to ensure it had come up to temperature and kept a water bath in the oven to increase the humidity and mitigate evaporation losses. Additional measures were developed to prevent evaporation such as adding a lid and covering with parafilm. These steps greatly reduced the evaporation of the electrolyte during electroplating.

Opentrons has come out with new hardware since we initially purchased the auto pipettor used for this project. We developed our well plate layout and dimensions with to integrate with auto pipettor capabilities; however, the process still necessitates manually moving well plates to a new area for electrodeposition due to heat and mixing functions. The newer commercially of-the-shelf (COTS)

hardware is capability of moving well plates in the tool and heating and mixing for programmable durations. Integrating electronic connections into this hardware could enable the entire process to be more automatic, drastically increasing the throughput even more than its current status.

Overall, the tools developed for electroplating have overcome many challenges typically associated with high throughput electroplating experimental setups. Figure 50 depicts the advances we have made on the time it takes to generate our samples. We have effectively designed hardware that allows us to minimize the time and effort required to generate these samples. The next major improvement in this workflow is utilizing solution handlers to aid in electrolyte preparation. There are currently two facets of our workflow that require the most time. Solution preparation and sample masking. Solution prep takes so long because we are often interested in very specific conditions, if we were able to use the opentrons to make the larger volumes of solutions we can reduce the amount of time we take to correct the pH to the values we are interested in. Furthermore, the use of gold on wafers eliminates the need to activate the substrate; however, it requires us to make front side connection in a system designed to make backside connection. We do this through the addition of a copper foil. Adding this to the samples is time intensive and also requires us to test electrical connection to of the cell. This may be the price to pay to ensure that we are plating on an active surface every time.

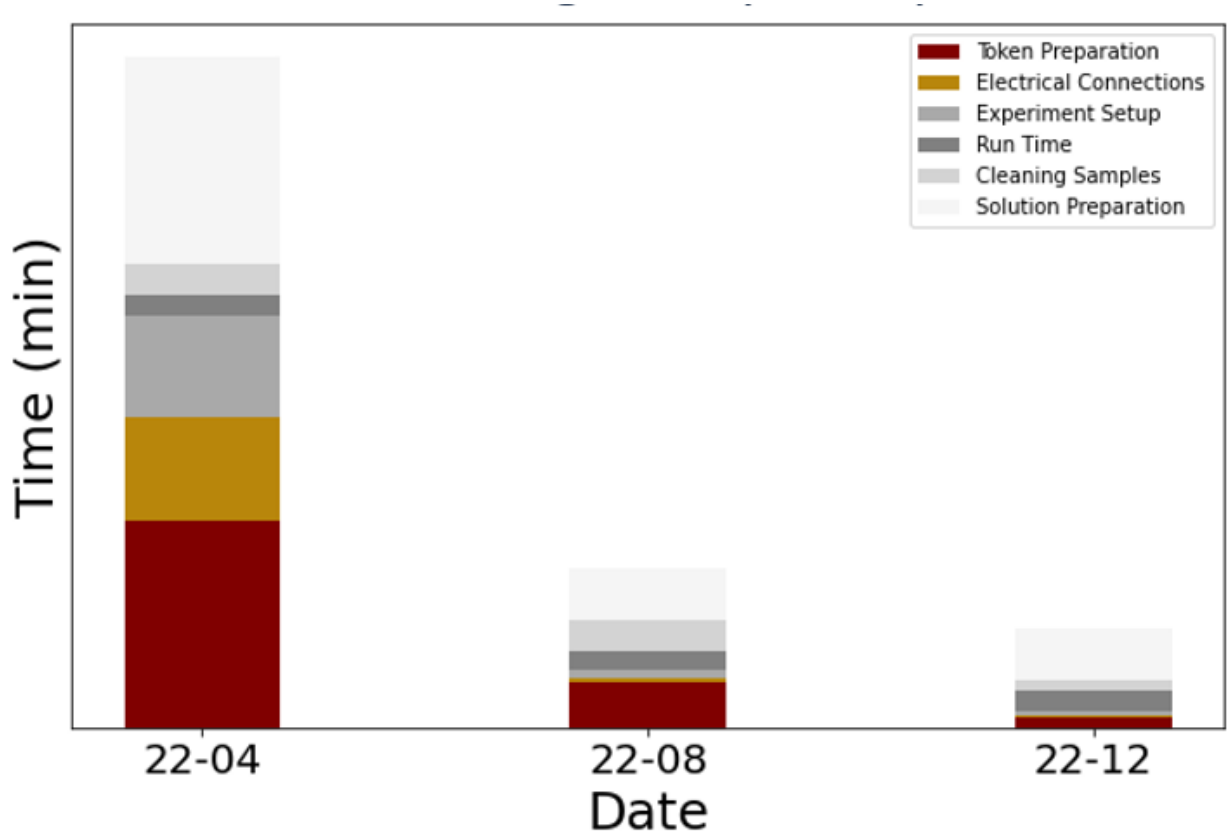

Figure 50. Time investment vs major iteration of the high throughput experimental system.

Deposition power control: Our team designed and acquired state-of-the-art NI power supply system. This system was supported by the concurrent development of a custom LabVIEW software program, specifically designed to meet the demands of electrodeposition research, including precise control and measurement of electronics with respect to current, voltage and time. A standout feature

of this new power supply is its capability to run 16 channels in parallel, significantly increasing the throughput of experiments and enabling simultaneous processing under individualized conditions. The hardware's level of precision ensures that the experimental conditions are consistent across all channels, thereby improving the reproducibility of results. The Hardware can be found in Figure 51.

Figure 51. 16 channel setup for the electrochemical depositions.

This power supply system utilizes custom LabVIEW software, designed from the ground up to offer the necessary control and monitoring capabilities. The software facilitates precise control of current and voltage across each of the 16 channels. Furthermore, the software includes real-time monitoring and data logging features, enabling researchers to track the progress of experiments and make informed adjustments as needed, as well as convenient data handling post processing which is imperative for the follow up analysis and machine learning goals. The custom operating graphic user interface (GUI) is shown in Figure 52.

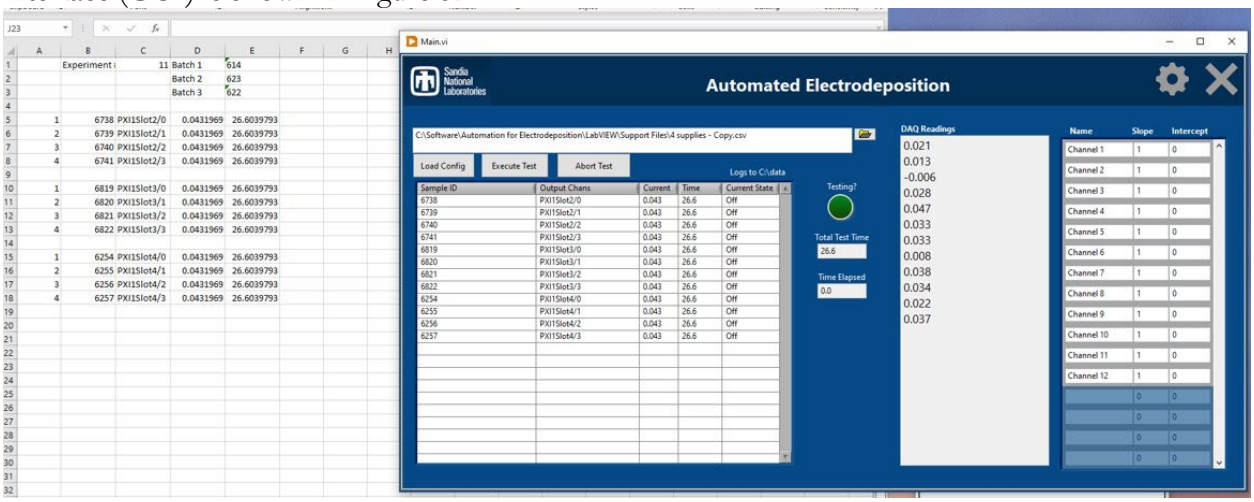

Figure 52. User interface and example of the cell initialization file for the data acquisition software.

The integration of the new power supply system into our laboratory workflow has been challenging, but thanks to the intuitive design of the LabVIEW software and the robust performance of the hardware we have seen rapid gains in our process flow. We have adapted to the new system, leveraging its capabilities to expand the scope and scale of electrodeposition experiments. The system's user-

friendly interface and automated features have reduced the manual workload associated with setting up and running experiments, allowing our lab to focus more on defining new experiments, analysis, and innovation. An example of the voltage time series data for different nickel deposition experiments running at variable current densities is shown in Figure 53.

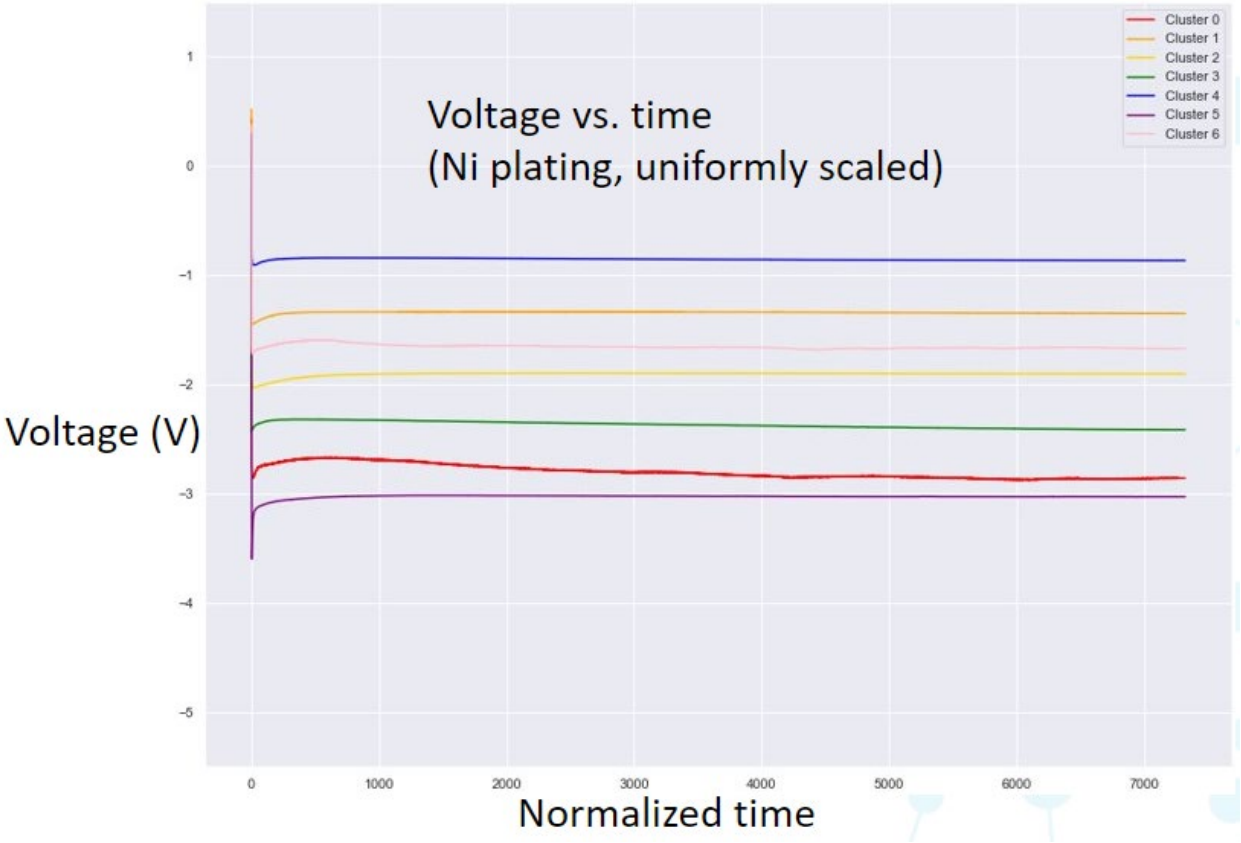

Figure 53. Voltage vs time trace for Ni deposition experiments as an output from the Data Acquisition (DAQ) system.

The ability to conduct 16 electrodeposition experiments in parallel represents a significant leap forward in experimental throughput. This multi-channel approach not only accelerates the research process but also opens new avenues for systematic studies of electrodeposition parameters, which is core to this grand challenge effort. By running experiments in parallel, we can efficiently explore a wide range of conditions, such as varying current densities or electrolyte compositions, within a fraction of the time required for sequential experiments. This high-throughput capability is particularly beneficial for optimization studies and the development of new materials, where a large dataset is crucial for identifying viable or optimal conditions.

The culmination of these process improvements has enabled us to deposit individualized unique samples at an unprecedented rate in our lab. Figure 54 is an image of 200 samples plated in an afternoon with 3 people's efforts (1 staff, 1 postdoc and 1 undergrad intern). 200 unique depositions is often more than are produced during a project's entire run.

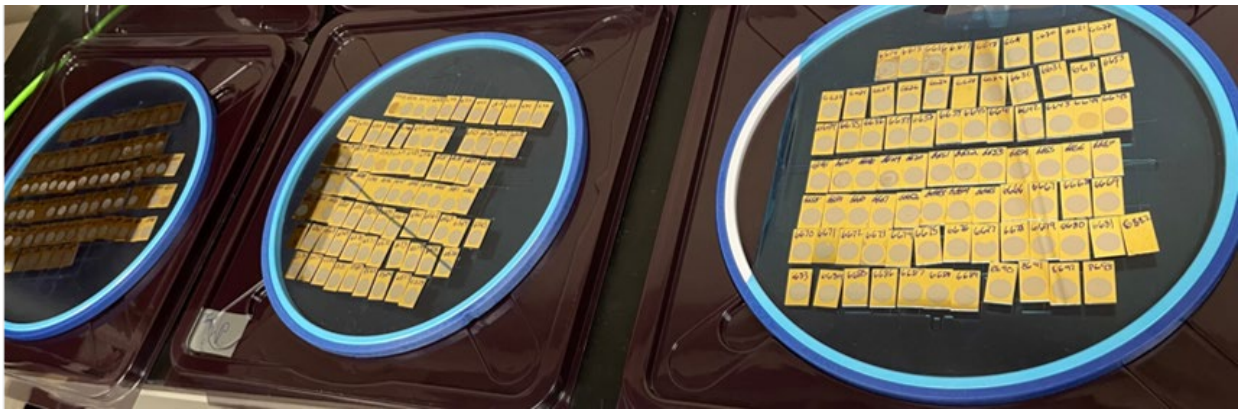

Figure 54. 200 Ni plated samples plated using the high throughput tooling over the course of one afternoon.

4.3.4. Discussion

We have explored the deposition of nickel and platinum with additions of 16 different complexing agents, some common and some less conventional to discover satisfactory deposition options for alloy synthesis. This process is novel not only because of our high throughput methodology but the focus on generating the best alloy deposition electrolyte instead of taking common nickel or platinum systems that may be better performing for deposition of pure films and adding a second metal source. The increased screening and processing system we have built is enabling for this methodology shift, where we are less limited by the vast number of electrolytes and depositions needed to screen electrolytes from scratch.

4.4. Use of High Throughput and Machine Learning Integration for the Exploration and Optimization of Electroplated Ni, Pt, and NiPt Alloys

4.4.1. Motivation

Nickel and platinum are heavily utilized metals across various industries and are often used coating layers. Both Ni and Pt offer corrosion resistance in harsh chemical environments. Ni is also ferromagnetic, making it useful in electromagnetic applications. Pt is widely known for its exceptional catalytic properties, electronic conductivity, and high-temperature stability. Together, NiPt alloys have shown enhanced catalytic activity and selectivity—as they combine the properties of both metals. NiPt alloys also show improved mechanical and corrosion properties over the pure elements.

Given its utility (efficient use of materials, precise control over coating properties, and versatility across a wide range of substrates), electroplating is an often used, and desirable, synthetic method for creating coating layers and has been used to produce Ni and Pt films for a long time (e,g. the first practical recipe for Ni was discovered/developed in 1843). While NiPt alloys have also been electroplated before, little exists in the way of broad systematic study aimed at mapping wide chemical and processing spaces. Below is a description of work in which high-throughput testing and characterization methods were applied in an attempt to accelerate the workflow necessary for exploring vast empirical domains.

4.4.2. Method

A series of Ni and Pt electrolytes were prepared by dissolving $NiSO_4$ or H_2PtBr_6 in aqueous solutions containing one of a series of 15 different chemicals/ligand-types, shown in Table 1. Ligand chemistries were chosen to explore both chemistries with established precedent and expand into new chemical territory—namely with the use of combined carboxylate and amine functionalities in amino acids as well as the use of less traditional functionalities in this space in sulfolane and thiourea.

Acidic stock solutions of each chemistry were prepared by dissolving 1 M of the respective ligand in water, except for citrate and borate which were prepared at concentrations of 0.5 M and 0.4 M, respectively. 0.5 M $(NH_4)_2SO_4$ was made to produce 1 M NH_4^+. For SO_4^{2-}, Cl^-, and Br^- chemistries, 0.9 M of the corresponding sodium salt was combined with 0.1 M of the associated acid (H_2SO_4, HCl, HBr). 0.1 M H_2SO_4 was also common to all solutions. Each acidic stock solution was titrated with 15 M NaOH to measure the exact concentrations of H_2SO_4 and acid form of the ligand of interest. Basic stock solutions were made by adding enough NaOH to the acid stock solutions to get the pH to about 13. The accurate acid concentrations, from titrations, were used to determine the volumes of acid and base stocks to combine to create targeted pHs for plating electrolytes. Electroplating electrolytes were prepared with appropriate ratios of acid and base stock solutions, dissolving $NiSO_4$ at 0.2 M (for Ni depositions) or 0.025 M H_2PtBr_6 (for Pt depositions).

Current efficiencies were estimated from XRF peak intensities of the respective metal peaks. XRF intensities were calibrated to corresponding thicknesses by creating a calibration curve for XRF intensity vs. known metal thickness.

Table 2. Ligand chemistries explored for Ni, Pt, and NiPt electroplating.

	Most Acidic		-H1		-H2		-H3
Ligand	**Formula**	**pka1**	**Formula**	**pka2**	**Formula**	**pka3**	**Formula**
Thiourea	SC(NH)2	*13.87*					
sulfolane	C4H8SO2	*13*					
Ammonia	[NH4]+	9.25	NH3				
Borate	BO3H3	9.15	[BO3H2]-				
Acetate	H3C2O2H	4.76	[H3C2O2]-				
Citrate	C6H5O7H3	3.128	[C6H5O7H2]-	4.761	[C6H5O7H]2-	6.396	[C6H5O7]3-
Phosphate	PO4H3	2.15	[PO4H2]-	7.2	[PO4H]2-	12.35	[PO4]3-
Malonate	H2CO4H2	2.83	[H2CO4H]-	5.69	[H2CO4]2-		
Alinate	H3CNH2O2	2.34	[H3CNH2O2]-	9.69	[H3CNHO2]2-		
Glycate	H2NCH2O2	2.34	[H2NCH2O2]-	9.6	[HNCH2O2]2-		
Prolate	H7C5NHO2	1.99	[H7C5NHO2]-	10.6	[H7C5NO2]2-		
Sulfamate	H2NSO3H	1	[H2NSO3]-				
Methane Sulfonate	H3CSO3H	-1.9	[H3CSO3]-				
Sulfate	H2SO4	-3	[HSO4]-	1.92	[SO4]2-		
Chloride	HCl	-6.3	Cl-				
Bromide	HBr	-8.7	Br-				

4.4.3. Results

Role of the Substrate: Bronze vs. Au(111)/Si(100)

Focusing on Ni electrodeposition, the ligands in Table 2 were investigated. The first series of depositions was conducted on bronze substrates. These were primarily chosen to improve electrical contact and leak proofing of the deposition wells; the bronze substrates were purely metallic allowing backside contact. However, the surface finish of the bronze substrates was not ideal as received (several prominent scratch marks) and even polishing with a computer numerical control (CNC) mill did not create the ideal mirror-like, smooth surface desirable for a study trying to isolate variables like initial substrate surface morphology. So, thereafter we chose to return to Au/Si substrates.

While switching to the Au substrates provided a condition removing initial surface finish as a variable it had the unfortunate consequence of causing our electrodeposits to grow in an epitaxial-like fashion, following the crystalline orientation of the Au(111) substrate. X-ray diffractograms showed only <111> peaks for Ni deposits. To address this issue, we began targeting thicker films in our plating protocol, as it is known—and we discovered—that thicker deposits will eventually relax from the strain associated with matching the substrate's orientation, leading to whatever crystalline orientations (texture) the processing parameters (namely chemistry and current density) create when free from substrate-directed growth. As of this writing XRD has not yet been acquired for thicker deposits on Au(111) substrates.

Ni, Pt, and NiPt Electrodepositions in Various Chemistries and Across a Range of Current Densities

The general procedure for conducting our electrodeposition experiments was to perform depositions at 5, 25, and 75 mA/cm^2 within different chemical environments. Given the vastness of possible

inputs to explore a first-pass experimental matrix was assembled with the intention of minimizing experimentation while still maximizing representation of chemical and energy/current space. Figure 54a shows first-pass heat maps for Ni and Pt plated on Au at 5 and 25 mA/cm^2. With these maps the researcher can quickly identify where Pt and Ni overlap, in terms of plating ability/behavior. The researcher can also quickly identify gaps that ought to be further explored. Figure 54b shows a second series of Ni depositions performed based on identified gaps in the first pass. These experiments identified acetate in the pH 4-7 range as a promising chemistry for Ni and Pt co-deposition at 5 and 25 mA/cm^2. Bromide chemistry at pH 6-7 was also a promising chemistry.

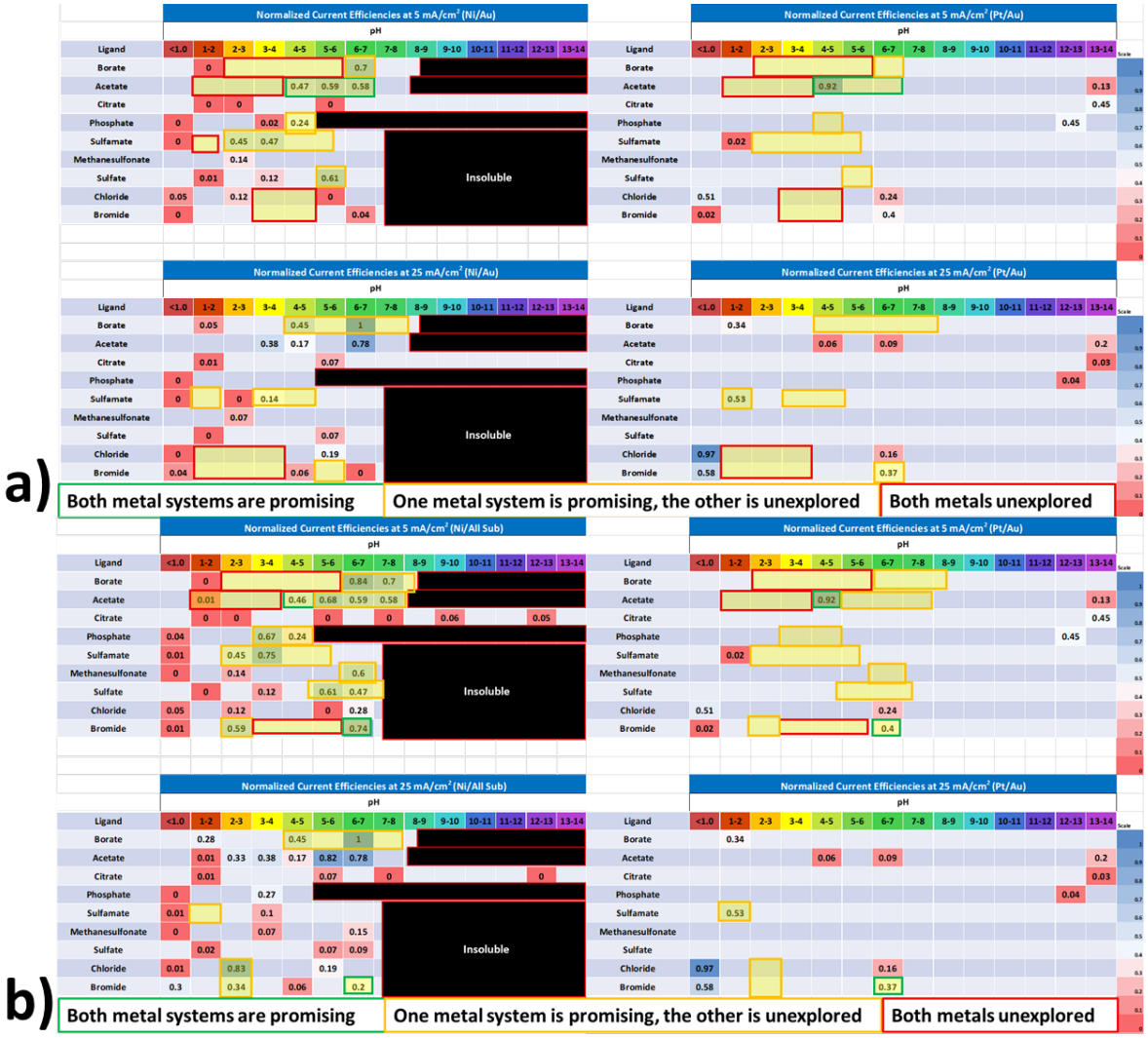

Figure 55. Heat maps of normalized current efficiency for a) First-pass Ni and Pt depositions and b) Second-pass Ni and Pt depositions. Ni depositions are on the left, Pt on the right. 5 mA/cm2 was used for the top maps while 25 mA/cm2 was used for the bottom maps. Chemistry/ligands are displayed in the row headers while pH ranges are displayed in the column headers. Each cell represents the average normalized current efficiency measured for the given experimental conditions.

Attempts to electroplate NiPt alloys were made at 25 and 50 mA/cm^2, varying both the ligand chemistry and the concentration of Ni and Pt salts. Results are shown below in Figure 55.

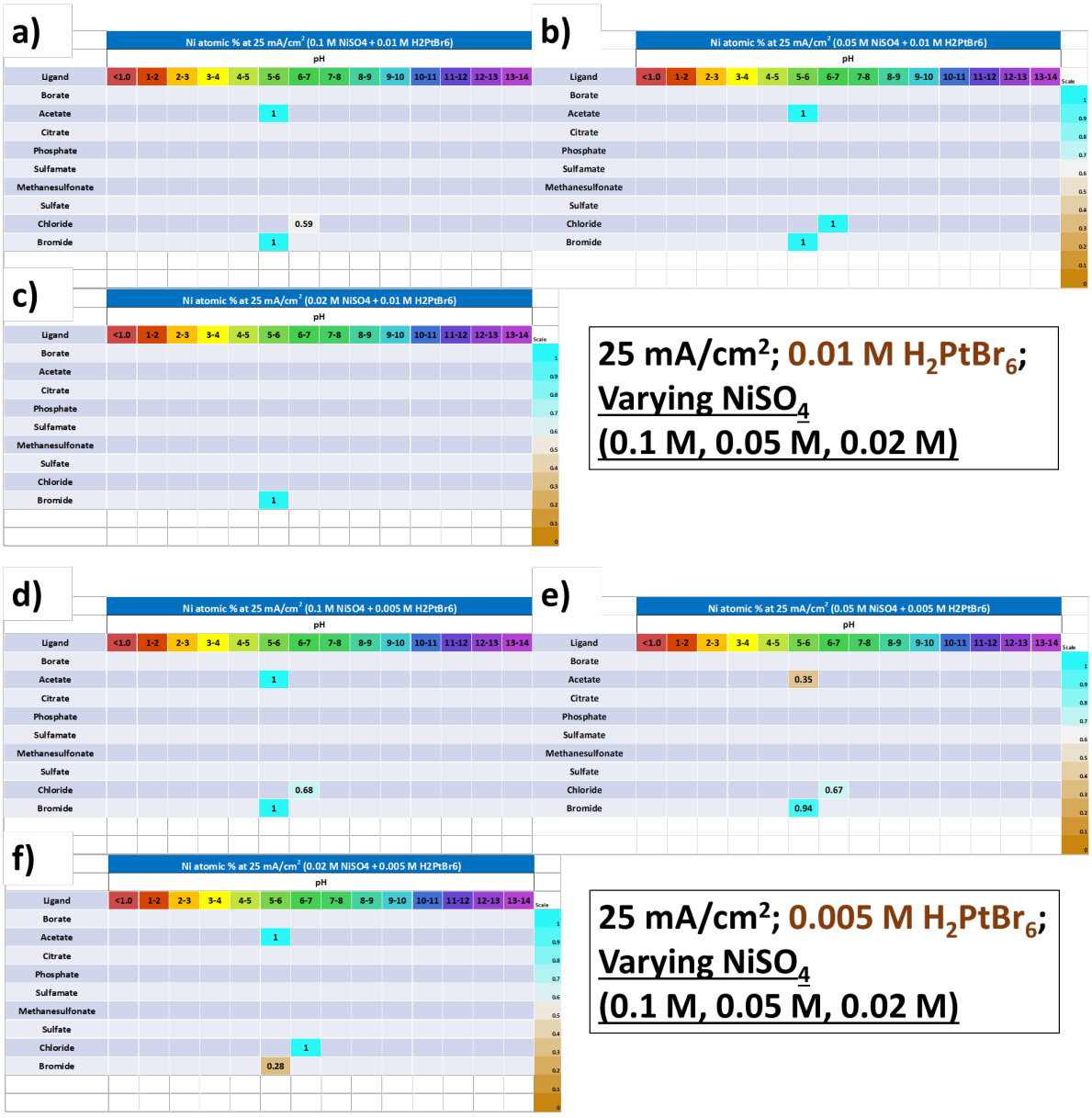

Figure 56. Heat maps of normalized current efficiency for a) First-pass Ni and Pt depositions and b) Second-pass Ni and Pt depositions. Ni depositions are on the left, Pt on the right. 5 mA/cm2 was used for the top maps while 25 mA/cm2 was used for the bottom maps. Chemistry/ligands are displayed in the row headers while pH ranges are displayed in the column headers. Each cell represents the average normalized current efficiency measured for the given experimental conditions.

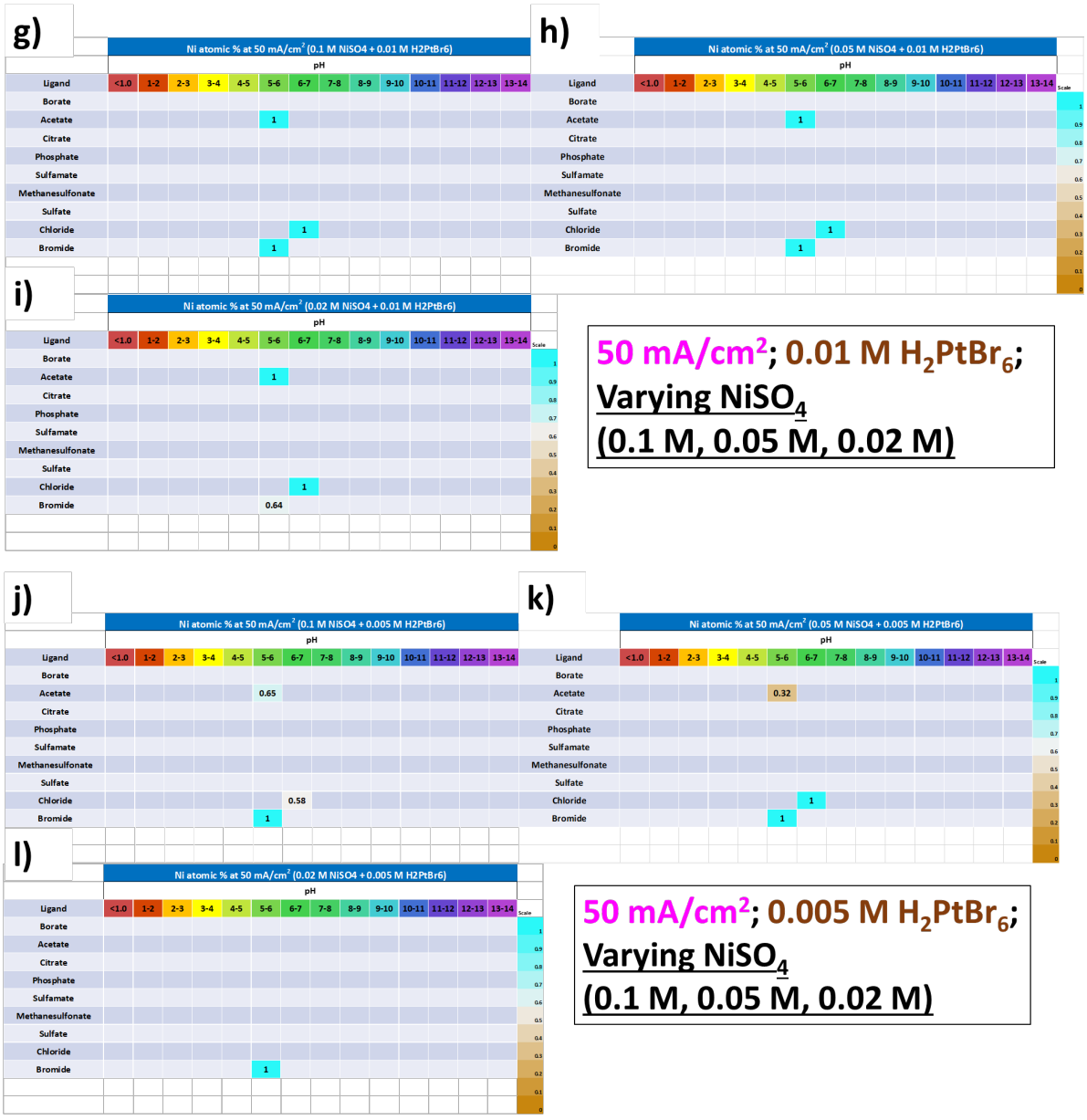

Figure 57. Attempt to electroplate NiPt.

4.5. Kinetics and Deposition Performance of the Nickel-Glycine Electroplating System

4.5.1. Motivation

Glycine has long been used as an additive in electroplating chemistries. However, its exact working mechanisms are not known. The current work sought to study this system more deeply using kinetic analysis. In the nickel-plating system, it was found that the kinetics of deposition, quantified using exchange current i_o, for glycine outperformed that of saccharine, boric acid, and L-proline. i_o had a 3rd order dependence on the concentration of glycine, directly corresponding to the maximum number of ligands around Ni^{2+}. Under concentrated conditions (1.2M) and elevated temperature (40C), baths comprised of the $Ni(Gly)_3$ coordination complex yielded faradaic efficiencies of 78.7, 82.3, and 64.5% at 20, 40, and 80 mA cm^{-2}. It was found that the grain size and texture were invariant with current density, giving a grain size of 10.16 nm and a texture coefficient of 2.1 for the (111) crystal plane.

4.5.2. Method

Electrochemical experiments were carried out in 60ml solutions with a constant amount of 0.3M Ni^{2+} in the form of $NiSO_4$. All molecular additives for screening studies were used at a concentration of 0.05M. The pH for glycine, proline, saccharine, and boric acid were 4.8, 5.05, 4.77, and 6.21. To synthesize $Ni(Gly)_2(H_2O)_2$, a metal to ligand ratio of 1:2 was used and tested at a pH of 8. For $Ni(Gly)_3$, a ratio of 1:3 was used and tested at a pH of 10. pH was adjusted with either 98% Sulfuric Acid or KOH pellets. A stir rate of 300 rpm was used during measurements. All experiments conducted in 3-electrode beaker cells with Ag/AgCl reference, a titanium mesh anode, and a 1.2 to 1.8 cm^2 area coupon, either a (111) Au substrate on silicon. All chemicals were purchased through Sigma Aldrich. Exchange current was calculated from LSV curves ran from 0 to -1200mV at 2.5 mV/s. Because each additive alters the concentration of protons in solution, a correction was applied to account for this. Corrected exchange currents were found by calculating the expected i_o at the measured pH after adding the catalyst based on the exponential fit equation of figure 1(a), $y = 1740.6x^{-7.902}$. This value was then subtracted from the measured value to get the 'true' rate enhancement due to the catalyst alone. LSV curves and chronopotentiometry measurements were generated using a Voltalab PGZ402 universal pulse dynamic-EIS voltametery instrument. SEM images were acquired using a FLEXSEM Hitachi SU 1000III at an accelerating voltage of 18kEV at a working distance of 10mm. XRD was gathered using a Bruker D2 Phaser using a Cu Kα X-Ray source.

Overpotential was measured by $\eta = V_{exp} - E_o$, where E_0 is the standard reduction potential of $Ni^{2+} + 2\ e^- \rightarrow Ni^0$. This value was -0.454 V (v.s. Ag/AgCl) for un-complexed species. For Ni-glycine complexes, the reference potential used was $Ni(NH_3)_6 + 2e^- \rightarrow Ni^0 + 6\ NH_3$ as no reference potentials for the $Ni(Gly)_3$ complex were found. This value was -0.686 V (v.s. Ag/AgCl). Texture Coefficient was calculated using:

$$T.C. = \frac{\frac{I(hkl)}{I_{ref}(hkl)}}{\frac{1}{n}\sum_1^n \frac{I(hkl)}{I_{ref}(hkl)}} \qquad (1)$$

Where I_{ref} is the reference intensity of polycrystalline Ni metal gathered from the NIST database. Grain size was calculated using the Scherrer Equation:

$$D = \frac{K\lambda}{\beta cos\theta} \qquad (2)$$

where K is Scherrer's Constant (0.94), β is the breadth of the peak at full-width-half-max (FWHM), cos(θ) is the cosine of the angle where the peak of interest occurs (measured for the (111) Ni peak in

this study), λ is the incident wavelength (1.54 angstrom for Cu Kα), and D is the crystallite size (in nanometers).

4.5.3. Results

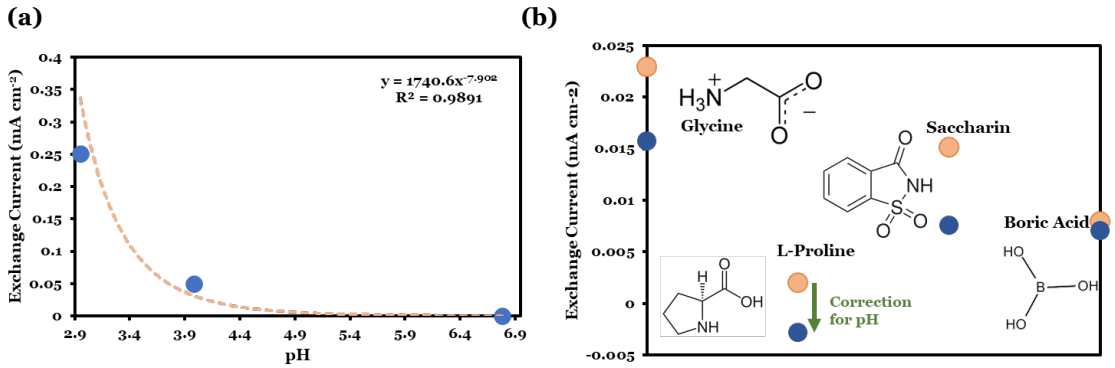

Figure 58 (a) Exchange current (i_o) v.s. pH for nickel reduction, (b) i_o for each additive with pH corrections

Figure 58(a) shows how i_o varies with pH in a pure Ni^{2+} solution. It was found that i_o decayed exponentially with pH in pure Ni^{2+} solutions. Figure 58(b) shows the effect of different catalysts on the exchange current. Orange dots are the original values while dark blue dots are the pH corrected values. It was found that glycine gave the largest exchange current (0.0229 mA cm^{-2}), followed by saccharin (0.015), boric acid (0.0079), and L-proline (0.0020). Figure S1 shows Tafel plots and LSV data used to extract i_o.

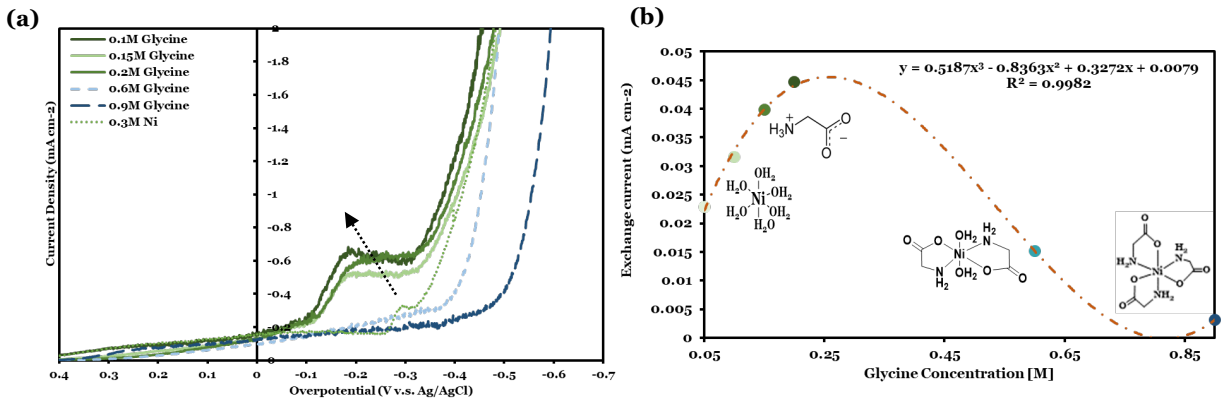

Figure 59. (a) Linear sweep voltammetry (LSV) of chemistries as a function of concentration of glycine (b) i_o as a function of glycine concentration

Figure 58(a) shows LSV scans as a function of glycine concentration. It is seen that as the concentration of glycine increases, a plateau region starts to form and shift towards lower potentials. For complexes $Ni(Gly)_2(H_2O)_2$ and $Ni(Gly)_3$, no peaks can be seen. The large increase in current starting around -0.4 V (v.s. Ag/AgCl) shifts for complexes towards more negative potentials. Figure 58(b) shows i_o as a function of glycine concentration. It is seen that a low concentration (< 0.25M),

i_o increases linearly. After this point, i_o falls after Ni-glycine complexes form. Overall, the current was fitted to a 3rd order polynomial. This suggests that 3 glycine molecules are involved in the deposition of Ni, which corresponds to the maximum coordination of nickel by glycine, $Ni(Gly)_3$.

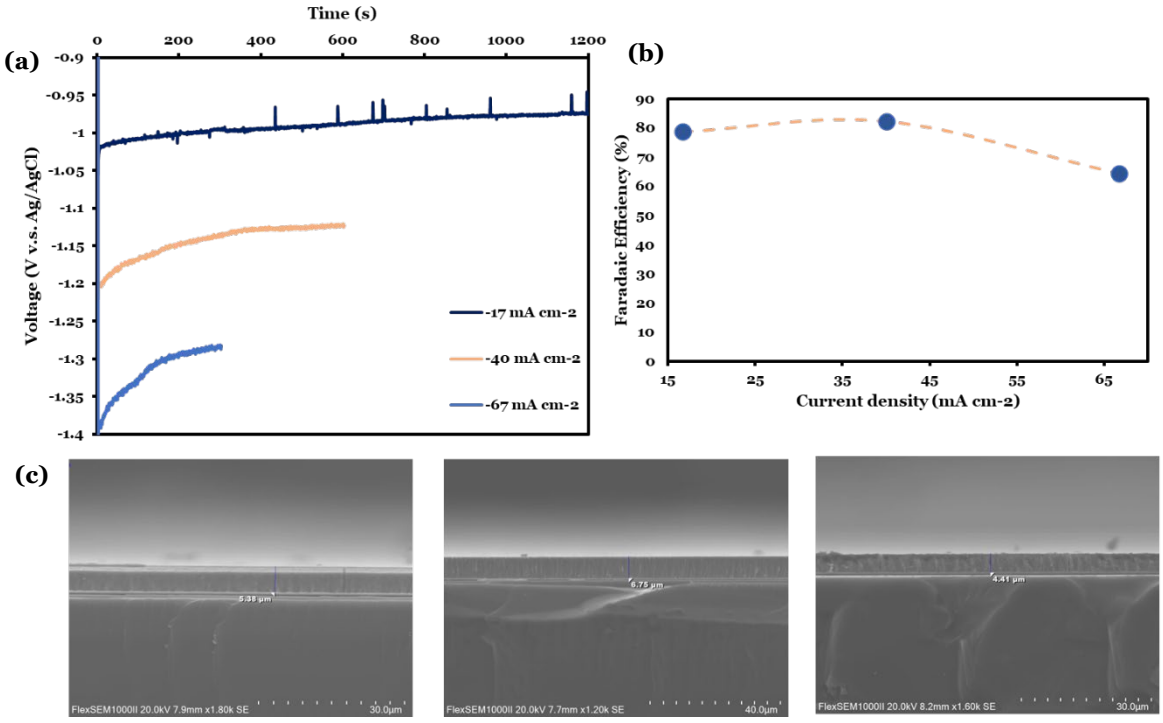

Figure 60. (a) Chronopotentiometry as a function of time, (b) Faradaic efficiency as a function of current density, (c) SEM images at -17 mA cm^{-2}, -40 mA cm^{-2}, and -67 mA cm^{-2}, from left to right.

Figure 60(a) shows chronopotentiometry for a 1.2M $Ni(Gly)_3$ chemistry operated at 40C°. A current of -17 mA cm^{-2} was applied for 20 minutes, a current of -40 mA cm^{-2} was applied for 10 minutes, and a current of -67 mA cm^{-2} was applied for 5 minutes. It was found that the required overpotential to maintain a given rate increased with applied current. Some instability was seen at a current density of -17 mA cm^{-2}, while -40 and -67 stable over time. Figure 60(b) shows the calculated faradaic efficiency as a function of applied current. A faradaic efficiency of 78.7, 82.3, and 64.5 % were attained at a current of -17, 40, and 67 mA cm^{-2}, respectively. Figure 60(c) shows SEM cross-sections acquired at each current. Each film was uniform and compact, with -40 mA cm^{-2} giving the thickest film.

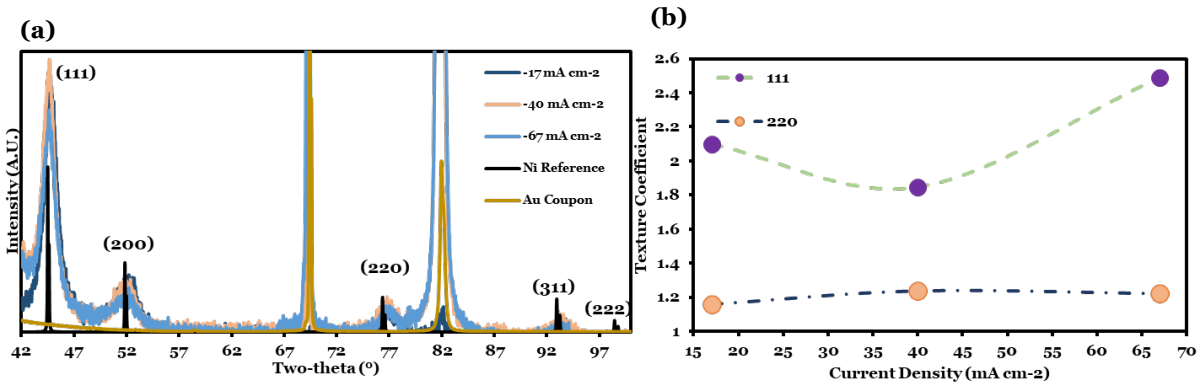

Figure 61. (a) XRD as a function of current density (b) Texture coefficient for the (111) and (220) crystal plane as a function of current density.

Figure 61a shows XRD of the deposited $Ni(Gly)_3$ film as a function of current density. It was found that all films show similar structure with a grain size of around 10.16 nm. Texture analysis found films deposited at -67 mA cm^{-2} had a strong (111) texture.

4.5.4. Discussion

The work describes the investigation of glycine in nickel plating, where kinetic analysis and performance testing showed the chemistry to have promise for future study.

4.6. Electrodeposition of Cobalt films from the Cobalt Tri(L-Prolinato) Complex

To date, all literature reports of electrodeposited cobalt have shown films that are rough and grown with low-to-moderate current efficiency. Here, we describe the deposition of cobalt from tris(L-prolinato) complexes. At a constant current density of 10 mA cm^{-2}, a 3.32 μm thick film was deposited at 64.5% Faradaic efficiency. At 40 mA cm^{-2}, a 5.91μm thick film was deposited at 28.72% efficiency. At 10 mA cm^{-2}, the film had a purity of 95.4% (weight % Co), as measured using Energy Dispersive X-ray Spectroscopy (EDS). From XRD measurements, the films show strong (220) texture with a grain size of 14 nm. UV-VIS spectroscopy found that the electronic structure of $Co(Pro)_3$ greatly differs from the "standard" aqueous $Co(H_2O)_6$ complex. Density Functional Theory (DFT) calculations show that L-Proline forms a weak, water-like solvation shell around Co^{2+}. We believe this metal complex to hold great promise for electrodeposition of cobalt.

4.6.1. Methods

The formation of tris-Prolinato was based off a report by Kato *et al.* [42] $Co(Pro)_3$ was synthesized using 0.3M Co^{2+} in the form of $CoSO_4$. L-Proline was used in a 3:1 ratio to Co^{2+}. The complex was formed by mixing ligand and metal in solution and slowly increasing pH to a working value of 11. The solution was mixed overnight at room temperature. The pkA values of L-Proline are 2.0 for the carboxylic acid group and 10.6 for the pyrrolidine group [43]. pH was adjusted using KOH pellets. All chemicals were purchased from Sigma Aldrich. A stir rate of 300 rpm was used during measurements. All experiments were conducted in 3-electrode beaker cells with Ag/AgCl reference, a Ti mesh anode, and a 1.2cm^2 electron beam evaporated (111) textured Au film on a Si coupon. Chronopotentiometry and linear sweep voltammetry was generated using a Voltalab PGZ402 universal pulse dynamic-EIS voltametery instrument. SEM/EDS was acquired using a FLEXSEM Hitachi SU 1000III at an accelerating voltage of 18kEV at a working distance of 10mm. UV-VIS was captured using a Thermoscientific Genesys150 from 190nm to 1100nm in plastic cuvettes. XRD was gathered using a Bruker D2 Phaser using a Cu Kα X-Ray source.

Overpotential was measured by $\eta = E_{exp} - E_o$, where E_o is the standard reduction potential of $Co^{2+} + 2e^- \rightarrow Co^0$ (-0.474V v.s. Ag/AgCl). Texture Coefficient (T.C.) was calculated using:

$$T.C. = \frac{\frac{I(hkl)}{I_{ref}(hkl)}}{\frac{1}{n}\sum_1^n \frac{I(hkl)}{I_{ref}(hkl)}} \quad (3)$$

where I_{ref} is the reference intensity of polycrystalline Co metal gathered from the NIST database.

Grain size was calculated using the Scherrer Equation:

$$D = \frac{K\lambda}{\beta cos\theta} \quad (4)$$

where K is Scherrer's Constant (0.94), β is the breadth of the peak at full-width-half-max (FWHM), cos(θ) is the cosine of the angle where the peak of interest occurs (measured for the (111) Ni peak and the (220) peak for Co in this study), λ is the incident wavelength (1.54 angstrom for Cu Kα), and D is the crystallite size (in nanometers).

All electronic structure calculations are done using the QUANTUM ESPRESSO package [44]. We use norm-conserving pseudopotentials from the PseudoDojo repository [45] and the Perdew-Burke-Ernzerhof (PBE) exchange-correlation functional [46]. We use kinetic energy cutoffs of 50 Ry and 400 Ry for the plane wave basis sets used to describe the Kohn-Sham orbitals and charge density,

respectively. We use a 2x2x2 Monkhorst-Pack grid [47] to sample the Brillouin zone in our calculations.

We place each molecule inside a 15 $Å^3$ box and allow geometry optimization until the interatomic forces are lower than 50 meV/Å. To simulate the solvation environment of the molecule, we use the self-consistent continuum solvation method as implemented Environ package for Quantum Espresso [48]. For charged molecules, we use the Martyna-Tuckerman correction to avoid issues around periodic boundary conditions [49].

4.6.2. Results and Discussion

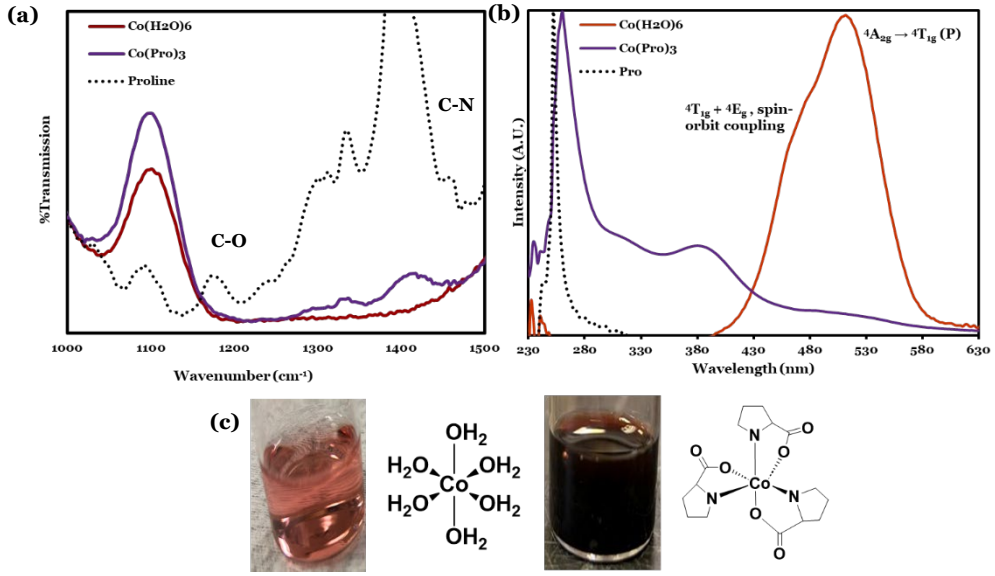

Figure 62. (a) FTIR, (b) UV-VIS, and (c) solution colors of $Co(H_2O)_6$ and $Co(Pro)_3$.

Figure 62(a) FTIR shows C-O and C-N bonds for L-Proline at 1202 cm^{-1} and 1465 cm^{-1} with mixed vibrations in between [49]. A prominent peak for $Co(H_2O)_6$ and $Co(Pro)_3$ are shown around 1100 cm^{-1} and 1098 cm^{-1}, respectively. When coordinated with Co^{2+}, the C-O and C-N vibrations modes vanish. Figure 62(b) shows UV-VIS of solutions, where a prominent peak with a doublet between 430 and 580 nm is seen, attributed to the $^4A_{1g} \rightarrow {}^4T_{1g}$ electron transition and spin-orbit couple splitting [51]. When coordinated with L-Proline, a new peak appears at 380 nm, amidst a broad absorption continuum between 580 nm and 280 nm. L-Proline alone shows a strong peak at 260 nm, likely from the same absorption band shifted to 270 nm when coordinated with Co^{2+}. Figure 62(c) shows optical images of the solutions, with $Co(H_2O)_6$ appearing light red and $Co(Pro)_3$ appearing dark red.

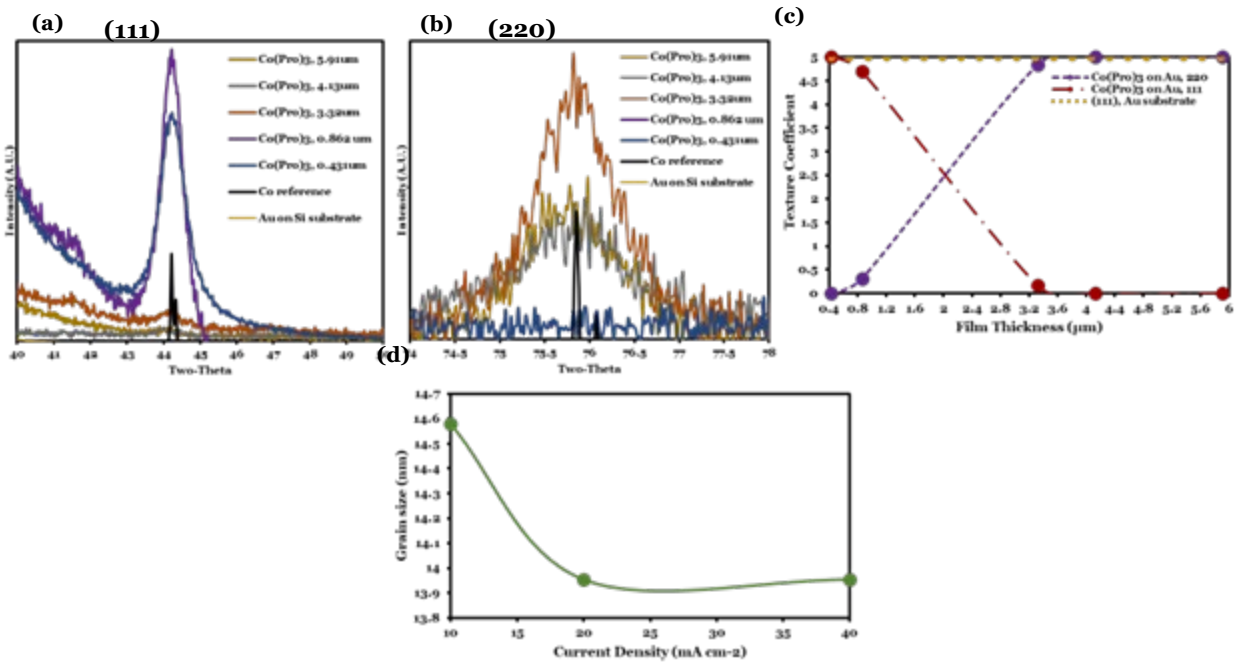

Figure 63. (a) (111) XRD peak of deposited Co as a function of thickness, (b) (220) XRD peak as a function of thickness, (c) texture coefficients as a function of thickness, (d) grain size as a function of applied current density.

Figure 63(a,b) shows XRD peaks for the (111) and (220) plane, respectively. These peaks were the only ones seen that could be identified for cobalt. Figure 63(c) shows the calculated texture coefficient as a function of thickness. It was found that as the thickness of the film increased, the texture evolved from being exclusively oriented as (111) at 431nm, the texture of the substrate, to (220) at 5.91 um. Figure 63(d) shows the calculated grain size as a function of applied current, where it was found that a smaller grain size was attained at higher current, from 14.6 nm at 10 mA cm^{-2} to 13.9 nm at 20 and 40 mA cm^{-2}.

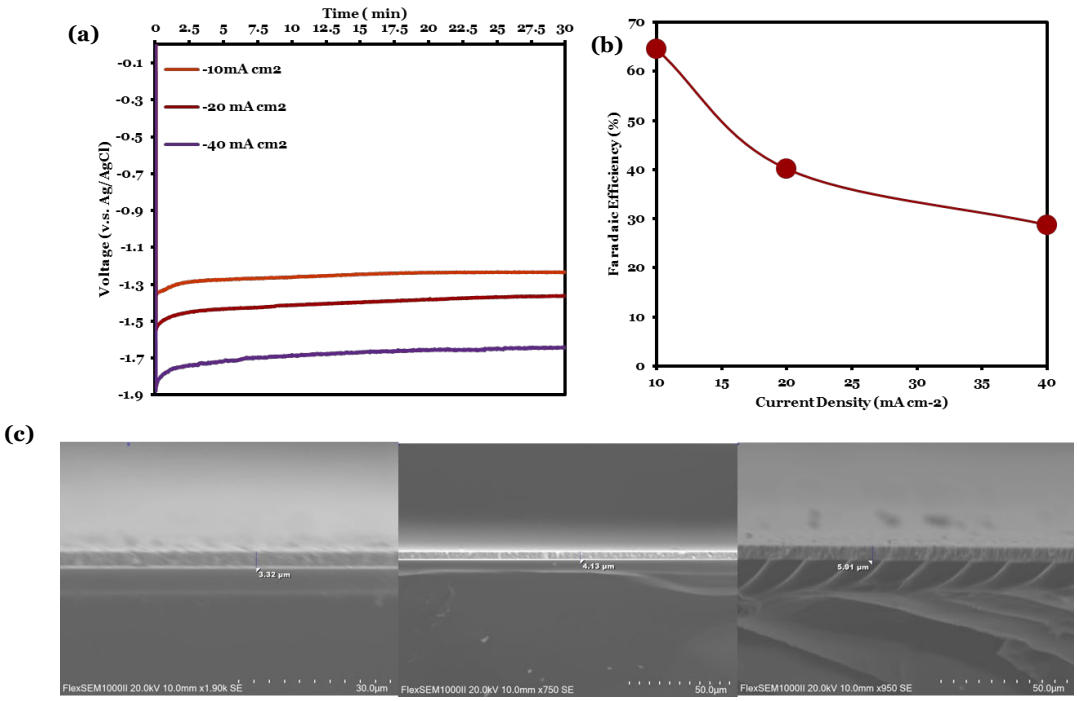

Figure 64. (a) Chronopotentiometry measurements as a function of current density, (b) Faradaic Efficiency as a function of current density, (c) SEM cross-sections as a function of current density (10, 20, and 40 mA cm^{-2}) going left to right.

Figure 64(a) shows chronopotentiometry measurements as a function of current density, where a linear scaling of potential is seen. Figure 64(b) shows the Faradaic efficiency as a function of applied current, where efficiencies of 64.5, 40.1, and 28.7% are seen for 10, 20, and 40 mA cm^{-2}, respectively. Figure 64(c) shows SEM cross sections of each film as a function of current density. EDS found the films had a purity of 84.8 atomic % cobalt, or 95.4 weight %, with the balance being oxygen. Optical profilometry found root mean square (RMS) roughness of the 10, 20, and 40 mA cm^{-2} samples to be 614, 519, and 413nm, respectively.

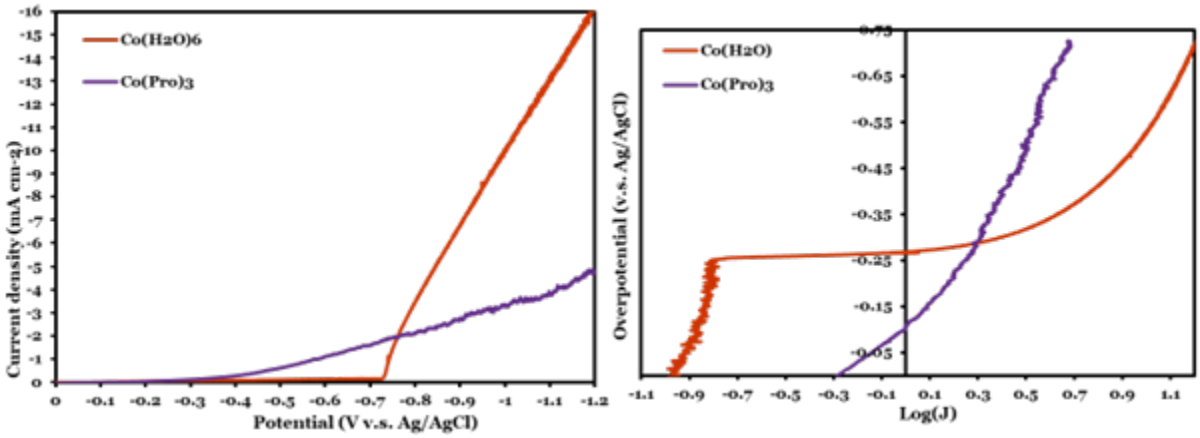

Figure 65. Linear sweep voltammetry (left) and Tafel plot (right) for $Co(Pro)_3$ and $Co(H_2O)_6$ complexes

Figure 65 shows a cathodic linear sweep and Tafel plot for $Co(H_2O)_6$ and $Co(Pro)_3$ complexes. It is seen that $Co(Pro)_3$ shows a reduction peak around -0.95 V (v.s. Ag/AgCl) while $Co(H_2O)_6$ shows only

a large increase in slope around -0.72 V. Tafel analysis was performed, where an exchange current of 0.109 and 0.501 mA cm^{-2} were found for $Co(H_2O)_6$ and $Co(Pro)_3$, respectively. In literature, a value of 0.0072 mA cm^{-2} was found for Co^{2+} for a $CoCl_2/NiCl_2$ chemistry containing 0.05 M Co^{2+}, 0.5M Ni^{2+}, and 0.5 M boric acid at a pH of 3.0 [52]. The reason for a larger exchange current (15x for $Co(H_2O)_6$ and 70x for $Co(Pro)_3$) could be due to several factors, such as the presence of Ni^{2+} and boric acid in the literature chemistry, and the large degree of dilution (Co^{2+} concentration in the current work is 6X that of the paper). As for the influence of L-Proline, a previous report used L-Proline in a Watt's nickel chemistry, where it was found that L-Proline increased the exchange current of Ni^{2+} from 0.00028 mA cm^{-2} to 0.0049 mA cm^{-2} at a concentration of 0.02M L-Proline and a pH of 3.4 [53].

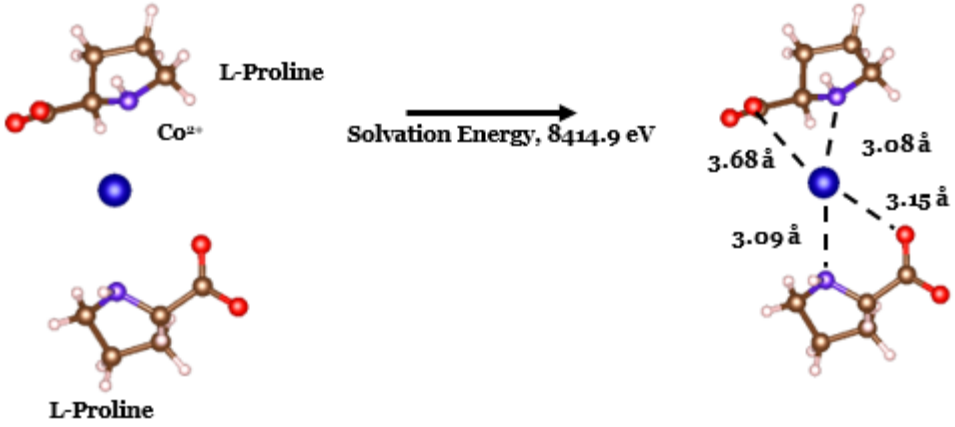

Figure 66. Calculated DFT energetics for the $Co(Pro)_2$ complex.

Figure 66 shows DFT calculations for the $Co(Pro)_2$ complex. It was found that the desolvation energy was low, indicative of hydrogen bonding to the metal center. This is favorable for the electrodeposition process as ligands should be shed at the double layer (desolvated) before Co^{2+} is reduced and deposited to metal [54].

4.6.3. Discussion

The work described electrodeposition from the $Co(Pro)_3$ complex chemistry, where promising results are found.

REFERENCES

[1] Kalidindi, S. R., Buzzy, M., Boyce, B. L., & Dingreville, R. (2022). Digital twins for materials. *Frontiers in Materials*, *9*, 818535.

[2] White, B. C., Garland, A., & Boyce, B. L. (2022). Topological homogenization of metamaterial variability. *Materials Today*, *53*, 16-26.

[3] Hu, C., Martin, S., & Dingreville, R. (2022). Accelerating phase-field predictions via recurrent neural networks learning the microstructure evolution in latent space. *Computer Methods in Applied Mechanics and Engineering*, *397*, 115128.

[4 Desai, S., & Dingreville, R. (2022). Learning time-dependent deposition protocols to design thin films via genetic algorithms. *Materials & Design*, *219*, 110815.

[5] Boyce, B. L. (2022, July). Microstructural black swans. In *IOP conference series: materials science and engineering* (Vol. 1249, No. 1, p. 012004). IOP Publishing.

[6 Oommen, V., Shukla, K., Goswami, S., Dingreville, R., & Karniadakis, G. E. (2022). Learning two-phase microstructure evolution using neural operators and autoencoder architectures. *npj Computational Materials*, *8*(1), 190.

[7] Abram, M., Burghardt, K., Ver Steeg, G., Galstyan, A., & Dingreville, R. (2022). Inferring topological transitions in pattern-forming processes with self-supervised learning. *npj Computational Materials*, *8*(1), 205.

[8] Jensen, S. C., Koepke, J. R., Saiz, D. J., Heiden, M. J., Carroll, J. D., Boyce, B. L., & Jared, B. H. (2022). Optimization of stochastic feature properties in laser powder bed fusion. *Additive Manufacturing*, *56*, 102943.

[9] Johnson, K. L., Moser, D., Rodgers, T. M., & Stender, M. E. (2023). Part-Scale Process Modeling for Metal Additive Manufacturing. In *Additive Manufacturing Design and Applications* (pp. 67-73). ASM International.

[10] Jensen, S. C., Carroll, J. D., Pathare, P. R., Saiz, D. J., Pegues, J. W., Boyce, B. L., ... & Heiden, M. J. (2023). Long-term process stability in additive manufacturing. *Additive Manufacturing*, *61*, 103284.

[11] Monti, J. M., Stewart, J. A., Custer, J. O., Adams, D. P., Depla, D., & Dingreville, R. (2023). Linking simulated polycrystalline thin film microstructures to physical vapor deposition conditions. *Acta Materialia*, *245*, 118581.

[12] Iyer, P. P., Desai, S., Addamane, S., Dingreville, R., & Brener, I. (2023). Learning incoherent light emission steering from metasurfaces using generative models. In *Proceedings of the IEEE/CVF Winter Conference on Applications of Computer Vision* (pp. 3770-3777).

[13] Vizoso, D., Subhash, G., Rajan, K., & Dingreville, R. (2023). Connecting vibrational spectroscopy to atomic structure via supervised manifold learning: Beyond peak analysis. *Chemistry of Materials*, *35*(3), 1186-1200.

[14] Boyce, B., Dingreville, R., Desai, S., Walker, E., Shilt, T., Bassett, K. L., ... & Warren, J. A. (2023). Machine learning for materials science: Barriers to broader adoption. *Matter*, *6*(5), 1320-1323.

[15] Kalaswad, M., Custer, J. O., Addamane, S., Khan, R. M., Jauregui, L., Babuska, T. F., ... & Adams, D. P. (2023). Sputter-deposited Mo Thin films: multimodal characterization of structure, surface morphology, density, residual stress, electrical resistivity, and mechanical response. *Integrating Materials and Manufacturing Innovation*, *12*(2), 118-129.

[16] DelRio, F. W., Mangolini, F., Edwards, C. E., Babuska, T. F., Adams, D. P., Lu, P., & Curry, J. F. (2023). Revealing the structure-property relationships of amorphous carbon tribofilms on platinum-gold surfaces. *Wear*, *522*, 204690.

[17] Barrios, A., Kunka, C., Nogan, J., Hattar, K., & Boyce, B. L. (2023). Automated High-Throughput Fatigue Testing of Freestanding Thin Films. *Small Methods*, *7*(7), 2201591.

[18] Bassett, K. L., Watkins, T., Coleman, J., Bianco, N., Bailey, L. S., Pillars, J., ... & Boyce, B. L. (2023). A Workflow for Accelerating Multimodal Data Collection for Electrodeposited Films. *Integrating Materials and Manufacturing Innovation*, *12*(4), 430-440.

[19] Desai, S., Shrivastava, A., D'Elia, M., Najm, H. N., & Dingreville, R. (2024). Trade-offs in the latent representation of microstructure evolution. *Acta Materialia*, *263*, 119514.

[20] Fowler, J. E., Kottwitz, M. A., Trask, N., & Dingreville, R. (2024). Beyond Combinatorial Materials Science: The 100 Prisoners Problem. *Integrating Materials and Manufacturing Innovation*, *13*(1), 83-91.

[21] Natinsky, E., Khan, R. M., Cullinan, M., & Dingreville, R. (2024). Reconstruction of high-resolution atomic force microscopy measurements from fast-scan data using a Noise2Noise algorithm. *Measurement*, *227*, 114263.

[22] Tsao, J. Y., Abbott, R. G., Crowder, D. C., Desai, S., Dingreville, R. P. M., Fowler, J. E., ... & Stracuzzi, D. J. (2024). AI for Technoscientific Discovery: A Human-Inspired Architecture. *Journal of Creativity*, *34*(2), 100077.

[23] Shrivastava, A., Kalaswad, M., Custer, J. O., Adams, D. P., & Najm, H. N. (2024). Bayesian optimization for stable properties amid processing fluctuations in sputter deposition. *Journal of Vacuum Science & Technology A*, *42*(3).

[24] Walker, E., Trask, N., Martinez, C., Lee, K., Actor, J. A., Saha, S., ... & Boyce, B. L. (2024). Unsupervised physics-informed disentanglement of multimodal data. *Foundations of Data Science*, 0-0.

[25] Oommen, V., Shukla, K., Desai, S., Dingreville, R., & Karniadakis, G. E. (2024). Rethinking materials simulations: Blending direct numerical simulations with neural operators. *npj Computational Materials*, *10*(1), 145.

[26] Dingreville, R., Trask, N.A., Boyce, B.L. Karniadakis, G.E. (2024). "Unlocking alternative solutions to critical materials via materials informatics." *The Bridge*. Issue on Critical Materials, 54(2).

[27] Startt, J., McCarthy, M. J., Wood, M. A., Donegan, S., & Dingreville, R. (2024). Bayesian blacksmithing: discovering thermomechanical properties and deformation mechanisms in high-entropy refractory alloys. *npj Computational Materials*, *10*(1), 164.

[28] Edwards, C. E., Babuska, T. F., Curry, J. F., DelRio, F. W., Killgore, J. P., Boyce, B. L., ... & Mangolini, F. (2024). Tunable amorphous carbon films formed on ultralow wear, Pt–Au alloys. *Carbon*, *226*, 119220.

[29] Fowler, J. E., Ruggles, T. J., Cillessen, D. E., Johnson, K. L., Jauregui, L. J., Craig, R. L., ... & Boyce, B. L. (2024). High-Throughput Microstructural Characterization and Process Correlation Using Automated Electron Backscatter Diffraction. *Integrating Materials and Manufacturing Innovation*, 1-15.

[30] Vizoso, D., & Dingreville, R. (2024). Dataset of simulated vibrational density of states and X-ray diffraction profiles of mechanically deformed and disordered atomic structures in Gold, Iron, Magnesium, and Silicon. *Data in Brief*, *55*, 110689.

[31] Dingreville, R., Roberston, A. E., Attari, V., Greenwood, M., Ofori-Opoku, N., Ramesh, M., ... & Zhang, Q. (2024). Benchmarking machine learning strategies for phase-field problems. *Modelling and Simulation in Materials Science and Engineering*, *32*(6), 065019.

[32] Adams, D.P., Kothari, R., Addamane, S., Jain, M., Dorman, K., Desai, S., Sobczak, C., Kalaswad, M., Bianco, N., DelRio, F.W., Custer, J.O., Rodriguez, M.A., Boro, J., Dingreville,

R., Boyce, B.L. (2024). Guided combinatorial synthesis and automated characterization expedites the discovery of hard, electrically conductive PtxAu1-x films, *J. Vac. Sci. Techn. A*. Accepted for publication.

[33] Bianco, N., Fitzgerald, K., Cillessen, D., Brown, N., Carroll, J., Garland, A., Bassett, K.L., Schroder, J.B., Boyce, B.L. (2024). Toughness from Imagery: extracting more from failure analysis using deep convolutional neural networks, submitted to *Journal of Failure Analysis and Prevention*, Accepted for publication.

[34] Custer, J.O., Kalaswad, K., Kothari, R.S., Kotula, P.G., Ruggles, T., Dingreville, R., Henriksen, A., Adams, D.P. (2024). Sputter-deposited Mo thin films: characterization of grain structure and Monte Carlo simulations of sputtered atom energies and incidence angles. To be submitted to *Integrating Materials and Manufacturing Innovations*..

[35] Dorman, K. R., Bianco, N., Kothari, R., Kalaswad, M., Sobczak, C., Desai, S., Custer, J., Addamane, S., Jain, M., Hinojos, A., Rodriguez, M., DelRio, F., Boyce, B. L., Dingreville, R., & Adams, D. P. (2024). "Cu-Ag Nanocrystalline Thin Films: Materials Library Development for the Study of Process-Property-Microstructure Relationships". To be submitted to *Thin Solid Films*.

[36] M. McKinney, A. Garland, D. Cillessen, J. Adamczyk, D. Bolintineanu, M. Heiden, E. Fowler, B.L. Boyce, (2024) "Unsupervised multimodal fusion of in-process sensor data for advanced manufacturing process monitoring", to be submitted to *Journal of Manufacturing Systems*.

[37] Shilt, T., Adams, D. P., Martinez, C., Dingreville, R. (2024). "Understanding Pt_xAu_{1-x} films through unsupervised disentanglement of multimodal data". To be submitted to *npj Computational Materials*.

[38] Deshwal, A. and Doppa, J. (2021). Combining latent space and structured kernels for Bayesian optimization over combinatorial spaces. *Advances in Neural Information Processing Systems*, 34:8185–8200.

[39] Eismann, S., Levy, D., Shu, R., Bartzsch, S., and Ermon, S. (2018). Bayesian optimization and attribute adjustment. In *Proc. 34th Conference on Uncertainty in Artificial Intelligence*.

[40] Grosnit, A., Tutunov, R., Maraval, A. M., Griffiths, R.-R., Cowen-Rivers, A. I., Yang, L., Zhu, L., Lyu, W., Chen, Z., and Wang, J. (2021). High-dimensional Bayesian optimization with variational autoencoders and deep metric learning. *arXiv preprint* arXiv:2106.03609.

[41] Tripp, A., Daxberger, E., and Hernandez-Lobato, J. M. (2020). Sample-efficient optimization in the latent space of deep generative models via weighted retraining. *Advances in Neural Information Processing Systems*, 33:11259–11272.

[42] Kato, M.; Hayashi, M.; Fujihara, T.; Nagasawa, A. (2008). (-)545-fac-[Delta]-Tris(l-prolinato)cobalt(III) trihydrate. *Acta Crystallographica Section E*, 64 (5), m684.

[43] Nugrahani, I.; Utami, D.; Permana, B.; Ibrahim, S. (2018) Development of the NSAID-L-proline amino acid zwitterionic cocrystals. *Journal of Applied Pharmaceutical Science*, 8 (4), 057-063.

[44] Giannozzi, P.; Baroni, S.; Bonini, N.; Calandra, M.; Car, R.; Cavazzoni, C.; Ceresoli, D.; Chiarotti, G. L.; Cococcioni, M.; Dabo, I. (2009) QUANTUM ESPRESSO: a modular and open-source software project for quantum simulations of materials. *Journal of physics: Condensed Matter*, 21 (39), 395502.

[45] van Setten, M. J.; Giantomassi, M.; Bousquet, E.; Verstraete, M. J.; Hamann, D. R.; Gonze, X.; Rignanese, G.-M. (2018) The PseudoDojo: Training and grading a 85 element optimized norm-conserving pseudopotential table. *Computer Physics Communications*, 226, 39-54.

[46] Perdew, J. P.; Burke, K.; Ernzerhof, M. (1996) Generalized gradient approximation made simple. *Physical Review Letters*, 77 (18), 3865.

[47] Monkhorst, H. J.; Pack, J. D. (1976) Special points for Brillouin-zone integrations. *Physical Review B*, 13 (12), 5188.
[48] Andreussi, O.; Dabo, I.; Marzari, N. (2012). Revised self-consistent continuum solvation in electronic-structure calculations. *The Journal of Chemical Physics*, 136 (6), 064102.
[49] Martyna, G. J.; Tuckerman, M. E. (1999). A reciprocal space based method for treating long range interactions in ab initio and force-field-based calculations in clusters. *The Journal of Chemical Physics*, 110 (6), 2810-2821.
[50] Cahyana, A.H., Liandi, A.R. and Anwar, N., (2022). An ionic liquids catalyst approach for synthesis of pyrimidine derivatives using l-proline nitrate. *Journal of Applied Pharmaceutical Science*, *12*(5), 240-245.
[51] Liu, W.; Migdisov, A.; Williams-Jones, A. (2012) The stability of aqueous nickel(II) chloride complexes in hydrothermal solutions: Results of UV–Visible spectroscopic experiments. *Geochimica et Cosmochimica Acta*, 94, 276-290.
[52] Iuchi, S.; Sakaki, S. (2010) Spin–orbit coupling in a model Hamiltonian for d–d excited states of Ni2+ ion aqueous solution. *Chemical Physics Letters*, 485 (1), 114-118.
[53] Hu, Q.; Yang, G.; Zhao, Y.; Yin, J. (2003) Determination of copper, nickel, cobalt, silver, lead, cadmium, and mercury ions in water by solid-phase extraction and the RP-HPLC with UV-Vis detection. *Analytical and Bioanalytical Chemistry*, 375, 831-835.
[54] Fan, C.; Piron, D. L. (1996) Study of anomalous nickel-cobalt electrodeposition with different electrolytes and current densities. *Electrochimica Acta*, 41 (10), 1713-1719.

DISTRIBUTION

Email—Internal

Name	Org.	Sandia Email Address
Dawn Flicker	1000	dgflick@sandia.gov
Basil Hassan	1500	bhassan@sandia.gov
Joel S. Lash	1800	jslash@sandia.gov
Ryan R. Wixom	1881	rrwixom@sandia.gov
Dan Sinars	1900	dbsinar@sandia.gov
Marie D. Arrowsmith	1910	mdarrow@sandia.gov
Wahid L. Hermina	1910	wlhermi@sandia.gov
Kevin R. Dixon	5500	krdixon@sandia.gov
Technical Library	1911	sanddocs@sandia.gov

This page left blank

Sandia National Laboratories

Sandia National Laboratories is a multimission laboratory managed and operated by National Technology & Engineering Solutions of Sandia LLC, a wholly owned subsidiary of Honeywell International Inc. for the U.S. Department of Energy's National Nuclear Security Administration under contract DE-NA0003525.